THESIS

DIRECT DIGITAL MANUFACTURE OF CONTINUOUS FIBER REINFORCED THERMOPLASTIC HIGH ASPECT RATIO COMPOSITE GRID STIFFENERS AND GRID STIFFENER INTERSECTIONS WITH RADICALLY REDUCED TOOLING

Submitted by

Steven J. Hogan

Department of Mechanical Engineering

In partial fulfillment of the requirements

For the Degree of Master of Science

Colorado State University

Fort Collins, Colorado

Spring 2024

Master's Committee:

Advisor: Donald W. Radford

Paul Heyliger
Mostafa Yourdkhani

ABSTRACT

DIRECT DIGITAL MANUFACTURE OF CONTINUOUS FIBER REINFORCED THERMOPLASTIC HIGH ASPECT RATIO COMPOSITE GRID STIFFENERS AND GRID STIFFENER INTERSECTIONS WITH RADICALLY REDUCED TOOLING

Grid stiffened structures are widely used in the aerospace industry due to their high strength and stiffness to weight ratio and impact damage tolerance. These structures consist of a lattice pattern of stiffening ribs bonded to a thin shell structure, where the stiffening ribs commonly act as the main load bearing members, and the shell acts to cover the ribs and transfer loads through membrane action. These structures offer a variety of beneficial structural properties including high specific strength and stiffness, high impact resistance, high compressive resistance, and high energy absorption. However, the complexity of a grid pattern can lead to excessive manufacturing times, especially for simple constructions such as flat plates. A more promising alternative for manufacturing grid stiffened structures is the use of automated manufacturing methods including ATL, AFP, and filament winding. Because composite grid stiffened structures can be composed entirely of the same composite material, the manufacturing process with these methods can be almost entirely automated, saving time and money. However, the traditional and automated methods of producing composite grid stiffened structures require the fabrication of complex tooling to develop the geometry of stiffening ribs. In addition, all composite grid stiffened structures suffer from the same manufacturing difficulty: for all of the fibers to be continuous through an intersection node, there must be twice as much material at

each intersection than in each rib, making intersection compaction extremely difficult. A more recently developed composite manufacturing method is additive manufacturing (AM) in the form of composite 3D printing, which offers a much higher degree of geometric freedom than other autonomous manufacturing methods and does not require tooling. However, composite 3D printing is generally limited to low fiber volume fractions. A manufacturing method with the ability to make high quality, high fiber volume fraction continuous fiber grid stiffened structures without the need for tooling could significantly increase the efficiency and decrease the cost to produce these structures.

The current study proposes the use of a novel additive manufacturing method which uses a commingled feedstock and features in situ consolidation to produce grid stiffened structures without the need for tooling. Several stiffener ribs and stiffener rib intersections were produced and tested for composite quality. The fiber volume fraction and void volume fraction through the height and length of printed stiffener ribs and intersections was analyzed to determine if the quality was consistent. A micrograph evaluation was performed on the high aspect ratio stiffener rib and intersection composites to qualitatively evaluate the reinforcement distribution, determine the void locations, and to support the constituent material concentration measurements. The consolidation force was measured during the manufacturing of the samples to better understand the forces experienced during printing and to form a relationship between the consolidation force experienced and the constituent volume fraction of the samples. The results of this study suggest that the application of direct digital manufacture to the placement and consolidation of commingled tow for the fabrication of high aspect ratio grid stiffeners and intersections, without the need for tooling, can readily achieve fiber volume fractions greater than 50% and void fractions as low as 5%. Volume fraction analysis results show that

manufactured stiffener ribs and stiffener grid intersections exhibit high fiber volume fractions and low void volume fractions which remain consistent through the height of the samples. Consolidation force measurement results show that a significant decrease in force is experienced between print layers. Microscopic analysis results show that the majority of voids collect at the edges of print layers leading to an increase in void content at the intersection node and potentially masking any quality gradient through the height of samples that may exist. The results of this study show the high potential for the manufacturing of high quality high aspect ratio continuous fiber composite grid stiffener structures through direct digital manufacturing technologies without the need for tooling.

ACKNOWLEDGEMENTS

Firstly, I must extend my gratitude to my advisor, Dr. Donald W. Radford, for his continuous support and guidance throughout my research. Without his direction and guidance, I would not have been able to achieve all that I have at CSU. Secondly, I would like to thank my committee members, Dr. Mostafa Yourdkhani and Dr. Paul Heyliger, for challenging me in the classroom and bolstering my confidence as a graduate student. Finally, I would like to thank my family and friends for their unwavering support through my advanced degree. I love you all so very much. I would especially like to thank my father, Dr. Timothy Hogan, for his unparalleled patience and insight which have helped shape me into the engineer that I am today.

TABLE OF CONTENTS

LIST OF TABLES

LIST OF FIGURES

1 Introduction

Continuous fiber reinforced polymer matrix composites are valuable structural materials due to their high strength and stiffness to weight ratios. Historically manufacturing of these structures was limited to flat or gradually curved sheets, however more recent advances in fiber reinforced polymer composite manufacturing technologies have allowed for complex structures to be manufactured. One such structure is the grid stiffened panel, which consists of a grid of stiffeners supporting a face sheet panel. The marriage of continuous fiber composites and grid stiffened panel structures results in one of the lightest and strongest structural materials available.

1.1 Grid Stiffened Structures

Grid stiffened structures are widely used in the aerospace industry due to their high strength and stiffness to weight ratio and impact damage tolerance. One of the most prominent uses of grid stiffened structures in the aerospace industry is the construction of airplane fuselages. Modern aircraft fuselage structures have been made from grid stiffened cylindrical structures [1]. Another prominent application of grid stiffened structures in aerospace is in spaceship shrouds and boosters, which must support the full weight of the upper stages of the rockets while under high G forces [2]. A recent example of the application of a grid stiffened structure is the development of an extended launch vehicle fairing for the Air Force Research Laboratory's Minotaur launch vehicle [3]. An example of a grid stiffened structure is shown in Figure 1.

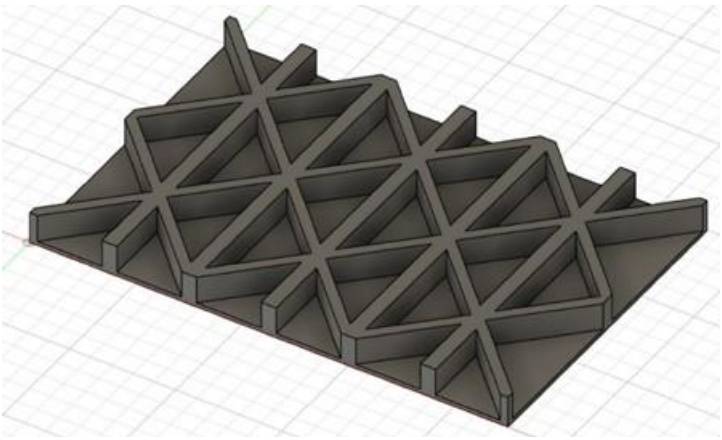

Figure 1: 3D modeled example of a grid stiffened panel structure.

Grid stiffened structures consist of a lattice pattern of stiffening ribs bonded to a thin shell structure. The shell can be in many shapes, with the most common forms being a cylinder and a flat or curved panel. Typically, the stiffening ribs run in 2-4 directions along the shell forming a repeating pattern. Stiffening ribs can be bound to one or both sides of the skin structure. In these structures the stiffening ribs commonly act as the main load bearing members, and the skin acts to cover the ribs and transfer loads through membrane action [4]. Adding stiffeners significantly increases the load resistance of a skin structure without much increase in weight. Further weight reduction is achieved by making both the shell structure and the stiffening grid out of fiber reinforced polymer composite materials. The marriage of continuous fiber composites and grid stiffened panel structures results in one of the lightest and strongest structural materials available.

Grid stiffened structures offer a variety of beneficial structural properties. Grid stiffened structures have high specific strength and stiffness, high impact resistance, high compressive resistance, and high energy absorption [5]. Due to their high flexural stiffness grid stiffened

panels can, in many design scenarios, compete with sandwich panel construction. Unlike sandwich panels, which have a foam or honeycomb core that needs to be completely sealed off from the outside environment, grid stiffened panels are constructed completely out of composite material. Grid stiffened panels are comparatively much more resistant to moisture, as water inside the core of a sandwich panel can degrade the core and cause catastrophic damage to the structure [6]. Additionally, it has been found that delaminations caused by impact damage to a grid stiffened structure tend to be contained to a single cell, limiting the potential to spread and eventually cause complete failure of the structure [6].

There are still some drawbacks associated with the production of grid stiffened structures. Grid stiffened structures exhibit a high level of geometric complexity. The complexity of a grid pattern can lead to excessive manufacturing times, especially for simple constructions such as flat plates. Intricate grid stiffener designs can increase the time to produce the structure depending on the manufacturing method being used. Traditional manufacturing of composite grid stiffened structures requires complex tooling to be made [2]. This tooling is required to guide the placement of fibers in the stiffening grid. During a composite cure cycle, stiffener grid tooling usually expands which helps to compact and shape the stiffener grid trusses. The cost of tooling can be significant especially for custom parts, which require an entire tool to be machined just to manufacture that part.

1.2 Grid Stiffened Structure Manufacturing

Originally, grid stiffened structures were not produced out of composite material but rather were machined out of stock metal. They were manufactured either by milling out each individual cell of the grid or by assembling individually manufactured stiffener ribs to form the grid. The McDonnell-Douglas Corporation holds the patent rights for the development of the

first aluminum isogrid, which is considered the earliest precursor of modern grid stiffened structures [6]. This structure was manufactured by machining it out of a single piece of aluminum stock. This method was costly and time consuming, requiring large sheets of stock material and precise machining of each individual stiffening grid cell. More recent development of grid stiffened structures utilized fiber reinforced composite materials to maximize the strength and stiffness to weight ratios of the structures [7]. Grid stiffened structures manufactured out of fiber reinforced composite materials are commonly referred to as Advanced Grid Stiffened (AGS) structures [8]. AGS structures were manufactured by placing composite material into channels cut into a mold which was used to define the geometry of the stiffener grid ribs. The composite material used for grid stiffened structure manufacturing can take many forms, however it usually has some form of matrix pre-impregnation prior to placement. A thin face sheet skin could then be added to the structure. The skin could either be hand laid on top of the grid pattern and the entire part cured together, or the skin could be premanufactured and bonded to the stiffener grid with adhesive. Composite isogrid panels were manufactured by combining filament winding and hand lay-up methods [9]. This method used dry reinforcement fibers which were impregnated with an uncured epoxy resin and placed in a silicone mold to define the geometry of the stiffening grid. Another study manufactured isogrid stiffened panels using a high temperature rubber mold and pre-impregnated tows of reinforcement [10]. Axial compression tests demonstrated that this manufacturing method could produce grid stiffened structures with excellent stiffener consolidation and skin finish.

A more promising alternative for manufacturing grid stiffened structures is the use of automated manufacturing methods including ATL, AFP, and filament winding. These systems are able to precisely place composite material along desired paths without the need for manual

positioning, which eliminates the presence of imperfections caused by human error. Because AGS structures can be composed entirely of the same composite material, the manufacturing process with these methods can be almost entirely automated, saving time and money.

1.2.1 Automated Tape Laying and Automated Fiber Placement

Automated Tape Laying (ATL) and Automated Fiber Placement (AFP) are similar manufacturing process that both involve an automated process of applying fiber reinforced tapes or tows using a spring-loaded consolidation roller system and a localized heat source [11]. These processes have been used to manufacture large scale composite parts and are generally limited to manufacturing flat or low curvature laminates where the curvature radii are superior to 10 m in the directions normal to the laying direction [12]. ATL uses a single wide tape while AFP uses multiple narrow tapes. The tapes used by ATL and AFP systems are typically composed of several reinforcement fiber tows which are pre-impregnated with thermoplastic or thermoset resin. In the composites industry a fiber tow refers to a bundle of continuous fibers which can be different in size depending on the number of fibers in the bundle. Common tow sizes include 1k, 3k, 6k, 12k, and 50k fiber bundles. For thermoplastic resin, the localized heat source, which is usually in the form of a laser or a heated air blower, is used to reduce the viscosity of the tape which helps it bond to the tool or the previously laid tape layers. For thermoset resin, the heat source is used to advance the curing of the resin to cause it to bond to the tool or previous layers. A consolidation roller is used to precisely place the tapes, to assist in bonding the tape to the tool or previous layer, and to compact the layers together [13]. These systems often include a cut-and-place mechanism which allows for in situ cutting, repositioning, and restarting of the tape. A diagram of an ATL/AFP system is shown in Figure 3.

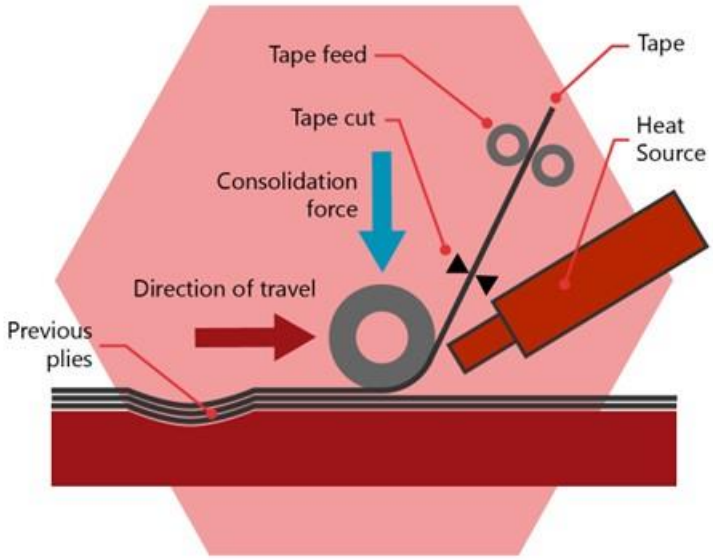

Figure 2: Diagram of ATL/AFP machine [11].

ATL and AFP manufacturing methods have been used to produce grid stiffened structures from fiber reinforced composite materials. The feasibility of grid stiffener intersections manufactured by AFP has been validated by the National Aerospace Laboratory [14]. The results show that grid stiffeners manufactured by AFP can exhibit better dimensional accuracy and have better interface strength between the stiffeners and skin than other conventional manufacturing processes. However, the manufacturing process required several metal support blocks to be used as tooling to define the geometry of the stiffening ribs during manufacturing. Another study leveraged off the findings of the first and manufactured full grid stiffened panel structures using a similar AFP process [15]. This study also required the use of a metal mold to define the stiffening grid geometry during fabrication.

1.2.2 Filament Winding

Filament winding is a composite manufacturing process where continuous fiber reinforcement is wound to a rotating mandrel [16]. A stationary rotating mandrel acts as the deposition surface while a carriage arm moves horizontally with the mandrel. The arm contains a winding pay-out eye, which groups and dispenses pre-impregnated fibers onto the mandrel. As the mandrel turns, the fibers wrap around it to form a composite winding over the mandrel's surface. A diagram of the filament winding method is shown in figure 3.

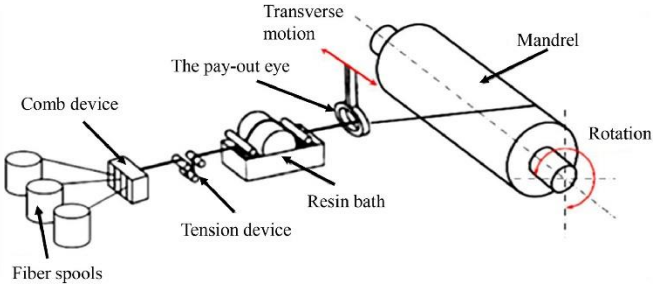

Figure 3: Schematic of filament winding process [16].

Filament winding has emerged as the primary process for composite cylindrical structure fabrication [17]. This process is commonly used for making tube and pipe-shaped objects such as rocket motor cases, launch tubes, golf club shafts, fishing rods, and high-pressure storage tanks [18]. In the composites industry, the process of filament winding has evolved to be the preferred, and most cost effective method, for producing pressure retaining structures from fiber reinforced polymer composites [19].

While flat grid stiffened panel structures could not be manufactured through a filament winding process, cylindrical grid stiffened structures can and have been manufactured using this process. One study produced stiffening lattice grid cylinders using a filament winding process to

investigate and compare their compressive strengths to that of solid composite cylinders produced using the same manufacturing process [20]. The study found that the structural efficiency of the lattice grid cylinders was higher than the solid composite cylinders. A high density polyurethane foam tool with CNC machined grooves was used to position and shape the stiffening ribs of the grid structures. Another study produced a grid stiffened cylinder using a robotic filament winding system which exhibited excellent constituent volume fraction values in both the ribs and the skin [21]. This method was highly autonomous and was similar to an ATL process but onto a rotating mandrel instead of a flat build platform. However, this method still required a machined tool made out of epoxy resin to guide fiber placement.

1.2.3 Manufacturing Limitations

While promising, the traditional and automated methods of producing AGS structures require the fabrication of complex tooling to develop the geometry of stiffening ribs [6]. The flexural stiffness of an AGS structure is largely dictated by the geometry of its stiffening ribs. Taller ribs will increase the bending stiffness, however wider ribs greatly increase the weight of the structure. Thus, grid stiffened panels produced to have high out of plane bending stiffness need to have taller, thinner stiffening ribs. Precise placement of fiber tows requires a mold to guide and shape the material into the desired stiffening rib geometry. These molds are commonly made out of a silicone rubber with a high coefficient of thermal expansion. This material is used so that during the curing process, the rubber mold expands and provides lateral compaction which squeezes excessive resin and results in a better rib/skin consolidation [22].

In addition, all AGS structures suffer from the same manufacturing difficulty: for all of the fibers to be continuous through an intersection node, there must be twice as much material at each intersection than in each rib, making intersection compaction extremely difficult [23]. Most

traditional manufacturing methods still result in grid structures with buildup at the intersection nodes, which can negatively affect the strength and stiffness of the structure. An example of this buildup is shown in Figure 4.

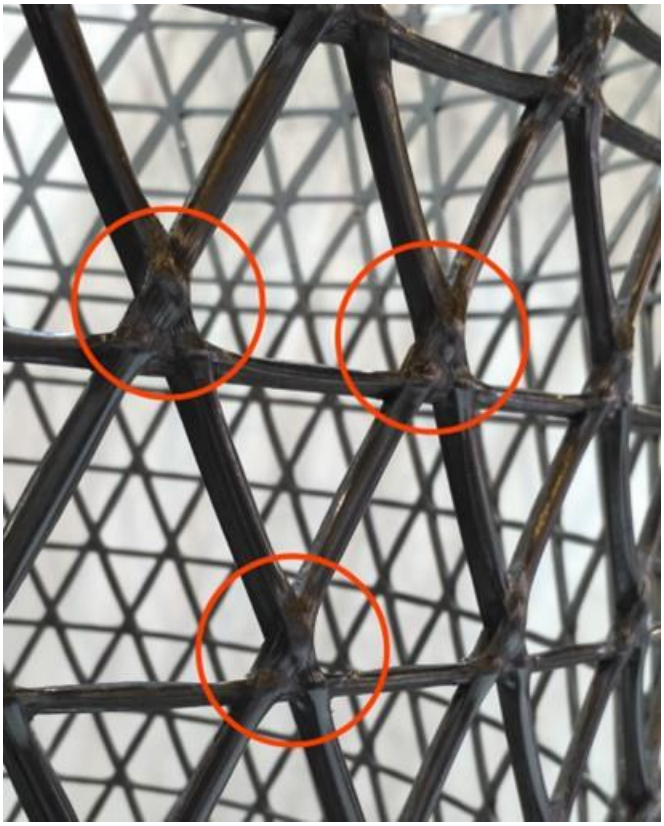

Figure 4: Prepreg based stiffener grid lattice showing buildup at intersections [24].

Three different approaches are generally used to deal with the material build up at stiffener grid intersection nodes [25]. The first approach involves allowing the dimensions of the grid stiffeners to change through the intersection. This can take the form of either an increase in stiffener height through the intersection or an increase in stiffener width. More commonly, the stiffener grid height is allowed to increase at the intersections [26, 27]. However, this increase in height leads to out-of-plane fiber undulation which reduces mechanical performance, particularly

in compression, of stiffening grid structures. Instead, other studies have kept the stiffening rib height the same by locally spreading the fibers to widen the stiffening ribs at the intersection points [14]. A similar method is used to deal with stiffener rib intersections for the research conducted in this report discussed in later chapters. An example of the stiffener grid widening at the intersections is shown in figure 5.

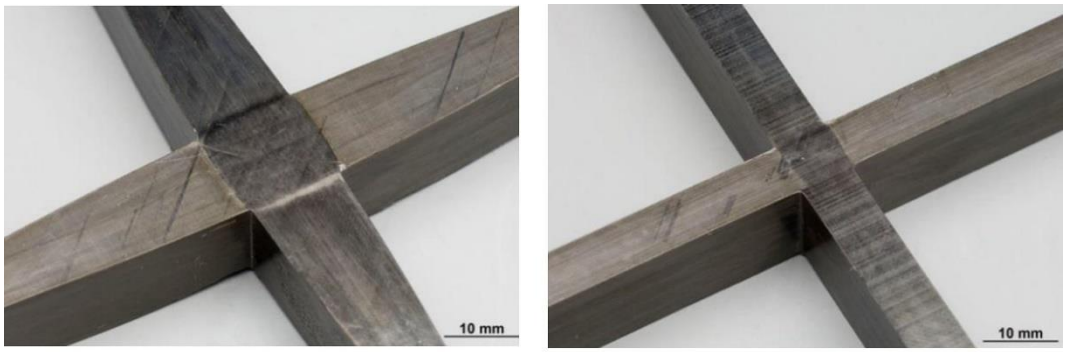

(a) (b)

Figure 5: Methods for reducing intersection buildup. (a) Widening of the stiffeners by spreading the tows. (b) Alternating discontinuous tows [14].

The second approach for dealing with stiffener grid intersection build up is to alter the resin content of the stiffening grid while keeping the geometry of the same [27, 28, 29]. This results in a higher matrix content in the stiffener ribs and a higher reinforcement fiber content at the intersections. The obvious disadvantage is that this approach results in a reduction in mechanical properties of the stiffeners.

The third approach is to reduce the number of layers at the intersection nodes through the use of discontinuous plies [14, 15] . In this approach, alternating layers of the stiffener ribs are cut just before the intersection node and restarted just after the node. This results in a constant geometry and resin content of the stiffening ribs through the intersection nodes as the nodes

contain the same number of layers as the rest of the stiffening grid. The downside of this approach is that the fiber discontinuity results in inefficient load transfer across the intersection nodes.

A final challenge in composite manufacturing more specific to autonomous processes is the manufacturing of curved tow paths. In order to effectively manufacture composite parts using ATL, AFP, or filament winding, the tow or tape must be able to completely conform to the shape of the tool. Curved paths can introduce a potential problem because the length of the inside of the curve is less than the length of the outside of the curve. To apply the material smoothly and evenly along a curved path, the fibers must be able to shear relative to one another [30, 31]. Incorporating this can improve the overall quality of composite structures with complex curved geometries by reducing the number of cuts and resulting gaps within the laminate. An example of traditional non-shearing tow paths versus shearing tow paths is shown in Figure 6.

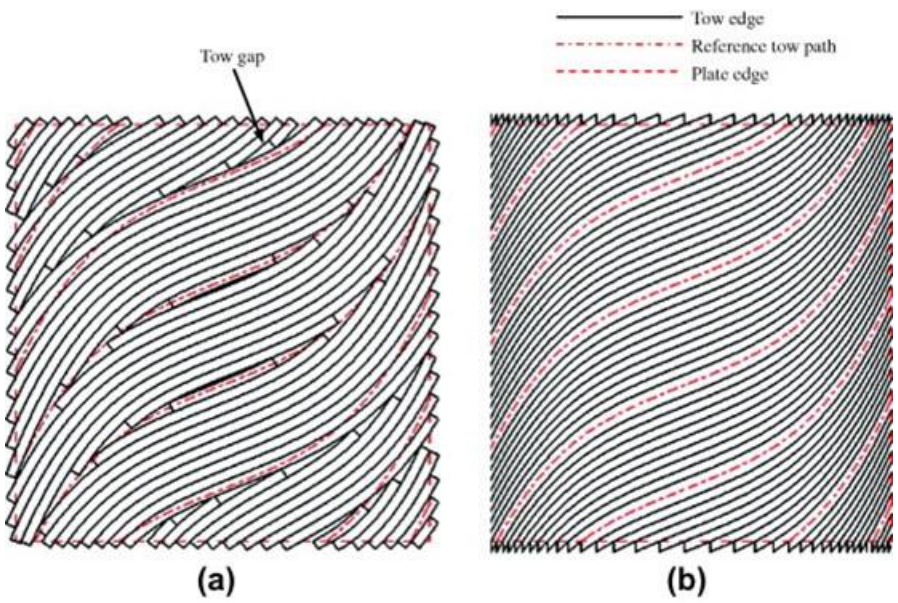

Figure 6: Traditional ATL Tow Paths vs Tow Shearing Paths [30].

Originally curved tow paths were produced by rotating the placement head of the system to follow the curve of the path to keep the axis of the consolidation roller perpendicular to the tangent line of the reference tow path [30]. However, this method causes fiber buckling and straightening on the inside and outside of the curved tow. Instead, a novel fiber placement technique was developed to manufacture curved tow paths which uses in-plane shear deformation of the tow instead of in-plane bending deformation [30]. This technique, called continuous tow shearing (CTS), involves the fibers in the tow slipping past each other as the tow is shifted. Unlike conventional tow bending AFP techniques, the fibers exactly follow the intended tow path, and tow gaps or overlaps are not formed. A further study adopted and modified the CTS technique to be able to produce curved tow paths with wider prepreg tapes [32]. This study was able to achieve steering radii as low as 50 mm with 100 mm wide prepreg tapes. Another study also produced complex reinforcement paths through a tow shearing process [33]. This study utilized a custom designed multi-axis filament winder system which used a commingled tow feedstock.

For the majority of grid stiffened composite structures, the ability to manufacture curved tow paths is not necessary as the stiffening ribs are usually straight and the geometry of these structures is usually limited to flat sheets or cylinders, which do not require curved tow paths to conform to the tooling surface. However, more recent studies have developed and analyzed stiffener grid structures with curved stiffeners [34, 35, 36, 37]. Manufacturing these structures would require the ability to produce curved tow paths that did not exhibit any buckling or wrinkling on the inside of the curves so that multiple layers could be built up to create the stiffening ribs. Although the manufacturing of curved paths is demonstrated and utilized in the research discussed in this report, it was not the focus of the research being presented.

1.2.4 Additive Manufacturing Methods

A more recently developed composite manufacturing method which does not have many of the manufacturing limitations described above is additive manufacturing (AM) in the form of composite 3D printing. 3D printing offers a much higher degree of geometric freedom than other autonomous manufacturing methods. The majority of the composite 3D printers can be used to manufacture short or continuous fiber composite structures and are significantly lower in cost than ATL/AFP systems. 3D printing can come in many different forms, including selective laser sintering (SLS), Fused Filament Fabrication (FFF) which is also known as Fused Deposition Modeling (FDM), and Stereolithography (SLA) [38]. However, the majority of composite 3D printing is FFF. There are several types of composite FFF 3D printers which are differentiated by the feedstock material that they use.

Short fiber composite FFF is the most widely available form of composite 3D printing. In fact, almost all commercially available standard 3D printers are capable of printing short fiber composite parts. 3D printing of short fiber reinforced composite parts is done by using specialized filament which consists of milled fibers mixed into a thermoplastic. Milled fibers are a short form of fiber reinforcement typically around 100 μm in length [39]. Milled fiber filaments are available with many different types of reinforcement fiber materials, however carbon fiber reinforcement is the most prevalent type. An example would be 3DXTECH's CarbonX line of short fiber reinforced 3D printer filaments which are available in a variety of thermoplastics [40]. These filaments are available in the standard 1.75 mm and 2.85 mm filament sizes used by almost all desktop 3D printers. Modifications to 3D printers are rarely required to print with short fiber composite filaments, however replacement parts are commonly recommended to maintain the longevity of the printer. For example, it is usually recommended

for printing with short fiber filaments to replace the stock brass nozzle with a hardened steel one which is more resistant to gradual abrasions caused by the reinforcement fibers.

The obvious downside of using short fiber composite 3D printing for manufacturing is the inherent inferior mechanical properties that short fiber manufactured parts exhibit when compared to the same parts manufactured using a continuous fiber manufacturing process. One study comparing the mechanical properties of short fiber and continuous fiber reinforced 3d printed samples found that the tensile strength and the elastic modulus of the short fiber specimens were only 13% and 20% of the tensile strength and the elastic modulus of the continuous fiber specimens, respectively [41]. This is mainly due to the short length of the reinforcement fibers in most fiber reinforced 3D printing filament, which falls well below the critical fiber length. Upon failure, the short fibers will pull out of the matrix rather than reinforce up to fiber failure. The minimum length to have the fibers rupture rather than pull out is known as the critical fiber length [42]. The critical length of carbon fibers in an ABS matrix has been calculated to be about 640 µm, while the majority of milled fibers used in AM composite materials fall below 150 µm in length [43].

Short fiber composite 3D printing has been used to manufacture stiffening grid structures. One study analyzed the buckling behavior of 3D printed composite isogrid structures [44]. This study used a short carbon fiber filled polyamide filament with 20% by weight of milled fiber reinforcement. This study explored the effects that varying geometric variables, specifically rib thickness and cell height, had on the compressive strength and buckling behavior of grid structures. Another study investigated the compression behavior of 3D printed isogrid cylindrical shell structures [45]. This study compared the compression properties of isogrid cylinders printed with fiber reinforced filament to isogrid cylinders printed with neat thermoplastic filament. This

study also used a short carbon fiber filled polyamide with the same fiber weight content of 20%. This study found that the compressive strength of the fiber reinforced isogrid cylinder was roughly 50% higher than that of the neat thermoplastic isogrid cylinder.

For continuous fiber 3D printing, a more complicated manufacturing process is required. One method is to combine the reinforcement fibers and the matrix material within the print head, as shown in figure 7. This method of in-nozzle impregnation was first successfully reported in a 2016 study [46]. The benefit of using this method is that the fiber volume can be varied while printing. The ability to change the fiber volume fraction while printing allows for localized tailoring of the stiffness and toughness of a part as desired. However, this method of continuous fiber 3D printing is limited to relatively low fiber volume fractions (<35%) [47]. Additionally, studies have shown that the reinforcement fibers do not intersperse evenly through the printed strand [48].

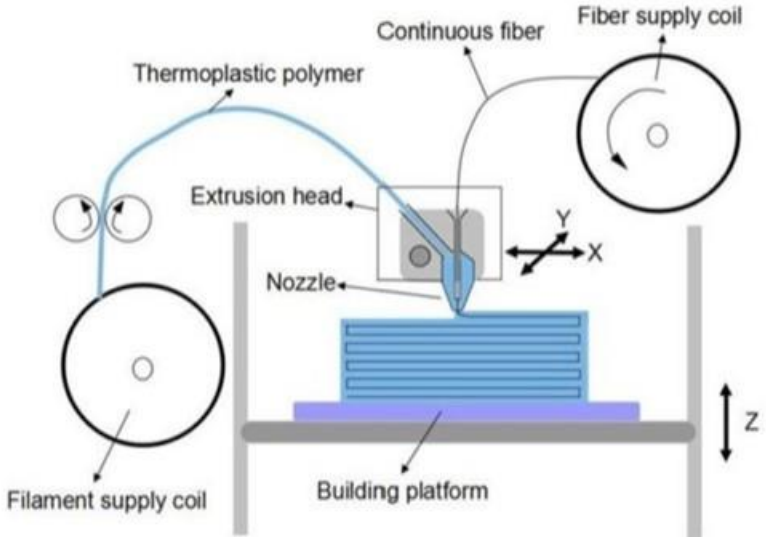

Figure 7: Diagram of continuous fiber 3D printing method where the reinforcement fibers and the thermoplastic matrix material are mixed within the print head [47].

A second manufacturing method is the use of two print heads with one used for placing reinforcement and the other used for printing thermoplastic. Recently, a number of continuous fiber composite 3D printers using this manufacturing method have become commercially available. Two of the most predominant dual-head continuous fiber composite 3D printer manufacturers are Markforged and Desktop Metal [49, 50]. Composite printers from these manufacturers are very similar in operation, with the main differences related to the style of continuous reinforcement material used. The reinforcement used in Markforged printers consists of a bundle of fibers 0.38 mm in diameter bonded together using a binder agent [51]. The fibers pass through a nozzle which has a large flat area that irons the fibers into the previous layer, which could be a fiber or matrix layer. The continuous reinforcement is ironed in a thin tow with a width of roughly 0.9 mm, which can allow for printing of smaller reinforced parts. Unfortunately, Markforged printers are also limited to producing continuous fiber composite parts with relatively low fiber volume fractions. The highest reported fiber volume fractions achieved using Markforged printers are only around 35% [52, 53, 54]. Desktop Metal composite printers instead use a roll of pre-impregnated fiber reinforcement tape, similar to those used in AFP technologies but scaled down in size. These printers feature a compaction roller and a rotating placement head for accurate placement of continuous fiber tapes. The use of larger, 3 mm wide multi-tow tapes results in more efficient printing of reinforced parts. Unfortunately, there is not much information about the volume fraction capabilities of the Desktop Metal Fiber printer at this time, but it is estimated that it will be similar to what is achievable with Markforged printers.

Limited research has been presented on the manufacturing of stiffening grid structures through continuous fiber 3D printing. One study manufactured stiffener grid samples using the

Markforged Mark Two continuous fiber 3D printer [55]. This study also developed an analytical method to obtain laminate stiffness matrices for these stiffened grids. However, the ribs of the stiffened grid structure were printed to be hollow, and only a few layers on the bottom and top of the ribs were made out of the continuous fiber material, considerably lowering the resulting fiber volume fraction of the structure. Another study manufactured a stiffened grid cylinder structure using continuous fiber printing [56]. This study used a modified Makerbot 3D desktop printer, which was retrofitted to be able to print continuous fiber and thermoset matrix composite material. While the printing of the stiffened grid cylinder is promising, limited information was given on the printed structure such as compressive strength or modulus, and thus the actual quality of the structure is undetermined.

1.2.3 Motivation and Objectives

It is clear from the previously discussed information that the current methods to manufacture continuous fiber composite grid stiffened structures suffer from limitations in some aspect. Automated methods like AFP and ATL are able to manufacture grid stiffened structures with high fiber volume fractions yet need complex tooling to form the geometry of the structure. Additive manufacturing methods like continuous fiber 3D printing are able to manufacture grid structures without the need for tooling yet are limited to low fiber volume fractions. A manufacturing method with the ability to make high quality continuous fiber grid stiffened structures without the need for tooling could significantly increase the efficiency and decrease the cost to produce these structures. The current study proposes the use of a novel additive manufacturing method which uses a commingled feedstock and features in situ consolidation to produce grid stiffened structures without the need for tooling. Several stiffener ribs and stiffener rib intersections were produced and tested for composite quality. The fiber volume fraction and

void volume fraction through the height of printed stiffener ribs and intersections was analyzed to determine if the quality of printed trusses was consistent through the thickness. The quality of stiffener ribs prepared using different processing parameters was compared and qualitatively analyzed. To direct this research effort, the scope of the investigation will be defined by the following hypothesis: *Through the use of direct digital manufacture high quality continuous fiber reinforced high aspect ratio grid stiffeners and grid stiffener intersections can be produced from glass fiber thermoplastic matrix commingled tow feedstock with radically reduced tooling requirements.*

2 Experimental

In this chapter, an experimental plan is described for the purpose of testing the previously stated hypothesis by manufacturing and evaluating the quality of direct digital manufactured continuous fiber high aspect ratio grid stiffeners and grid stiffener intersections. This work builds off previous efforts from this research group on low profile beams. To reduce tooling requirements a custom FDM style composite placement system was utilized for sample fabrication. Commonly used composite evaluation techniques including constituent volume fraction analysis and micrograph inspection were determined to be essential for analyzing the quality of manufactured samples. For these high aspect ratio samples, it was further decided that the constituent volume fraction testing should take place as a function of height and position to detect if variations in quality were present. In addition, consolidation force testing was determined to be of importance for quality analysis of manufactured samples, as further elaborated below.

2.1 Composite Placement System

To manufacture continuous fiber reinforced thermoplastic composites (CFRTP), a custom dual gantry FDM style composite placement system was used, which is shown in Figure 8. This system was built for prior research which demonstrated the ability to use the machine to manufacture high quality, high fiber volume fraction continuous fiber composites [57, 58]. The system was designed with two print heads such that one print head can place a composite feedstock and the other can print neat thermoplastic. For the extent of this study only the composite placement print head was used. The movement of both gantries is powered by stepper motors, which are controlled using an Azteeg X3 Pro microcontroller. This microcontroller was specifically chosen because it can accommodate eight stepper motor drivers. In addition to the

stepper motors, this microcontroller also controls all associated heat elements and temperature sensors used in the system, which includes thermal control of both print heads and a heated bed.

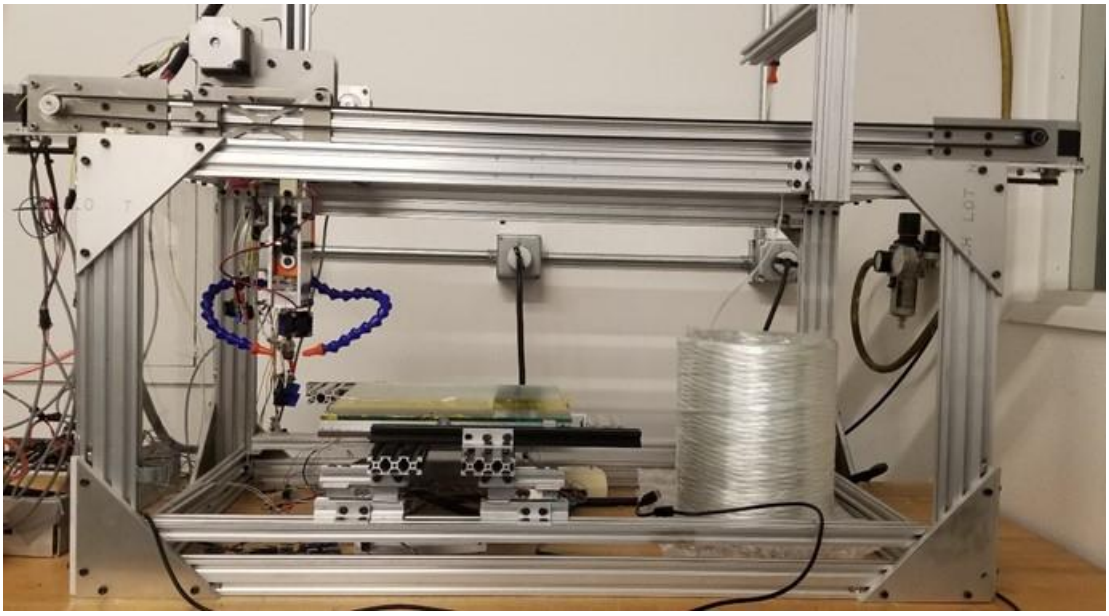

Figure 8: Custom designed FDM style composite placement system.

2.1.1 Spring-Loaded End Effector

The composite print head on this machine is a custom spring-loaded placement head which is shown in figure 9. This placement head was designed with the system during prior graduate research and was utilized for this study [58]. A set of 4 rubber rollers pinch an extruded aluminum Z-axis shaft and restrict the placement head compression movement to be purely vertical. The placement head features a steel compression spring with a known spring constant of about 7.5 N/mm. Controlling the consolidation force applied by the composite placement system is done by simply coding the print head to position itself below the top surface of the print bed. The magnitude of the distance the head is positioned past the surface of the print bed can be

assumed to be the distance that the spring will compress, and by using the known spring constant a compression force can be calculated.

Implementation of the compression spring has two purposes. Firstly, the known stiffness coefficient of the spring allows for the application of a known compression force during printing. Secondly, the spring helps equilibrate the application force applied when printing over any slight variations in the bed level or surface smoothness that may be present. Printing with a known, consistent consolidation pressure should, in theory, produce samples that have uniform material compaction. Because material compaction has a large effect on composite quality in the form of void reduction and reinforcement distribution, samples printed with uniform compaction should exhibit uniform quality. Prior graduate research explored quality analysis of samples printed using different printing parameters and demonstrated the effect that printing with different consolidation forces had on the composite quality [59].

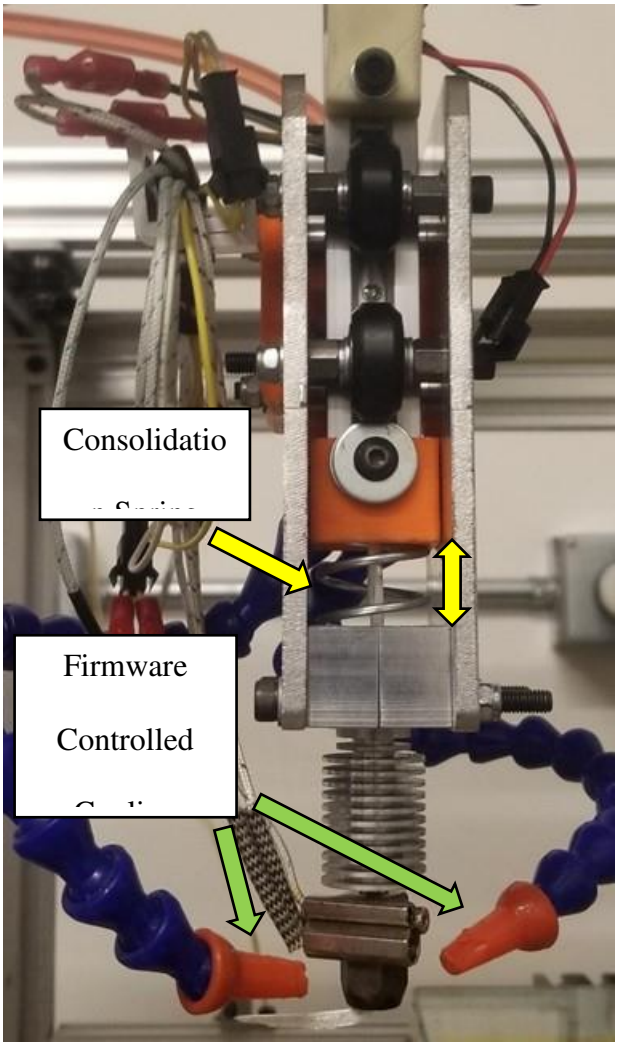

Figure 9: Composite placement print head with compression spring consolidation and firmware controlled cooling system.

2.1.2 Custom Placement Nozzle

A custom EDM machined brass nozzle was designed and implemented during the construction of the system for prior graduate research [57, 58]. The nozzle was implemented to assist with both heat transfer and material compaction during printing. The geometry of the nozzle is shown in figure 10. The interior geometry of the nozzle has a smooth double taper to initially compact the commingled feedstock and to ensure that all the thermoplastic fibers have

melted. Smooth radii have been machined at the nozzle exit to minimize the abrasion inflicted on the fibers as they exit the nozzle. The nozzle has a large bottom surface area to ensure that the entire width of a printed tow is compacted. Additionally, the large surface area grants the ability to explore tow spreading through manipulation of the applied consolidation force. Tows spreading using this method would only be limited by the outer diameter of the flat face which is 11.42 mm.

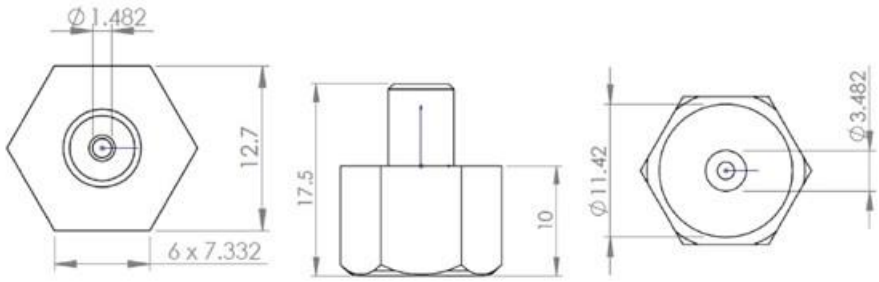

Figure 10: Custom EDM machined nozzle geometry [33].

2.1.3 Firmware Controlled Cooling System

A firmware controlled cooling system was implemented during previous graduate research to allow for active control of the nozzle temperature during printing and is shown in figure 9 [57]. The cooling system consists of a pneumatic compressed air manifold which can be activated directly by the control board. Compressed house air is fed through rubber hoses to two plastic nozzles which can be freely manipulated to direct cooling air wherever needed. Obstructing this path is a solenoid valve wired to the control board which can be opened and closed with gcode. The solenoid valve was installed such that including an “S” parameter as part of any “G1” linear move command will activate or deactivate the solenoid and open or close the valve.

The implementation of the firmware controlled cooling system was important for producing non-geodesic print paths. When the commingled feedstock is heated, the thermoplastic fibers pass their glass transition point and drastically lower in viscosity, allowing the plastic to flow around and between the reinforcement fibers. If the temperature of the liquid thermoplastic is raised, the viscosity of the plastic drops further allowing it to flow around and between the reinforcement fibers more freely. The higher the temperature, the lower the viscosity of the thermoplastic, and the easier it is for the thermoplastic to wet out all of the reinforcement fibers and reduce voids. However, higher temperatures also allow for more tow shearing and reduce the tackiness of the material. This can be an issue when trying to print curved paths, as the tension on the laid reinforcement fibers from the placement head can pull the fibers through the lower viscosity thermoplastic and shift them off of their intended position. During prior graduate research the firmware controlled cooling system was implemented to solve this problem. When printing straight lines, the cooling was not necessary and was turned off to keep the nozzle temperature high. When making a turn, the cooling was turned on and the nozzle temperature was lowered. When the temperature is lowered, tow shearing is reduced, and the tackiness of the placed composite is increased. This results in an increase in positional fidelity as the material is able to rigidize faster and form a bond to the previous layer or bed substrate more quickly.

2.1.4 Feedstock Material

The material used was a Compofil PET-70-R2690N commingled roving hybrid yarn supplied by Jushi [60]. The commingled roving was composed, by weight, of 70% E-Glass reinforcement fibers and 30% PETG thermoplastic fibers, equating to an unprocessed fiber volume fraction of 55%. The commingled roving used for this study had a linear textile density

of 2690. Commingled rovings are typically manufactured such that small clusters of smaller diameter reinforcement fibers are surrounded by larger diameter thermoplastic matrix fibers, as shown in figure 11. It should be noted that the actual cross-section of a commingled roving is not circular, but rather flattened and more similar to a wide ribbon. As discussed above, commingled feedstock can have a much higher fiber volume fraction than available in commercial continuous fiber 3d printer feedstock material.

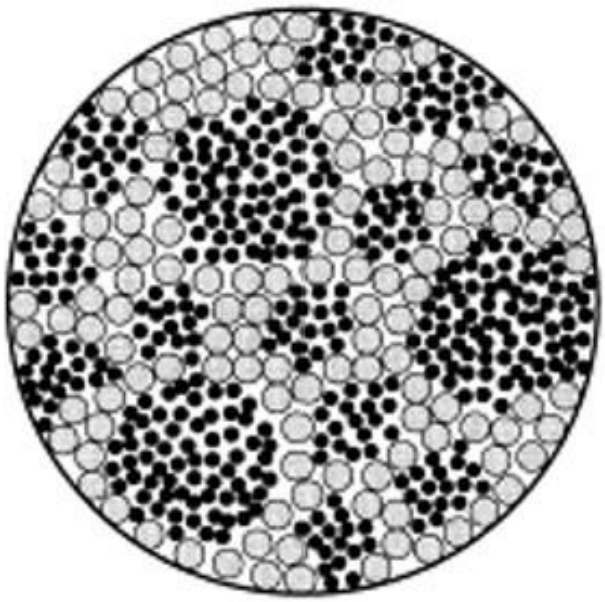

Figure 11: Representative cross-section of the commingled feedstock.

2.1.5 Path Generation

To generate the print paths, hand-written G-code was used. Because the mechanics of the composite placement system required continuous print paths, a conventional slicer program used for 3D printing could not be used. Slicer programs generate G-codes that have discontinuous print paths which include print head traverse movements where no material is extruded. Instead,

prior to the move the neat thermoplastic filament is retracted a small distance back into the nozzle to avoid excess material stringing during the move. This approach is effective for additive manufacturing methods that feature motorized feed mechanisms but cannot be used with the composite placement system due to its pultrusion style method of material deposition. Furthermore, if a specialized slicer designed for continuous fiber was used, like the ones used by MarkForged continuous fiber 3D printers, the fiber paths would be predefined by the slicer program and may not have the desired orientation.

2.1.6 Consolidation Force Measurement System

An important modification that was made to the composite placement system over the course of this study was the implementation of a consolidation force measurement system. This system is comprised of 4 cantilever load cells supporting the print bed, as shown in figure 12. All four load cells are controlled by a single Arduino microcontroller, which is interfaced with a computer to display and record the load cell measurements. The microcontroller is programmed to output a summation value of the 4 load cells. Using two different calibration weights of known mass, the accuracy of the system was found to be ± 5 g. Additionally, no noticeable variation in load measurement was detected when positioning the calibration weights at different locations on the print bed.

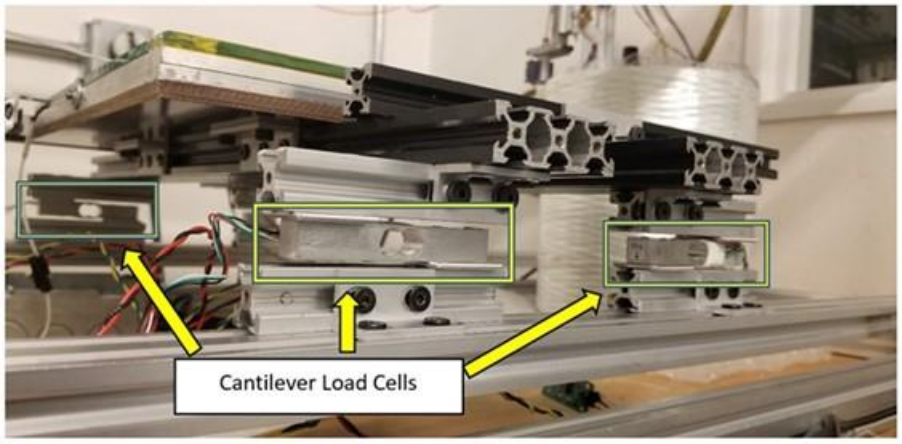

Figure 12: Consolidation force measurement system comprised of cantilever load cells supporting the print bed.

This system was installed to gain a better understanding of the consolidation force applied during printing. To determine the printing consolidation force for early experiments, the known spring constant of the steel compression spring was multiplied by the distance that the outlet of the nozzle was programmed to be positioned past the surface of the print bed substrate. This approach, while sufficient for initial testing, was somewhat inaccurate as it assumes that the rest of the composite placement system hardware has infinite stiffness, and only the spring compresses during consolidation. In addition, early experimental efforts of printing high aspect ratio structures used a constant layer height in the G-code such that the placement head would shift up the same distance for each subsequent print layer. While it was determined that this approach was able to produce the desired print structures, it was also assumed that the consolidation force most likely varied between print layers. The Consolidation Force Measurement System was used to analyze the variation that occurred between each print layer of the samples.

2.2 High Aspect Ratio Stiffener Ribs

To manufacture tall, narrow stiffeners, a continuous print path was used to allow for fully autonomous manufacturing. Simply printing a single beam would require manual cutting and placing of the fibers for every print layer. This method was used in the previous efforts to produce low aspect ratio beam samples [59], however it is much less feasible for producing high aspect ratio beams featuring 10 times the layer count. Instead, a single loop print path was developed which featured two straight sections to be used to harvest straight beam specimens, shown in figure 13. Each of the straight beam sections was 120 mm long. The print path featured large shallow turns, of nominally 50 mm radius, in an attempt to maintain placement fidelity and minimize the effects that turning may have on the quality of the composite. The final loop print samples consisted of 80 print layers and took roughly 19 hours to complete.

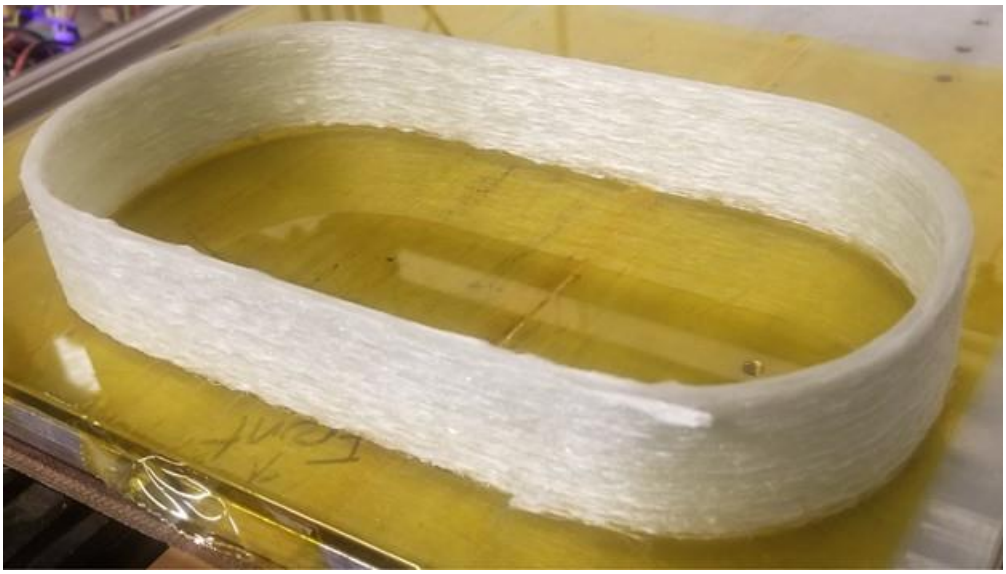

Figure 13: 80 layer high height to width aspect ratio stiffener rib loop print sample.

For this study process parameters were developed based on prior research findings coupled with early experimentation using the composite placement system [57, 58]. The initial

consolidation force was programmed based on values used in prior research and was set to be about 10 N [59]. The composite placement head was set to 270 °C and the print bed was set to 72 °C which was just above the glass transition temperature median value previously determined. In contrast with previous research with this system, the print speed was reduced to 50 mm/min. Early testing with the composite placement system revealed that reducing printing speed both improved the quality of the composite and the placement fidelity of multi-layer curved print path sections.

A total of three different 80 layer loop print samples were manufactured and analyzed. Two loop print samples were manufactured prior to the installation of the Consolidation Force Measurement System and featured different programmed layer heights. The first featured a programmed layer height of 0.4 mm and the second featured a programmed layer height of 0.5 mm. A programmed layer height of 0.4 mm was used on the first sample because it was equal to the layer height used in prior research with the system. A programmed layer height of 0.5 mm was used to explore the effects that increasing the layer height would have on the quality of the stiffener beam through its height. Figure 14 shows a comparison of the final height of the two stiffener beam print structures.

Figure 14: Comparison of final height of 0.5 mm layer height (left) and 0.4 mm layer height (right) loop print samples.

2.2.1 Stiffener Rib Volume Fraction Measurement

From each of the two 80 layer printed loop samples a straight beam was isolated and used for testing. The straight beam cut from the 0.4 mm layer height loop print sample was nominally 5 mm wide by 30 mm tall by 120 mm long. The straight beam cut from the 0.5 mm layer height sample was nominally 4.5 mm wide by 39 mm tall by 120 mm long. Quality analysis of the composite stiffener beam was performed by finding the fiber volume fraction and the void volume fraction of these straight beam segments. The location of the straight beam section taken from the loop prints is shown in red in figure 15.

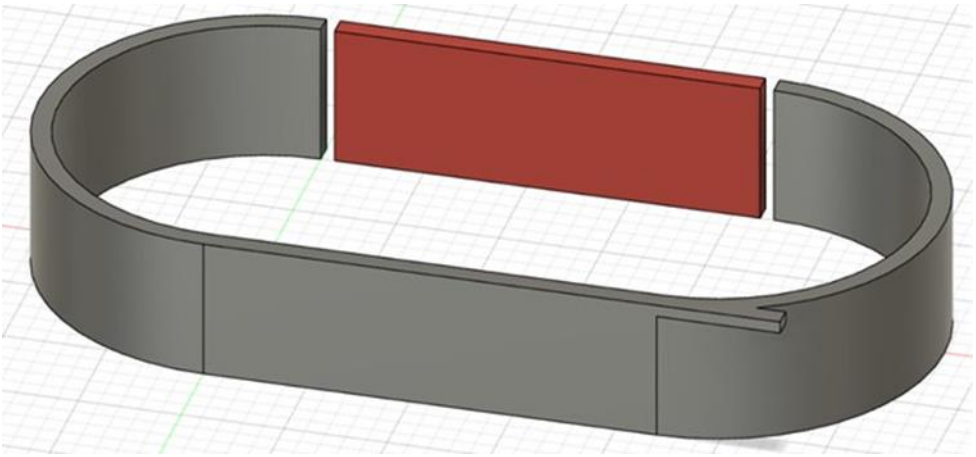

Figure 15: Location of the straight stiffener rib section taken from the loop print samples for testing.

To detect if variations in quality through the length or height of the beams were present, multiple specimens were taken and tested from different positions on the beams. Using a water cooled diamond saw, the beams were cut into 5 sections along the length, as shown in figure 16. It should be noted that the print direction of the loops was counterclockwise. Therefore, the

section that occurred first along the print path was labeled Section 1, and the section that occurred last along the print path was labeled Section 5. Furthermore, it should be noted that Section 1 occurred immediately after a turn in the fiber path, and Section 5 occurred immediately before the next turn in the path.

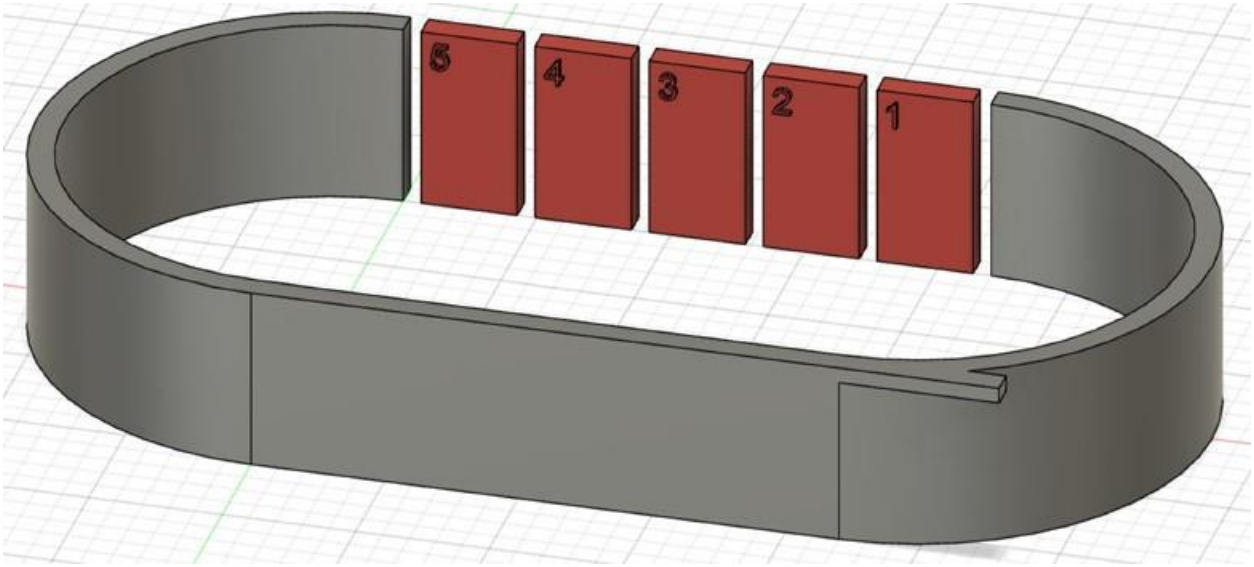

Figure 16: Location and label of the 5 sections along the length of the straight stiffener beam used for testing.

Each section was then divided into 8 specimens through the height, as shown in figure 17, using a water cooled laboratory precision diamond saw. It should be noted that specimens were labeled by their section followed by their position through the height of the section. Specimen labels were in the form of a section number, from 1 to 5, followed by a position letter, from a to h. The position letters were used to label the 8 specimens which were taken from each section. Specimens were labeled such that specimens labeled with “a” were taken from the bottom of each section, or from the initial print layers closest to the heated print bed, and

specimens labelled with “h” were taken from the top of each section. Individual labels for each specimen can be seen in figure 17.

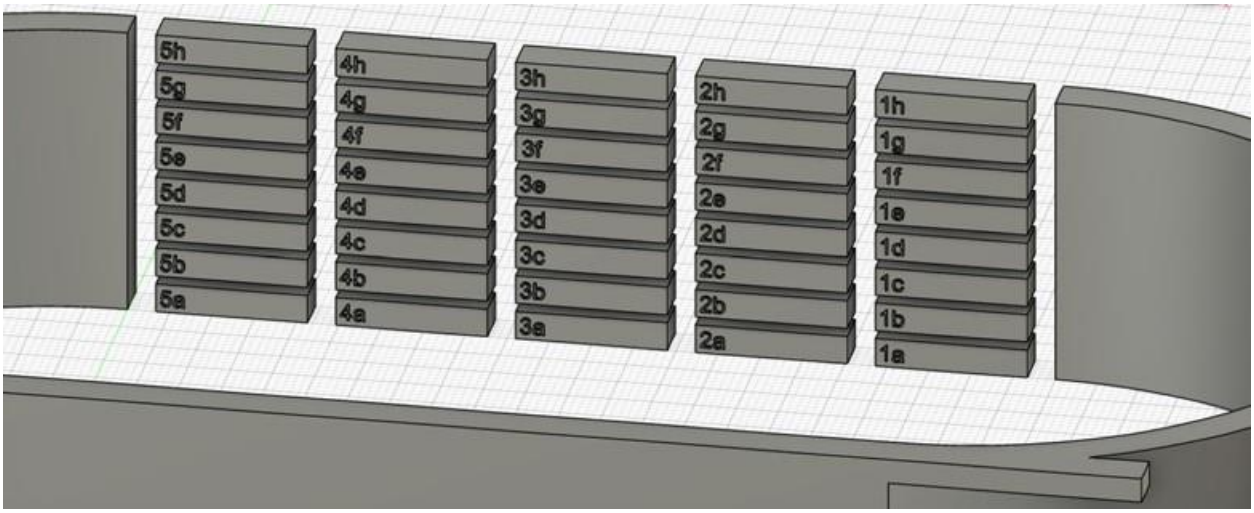

Figure 17: Location and label of the individual specimens of the straight stiffener ribs.

To find the volume fraction of stiffener beam specimens, first the volume of the specimens needed to be determined. These printed structures exhibited a rough texture on the sides of the print. However, no modifications to the specimens such as sanding or polishing were performed to preserve the as-printed properties of the specimens. A close-up image of the rough sides of the printed stiffener beam samples is shown in figure 18.

Figure 18: Close-up image of the as-printed rough texture of the walls of the stiffener rib samples.

The volume of the specimens was determined using a fluid displacement method based on ASTM D792 [61]. The mass of each sample was weighted, in air, using a laboratory precision scale accurate to 10 micrograms. Then the mass of each sample, submerged in a solution of known density, consisting of 1 part RedLine Water Wetter surfactant and 32 parts deionized (DI) water, was measured using a hanging basket apparatus, shown in figure 19. The rough sides of the samples tended to trap air bubbles which would alter the submerged mass data, as shown in figure 20. The surfactant was added to the DI water to lower the surface tension in an attempt to minimize the formation of air bubbles on the sample surfaces.

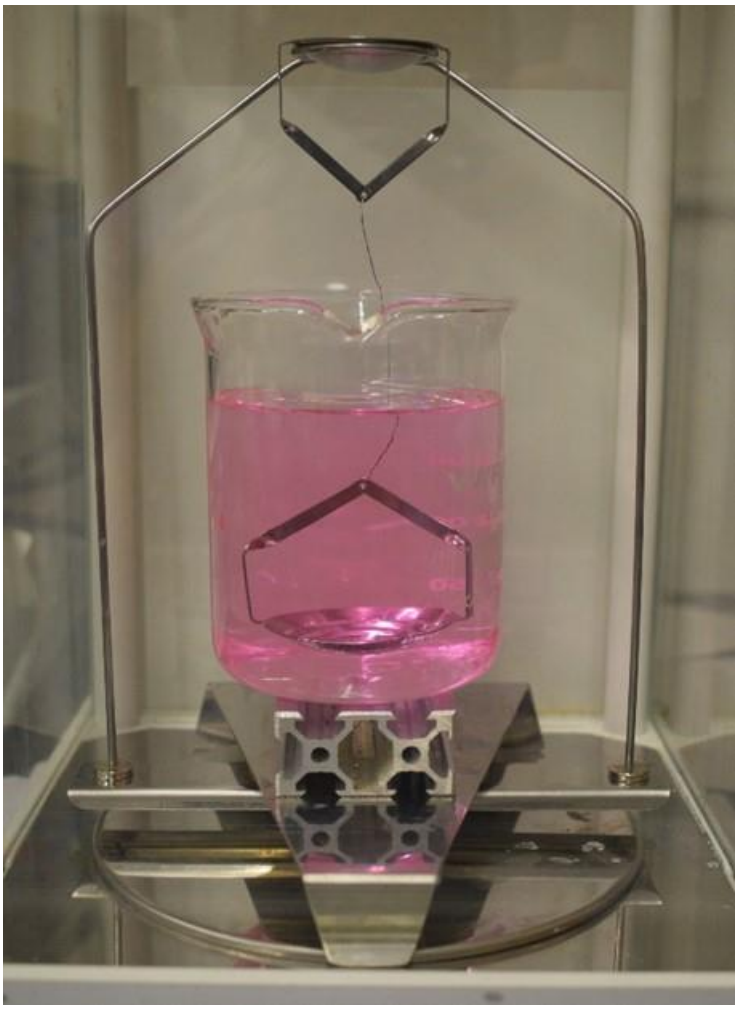

Figure 19: Hanging basket apparatus used to measure submerged mass of specimens.

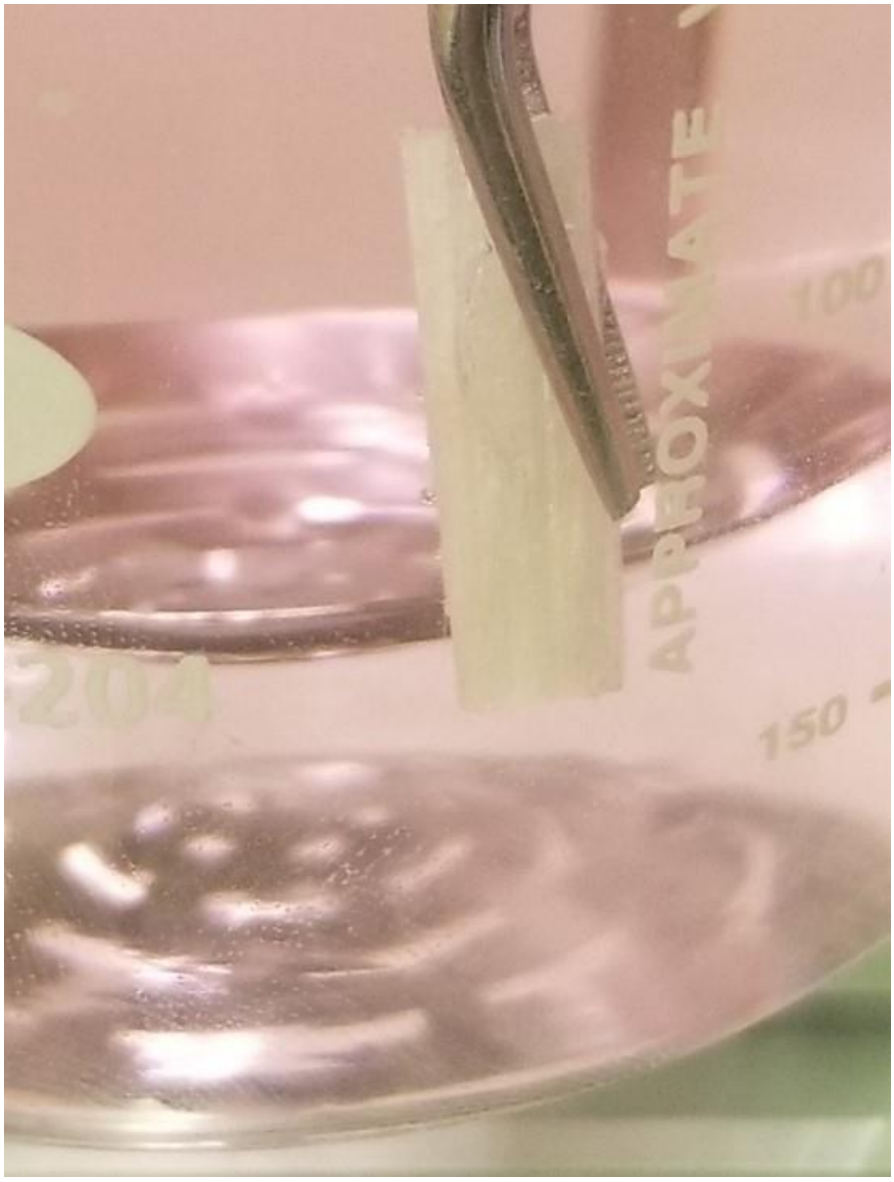

Figure 20: Image of air bubble clinging onto the side of one of the specimens.

Through the Archimedes' principle it can be stated that the weight of a submerged object is reduced, due to buoyancy effects, by its volume multiplied by the density of the fluid. Using this principle and the measured dry mass and submerged mass of each sample, the volume and density of each sample was calculated using equation 1 and 2. Finally, a relative density percentage was found by dividing the sample density calculated using Archimedes' principle by

the unprocessed density of the commingled feedstock. The unprocessed density of the commingled material was determined using the known density of the constituent materials and the rule of mixtures. The constituent material densi

ties were supplied by the manufacturer and are given in Table 1. The Rule of Mixtures equation is shown in Equation 3. The calculated unprocessed density using the constituent material densities supplied by the manufacturer and the Rule of Mixtures equation was determined to be 1.974 g/cm^3.

$$V_s = \frac{(m_d - m_w)}{\rho_f} \tag{1}$$

$$\rho_s = \frac{m_d}{V_s} \tag{2}$$

$$\rho_c = \rho_f V_f + \rho_m V_m \tag{3}$$

Where:

V_s = volume of sample

m_d = mass of dry sample

m_w = mass of wet (submerged) sample

ρ_f = density of submerging fluid

ρ_s = density of sample

ρ_c = density of composite

ρ_f = density of fiber (reinforcement) material

V_f = volume of fiber (reinforcement) material

ρ_m = density of matrix material

V_m = volume of matrix material

Table 1: Constituent material density values of the commingled tow given by manufacturer.

Commingled Feedstock Material Densities		
Material	**Density**	
	g/cm^3	oz/in^3
PETG	1.27	0.734
E-Glass Fibers	2.62	1.514

To determine the fiber volume fraction and void volume fraction of the E-glass fiber reinforced PET specimens, a matrix burn off test was performed according to ASTM D3171-15 [62]. Specimens were placed in ceramic crucibles and positioned in a furnace. The furnace temperature was then raised to 600 °C and the specimens were kept at that temperature for at least 2 hours to ensure that the matrix was completely removed. After the furnace was turned off and cooled to room temperature, the crucibles containing the specimen fibers were again placed into the 70 °C drying oven with desiccant for 1 hour. The mass of the reinforcement fibers for each specimen was measured using the precision laboratory scale. The mass of the matrix was then determined by calculating the difference between the total specimen dry mass and the mass of the reinforcement fibers. The volume of the fibers and the matrix were determined by dividing the previously determined masses by known constituent material densities of the commingled material given by the feedstock manufacturer. The given constituent material densities for the E-Glass fibers and the PET matrix fibers were 2.62 g/cm^3 and 1.27 g/cm^3, respectively. To determine the volume of voids in the samples, the volume of the reinforcement

fibers and the matrix were subtracted from the measured volume of the samples found during Archimedes' testing. Finally, the fiber volume fraction and void volume fraction of each sample was determined by dividing the calculated volume of the reinforcement fibers and the voids by the total volume of the sample.

2.2.2 Stiffener Rib Microscopic Inspection

A micrograph evaluation was performed on the high aspect ratio stiffener rib composites to qualitatively evaluate the reinforcement distribution, determine the void locations, and to support the constituent material concentration measurements. Due to the complete consumption of the matrix in burn off testing, micrographs of constituent content tested specimens could not be obtained. Thus, specimens were taken from material adjacent to that which was used for constituent content testing. Short specimens were cut from the remaining loop print material using a diamond saw, as shown in yellow in figure 21. The specimen taken next to the start of the straight section was labeled "S" and the specimen taken next to the end of the straight section was labeled "E". It should be noted that the side of the specimens that were polished and imaged was the side adjacent to the constituent content testing specimens, suggesting that the micrographs are consistent with the microstructure of the beginning and end of the stiffener rib samples. The specimens were suspended in an acrylic mounting media which was left to cure for 24 hours before polishing. Specimens needed to be cut in half through the height to fit into the acrylic mounting mold. Polishing was performed by hand using polishing wheels and various grinding and polishing media, with a final polishing step utilizing a 0.05 micron colloidal silica suspension.

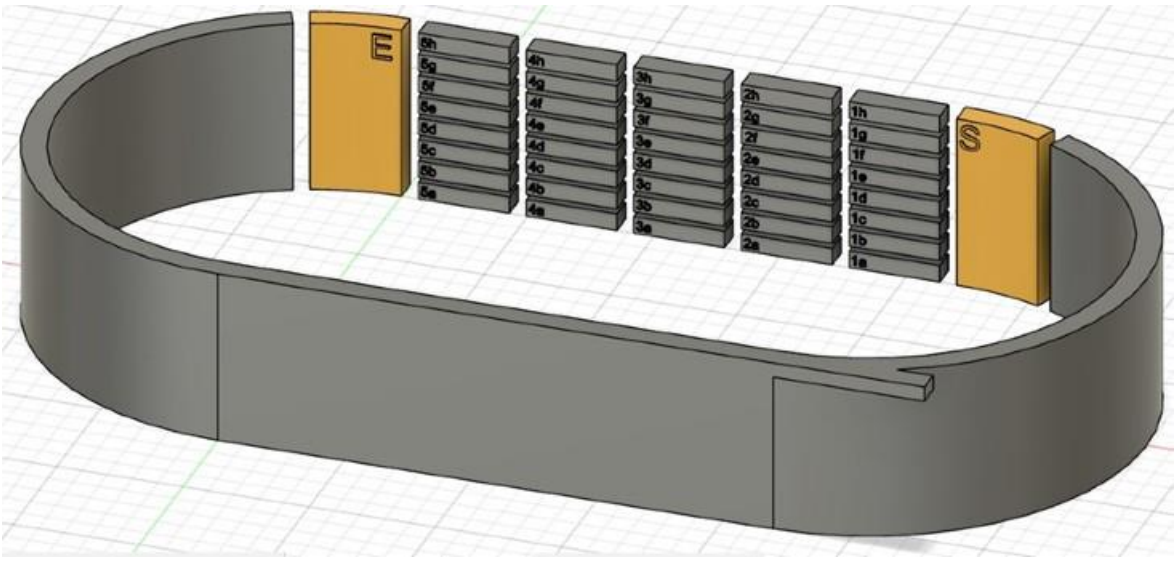

Figure 21: Location and label of microscopic inspection specimens taken from extra material of the loop print samples.

2.2.3 Stiffener Rib Consolidation Force Measurement

To better understand consolidation force experienced during printing of the high aspect ratio stiffener beam, a third high aspect ratio stiffener beam loop sample was digitally manufactured while measuring the consolidation force using the consolidation force measurement system. Due to the consolidation force measurement system being installed after the manufacturing and testing of the original 0.4 mm layer height and 0.5 mm layer height stiffener rib loop print samples, an additional loop print sample needed to be manufactured to test with the system. This beam sample was manufactured with the same process settings used to manufacture the original 0.4 mm layer height sample. The consolidation force was measured and recorded during the full manufacturing time.

2.2.4 Force Measured Stiffener Rib Volume Fraction Measurement

A constituent volume fraction analysis was performed on the consolidation force measured high aspect ratio stiffener rib loop print sample. This was done to form a relationship between constituent volume fraction and measured consolidation force during printing where all data was collected from the same print sample.

The consolidation force measured loop print sample was printed using the same process parameters as were used to manufacture the first 0.4 mm layer height stiffener rib loop print sample. Because an extensive constituent volume fraction analysis had already been performed on the first 0.4 mm layer height sample, it was determined that a reduced analysis would be sufficient for the consolidation force measured sample. Therefore, a reduced number of specimens were procured from the sample and only specimens from section 1 and 5 were analyzed. The location and labelling of the specimens taken and analyzed from the consolidation force measured loop print sample are shown in figure 22. It should be noted that, like with the previously discussed volume fraction analysis, specimen labels were in the form of a section number followed by a position letter. Section 1 occurred first along the print path and immediately after a turn, and section 5 occurred last along the print path and immediately before the next turn. Specimens labeled with “a” were taken from the bottom of each section, or from the initial print layers closest to the heated print bed, and specimens labelled with “d” were taken from the top of each section, or from the final print layers furthest away from the heated print bed.

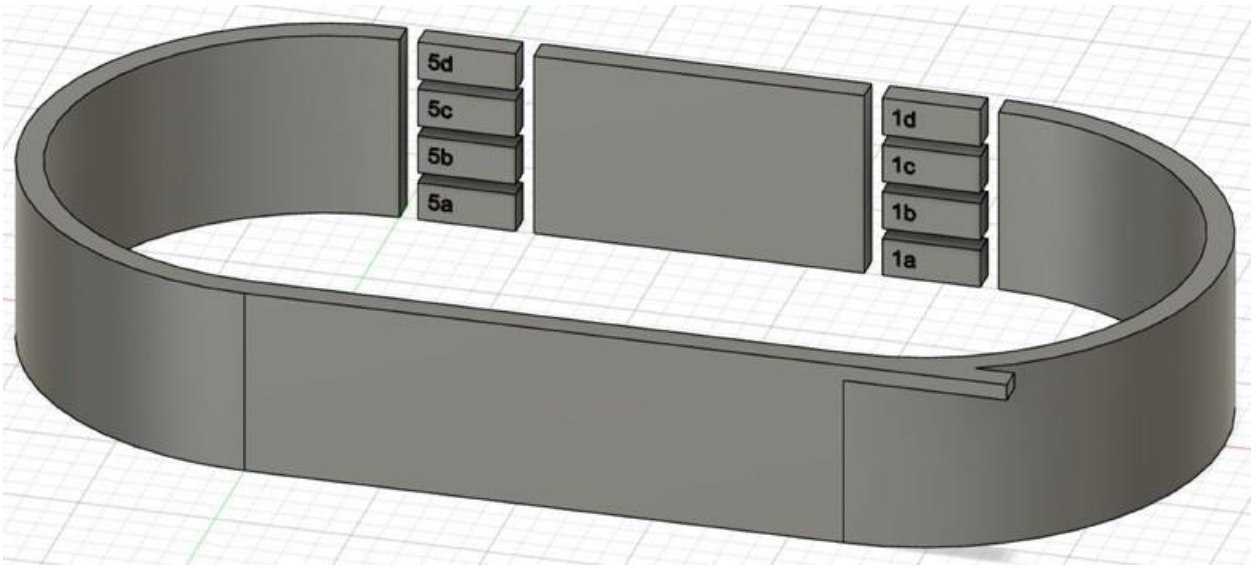

Figure 22: Location and label of specimens taken from the force measured stiffener rib sample.

The exact same testing procedure used to analyze the constituent volume fraction of the 80 specimens taken from the original 0.4 mm layer height and 0.5 mm layer height stiffener rib samples was used to analyze the constituent volume fraction of the 8 specimens taken from the consolidation force measured stiffener rib sample. The volume of the specimens was determined using a fluid displacement method based on ASTM 792 [61]. Then, the matrix material was burned off in a furnace set to 600 °C. Once cooled, the mass of the reinforcement fibers for each specimen was measured and the fiber volume fraction and void volume fraction were calculated using known constituent material densities given by the commingled tow manufacturer.

2.2.5 Force Measured Stiffener Rib Microscopic Inspection

A micrograph evaluation was performed on the consolidation force measured stiffener beam loop print sample to qualitatively evaluate the reinforcement distribution, determine the void locations, and to compare to the results of the constituent volume fraction tests and the consolidation force measurement tests. Like with the first microscopy analysis, the same

specimens tested in the constituent volume fraction tests could not also be used for microscopy as the volume fraction test consumes the specimens. Therefore, extra material from the loop print sample that was adjacent to the stiffener beam portion was used for microscopy. Short specimens were cut from the remaining loop print material using a diamond saw. The specimen taken next to the start of the straight section was labeled “S” and the specimen taken next to the end of the straight section was labeled “E”. The specimens were cut in half to fit in the mounting mold, and then were suspended in acrylic and left to cure for 24 hours before polishing.

2.3 High Aspect Ratio Stiffener Grid Intersections

To demonstrate the ability of the composite placement system to manufacture more complex geometries, a stiffener grid intersection was manufactured and analyzed for composite quality. The stiffener grid intersection sample consisted of two 40 layer stiffener ribs intersecting each other at their midpoint angled 90 degrees from each other. Each stiffener rib was nominally 190 mm in length. Because the print layers were continuous, unbroken print paths, there were 80 print layers at the intersection node of the print sample. The stiffener grid intersection point sample is shown in figure 23.

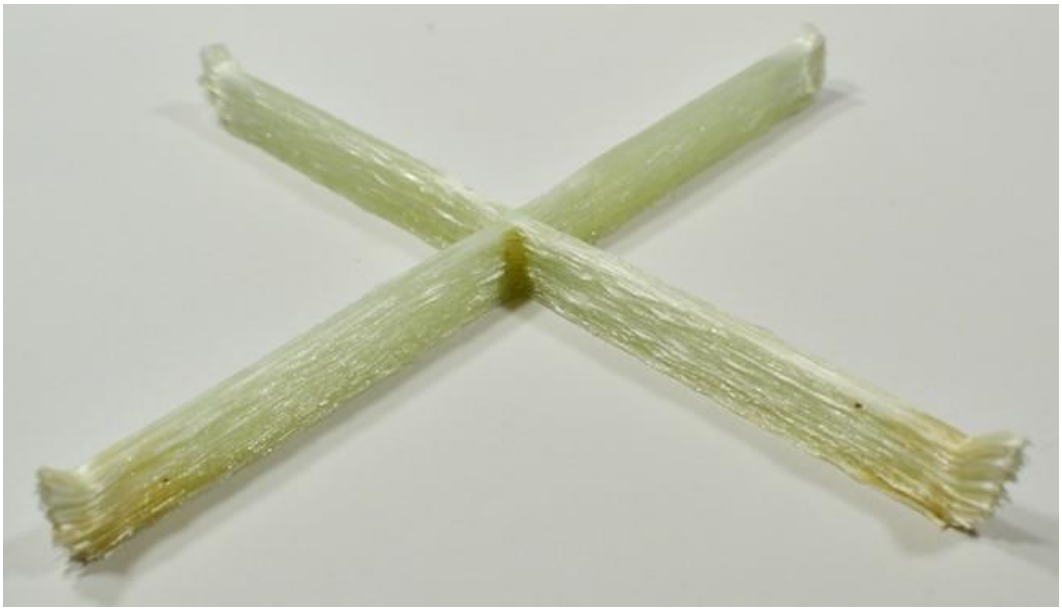

Figure 23: 40 layer stiffener grid intersection sample.

To keep the top surface of the intersection sample flat and reduce buildup at the intersection node, localized tow spreading was used. The tow was locally spread when printing the intersection node of the sample by means of increasing the consolidation force and decreasing the print speed. To print the stiffener grid intersection point, the printer started by printing one of the stiffener ribs using the same process parameters as were used to manufacture the consolidation force measured high aspect ratio stiffener beam. The composite placement head nozzle was set to a temperature of 270 °C and the heated print bed was set to a temperature of 72 °C, just above the glass transition temperature of the matrix material. The initial consolidation force was set to 10 N and the initial print speed was set to 50 mm/min. However, when the nozzle reached a position 5 mm before the intersection node, the Z-axis position was lowered to increase the consolidation force and the print speed was lowered. The initial consolidation force at the intersection node was increased to 20 N and the print speed at the

intersection node was reduced to 20 mm/min. The consolidation force was increased to further compress the print layers and decrease the height of each print layers, forcing the tow to spread out. Doing so allowed the intersection point, which had double the amount of print layers as the rest of the sample, to have roughly the same height as the rest of the intersection point sample. The print speed was reduced to increase the amount of heat that was supplied to the composite material by increasing the amount of time that the heated placement nozzle was in contact with the feedstock material while printing the intersection point. This gave the material more time at low viscosity to flow and spread in response to the increased consolidation force being applied, further increasing the amount of tow spreading exhibited at the intersection node. After printing with an increased consolidation force and reduced print speed for 10 mm, which encompassed the intersection node, the nozzle was then raised to its original Z-axis position which resulted in an initial consolidation force of 10 N and resumed printing at its original print speed of 50 mm/min, finishing one layer of one of the stiffener ribs. Once the stiffener rib print layer was finished, the end was manually cut, and the nozzle then moved to the start of the second stiffener rib location, programmed to be positioned perpendicular to the first stiffener rib and intersecting it at the center of the spread tow region. The same process parameters were used when printing the second stiffener rib, including the increased consolidation force and reduced print speed at the intersection node. This pattern of overlapping stiffener rib print layers continued until all 40 print layers were built up for both of the stiffener ribs, resulting in an 80 layer intersection node in the sample. While a continuous print path could have been used to manufacture the intersection point sample, which would have been shaped similarly to a figure-8 as shown in figure 24, it was determined that manually cutting and placing the material for each print layer would be a better choice. This was determined based on a material shortage as well as the results

of the stiffener beam sample analysis discussed later, which showed that turns in the print path significantly increased the void content in the samples.

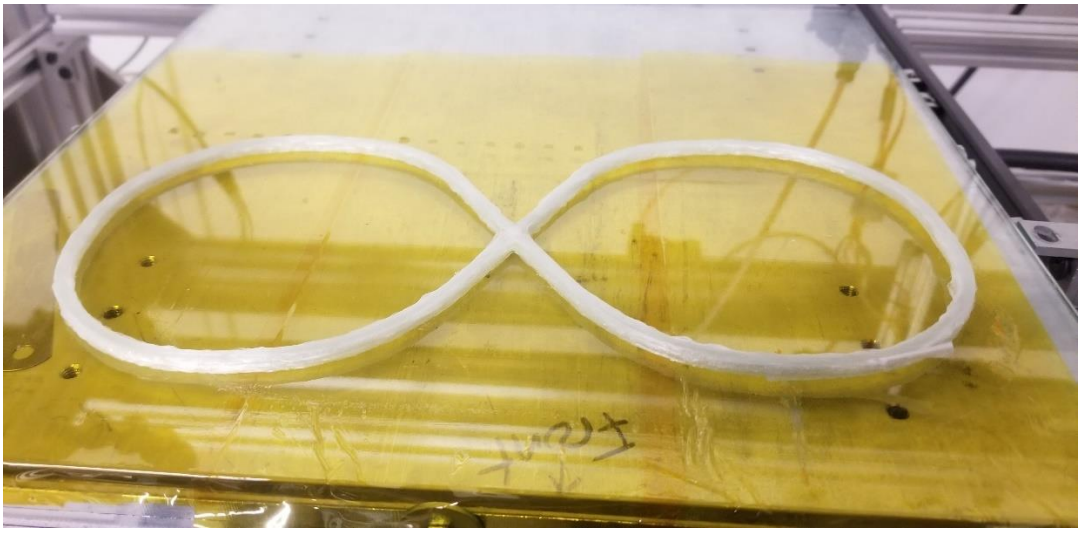

Figure 24: Example of figure-8 print path for intersection point sample manufacturing. This method was not used to manufacture the 40 layer intersection point samples.

2.3.1 Stiffener Grid Intersection Geometry Measurement

To test the effect that the tow spreading procedure used during printing of the stiffener grid intersection point sample had on the geometry of the intersection node, a height and tow width measurement test was conducted on the sample. The height of the sample was measured at 7 different locations. The location and labels of these measurement locations are shown in figure 25. The height at these locations was measured using a 1 inch digital micrometer. Additionally, the width of the sample was also measured at the 7 locations. Both the width of the bottom layer and top layer were measured using calipers.

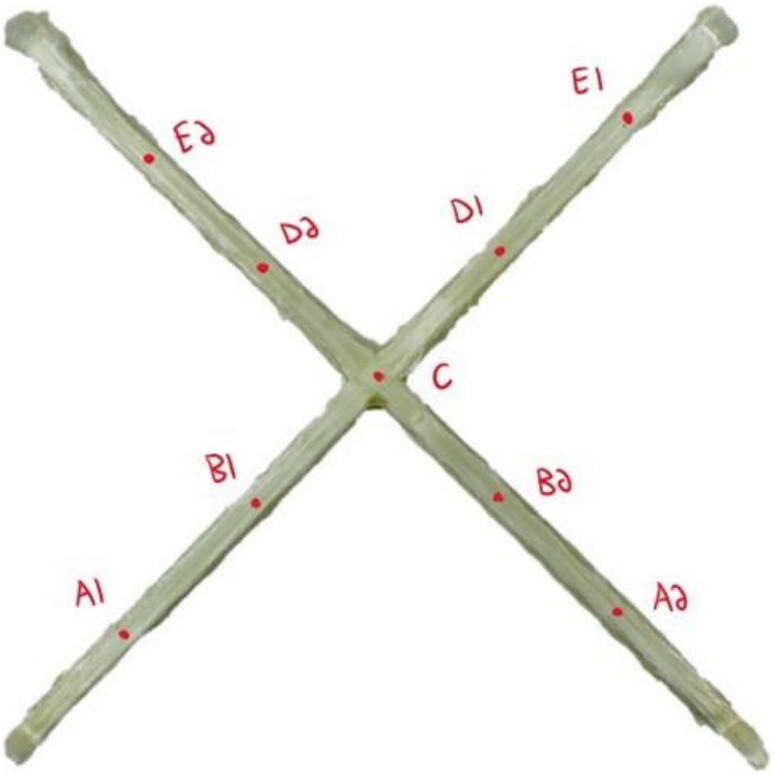

Figure 25: Location and label of geometric measurement positions on the stiffener grid intersection sample.

2.3.2 Stiffener Grid Intersection Consolidation Force Measurement

To better understand the consolidation force experienced during the printing of high aspect ratio stiffener grid intersections, the consolidation force was measured while printing the grid intersection sample using the consolidation force measurement system. The consolidation force was measured during all 40 layers of the print for both stiffener rib directions. Individual consolidation force data sets were gathered for each print layer of each stiffener rib due to the discontinuous printing method used, where the material was manually cut and held for each print layer.

2.3.3 Stiffener Grid Intersection Volume Fraction Measurement

A constituent volume fraction analysis was performed on the grid stiffener intersection sample to analyze the quality of the printed sample. The intersection point sample was divided into several test specimens using a water cooled diamond saw. To maximize the analysis performed on the intersection point sample, it was determined that both a constituent volume fraction analysis and a microscopic inspection should be performed on the intersection node of the sample. Therefore, the node of the sample was isolated and divided diagonally through the center, with one half reserved for pyrolysis and the other half mounted for microscopy. Dividing the sample node diagonally allowed for the position of reinforcement fibers in both fiber directions to be observed on the micrograph analysis specimen. Figure 26 shows the specimens taken from the intersection point sample with their relative positions from the sample.

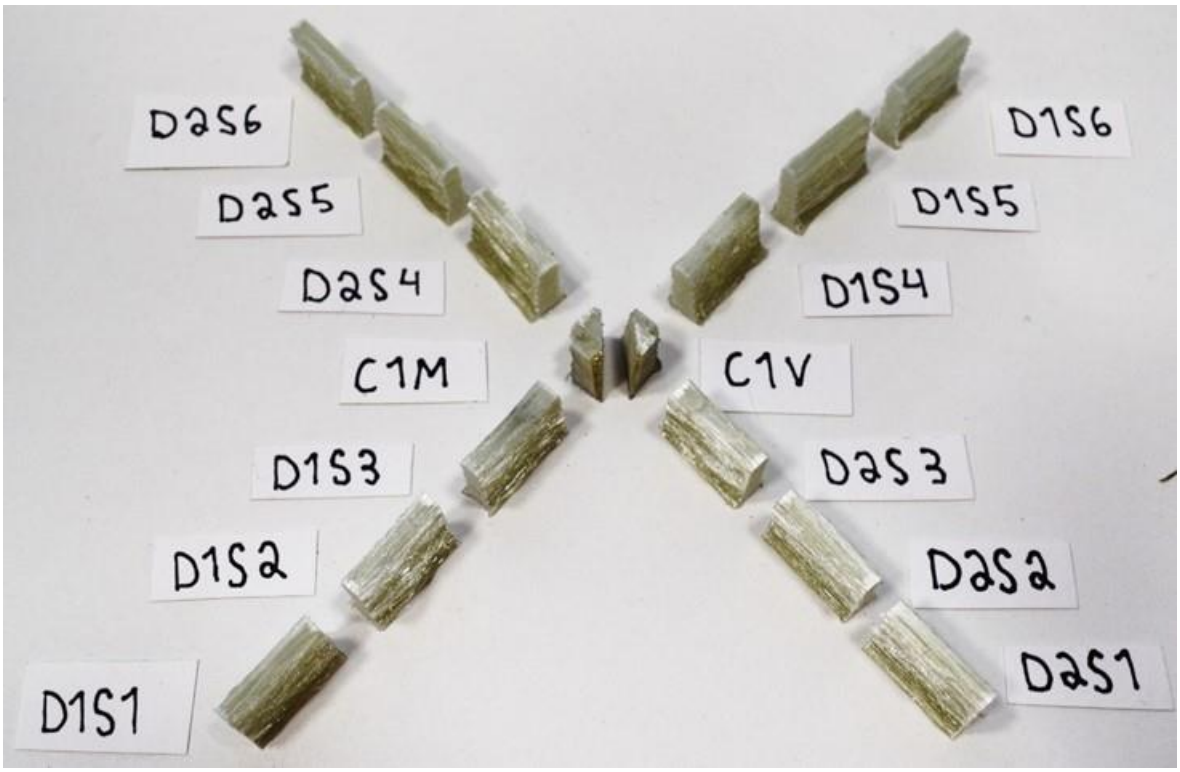

Figure 26: Location and label of specimens taken from stiffener grid intersection sample.

Specimens located on the stiffener rib regions of the intersection point sample were labeled in the form of a direction, either D1 or D2, followed by a specimen location, from S1 to S6. It should be noted that specimens labeled S1 were located at the start of a stiffener rib direction and specimens labeled S6 were located at the end of a stiffener rib direction. The two intersection node specimens were labelled such that the specimen tested for volume fraction analysis was labelled V and the specimen tested for microscopy was labelled M.

The same testing procedure used to analyze the constituent volume fraction of the high aspect ratio stiffener beam specimens was used to analyze the constituent volume fraction of the intersection point specimens. The volume of the specimens was determined using a fluid displacement method based on ASTM 792 [61]. The matrix material was then burned off in a furnace set to 600 C. Once cooled, the mass of the reinforcement fibers for each specimen was measured and the fiber volume fraction and void volume fraction were calculated using known constituent material densities given by the commingled tow manufacturer.

2.3.4 Stiffener Grid Intersection Microscopic Inspection

A micrograph evaluation was performed on the stiffener grid intersection point sample to evaluate the quality of the composite at the intersection node and to support the results of the constituent volume fraction analysis. As shown above, the intersection node of the sample was divided into two halves along the diagonal, with one half reserved for volume fraction analysis by pyrolysis, and the other half reserved for microscopic inspection. The C1M intersection node specimen was mounted in an acrylic which was left to cure for 24 hours before polishing. The surface along the diagonal cut through the middle of the intersection node was the surface that was polished and inspected.

3 Results

3.1 Stiffener Rib Volume Fraction Measurement

The fiber volume fraction and void volume fraction of each section along the length, 1 – 5 of the stiffener rib samples were found by summing the average fiber volume fraction and void volume fraction of the 8 specimens taken through the height of each section. The fiber volume fraction of each section of the 0.4 mm layer height stiffener rib sample are shown in figure 27, and the void volume fraction of each section of the 0.4 mm layer height stiffener rib sample are shown in figure 28. The fiber volume fraction of each section of the 0.5 mm layer height stiffener rib sample are shown in figure 29, and the void volume fraction of each section of the 0.5 mm layer height stiffener rib sample are shown in figure 30.

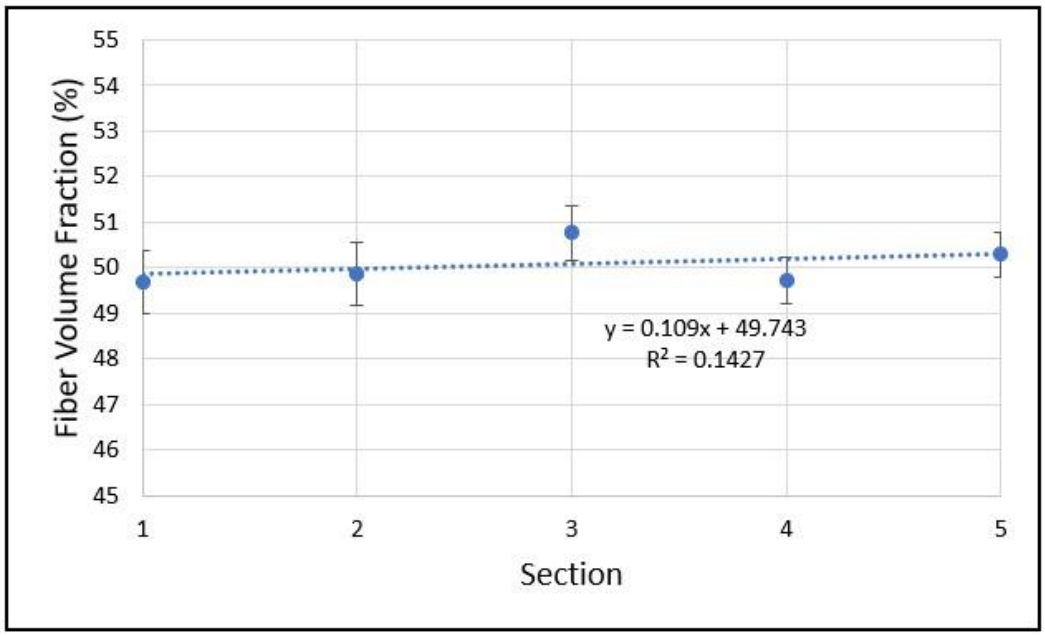

Figure 27: Average fiber volume fraction vs. linear position of 0.4 mm layer height stiffener rib sections.

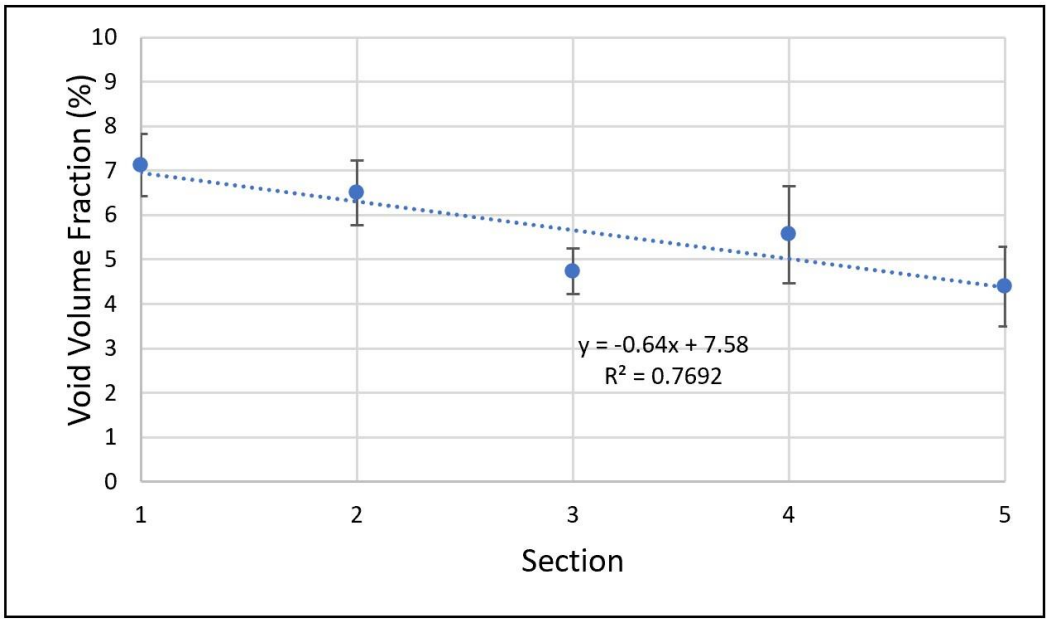

Figure 28: Average void volume fraction vs. linear position of 0.4 mm layer height stiffener rib sections.

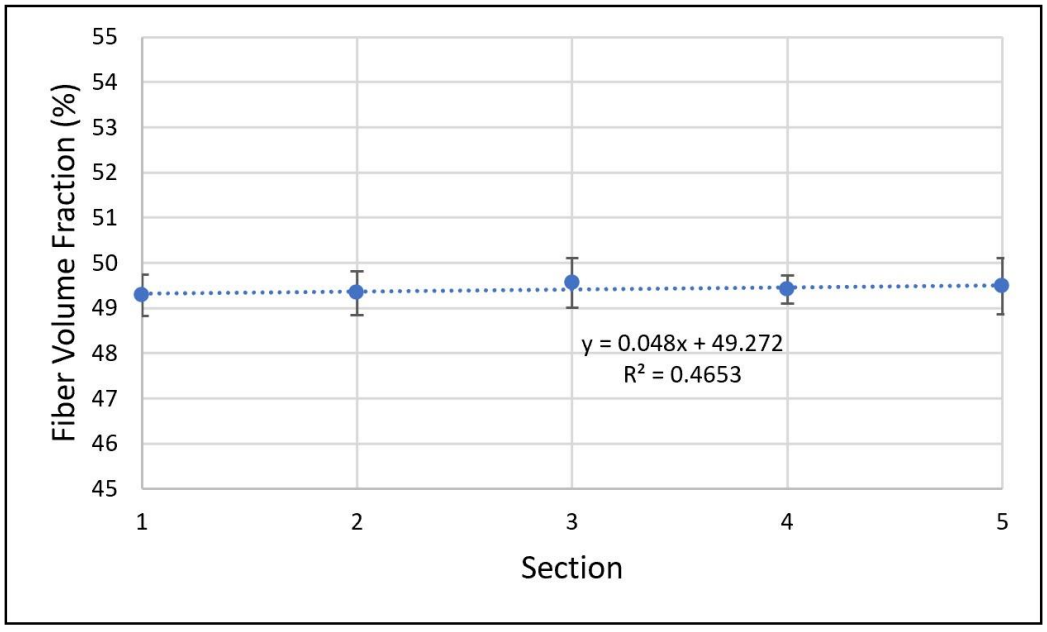

Figure 29: Average fiber volume fraction vs. linear position of 0.5 mm layer height stiffener rib sections.

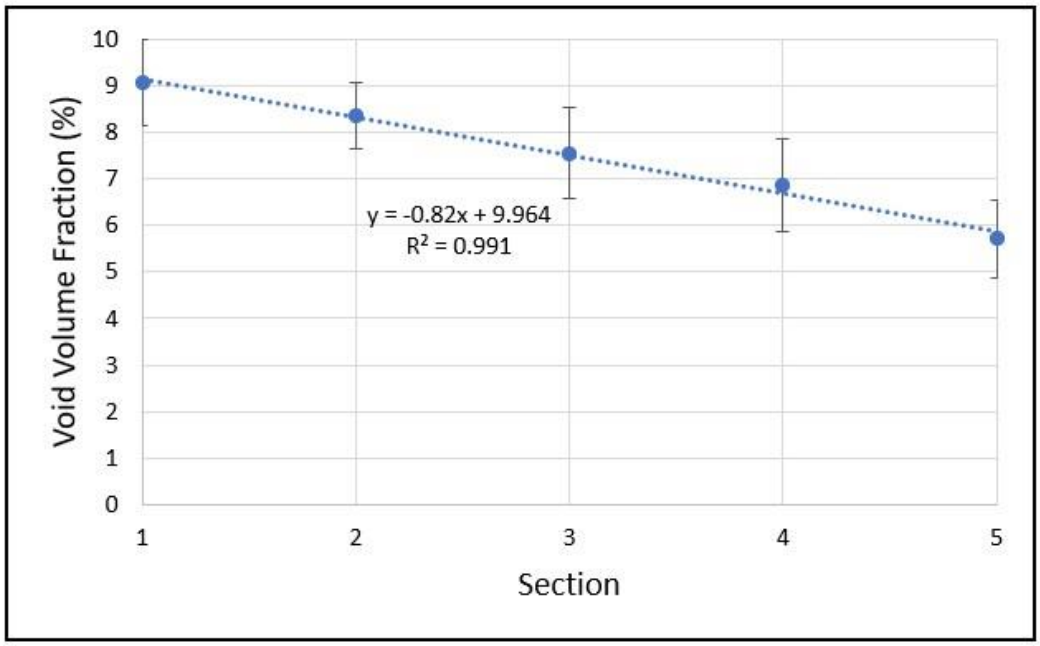

Figure 30: Average void volume fraction vs. linear position of 0.5 mm layer height stiffener rib sections.

The fiber volume fraction results indicate that little variation in fiber content is present between the different sections along the length of both stiffener beams. A small increasing trend in volume fraction is shown in the 0.4 mm layer height stiffener beam linear trendline; however, within the measurement error represented by the error bars, the volume fraction can be considered to be unchanging over the length. The results show that a high fiber volume fraction of around 50 % was maintained over all sections of both of the stiffener beam samples. Unlike the fiber volume fraction results, the average void volume fraction results exhibit clear decreasing trends along the lengths of both the 0.4 mm layer height and 0.5 mm layer height stiffener beams. The void volume fraction results indicate that the void content gradually decreases along the length of the stiffener beams, with the lowest volume fractions reaching

below 5 % in the 0.4 mm layer height beam sample and reaching below 6 % in the 0.5 mm layer height beam sample.

A total of 40 specimens were tested from each stiffener rib sample to examine the relationship between height and the constituent volume fractions of the stiffener ribs. However, only the 8 specimens from section 5 of each stiffener beam will be discussed. These were chosen because they were furthest away from the turns in the print path, so as to minimize any influence that the turns may have on void content and best represent the steady state properties of the printed material. The fiber volume fractions and void volume fractions were determined for each of the 8 specimens through the thickness (height) of the 0.4 mm layer height and 0.5 mm layer height stiffener rib samples. The fiber volume fraction and void volume fraction of the specimens taken from section 5 of the 0.4 mm layer height beam sample are plotted in figure 31 and figure 32. The fiber volume fraction and void volume fraction of the specimens taken from section 5 of the 0.5 mm layer height beam sample are plotted in figure 33 and figure 34.

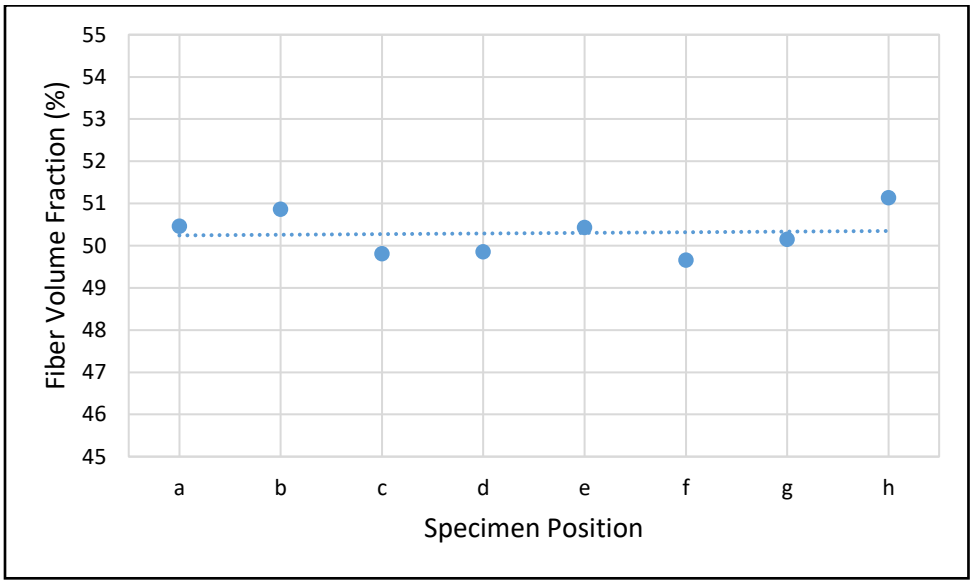

Figure 31: Fiber volume fraction vs. height of 0.4 mm layer height section 5 stiffener rib specimens.

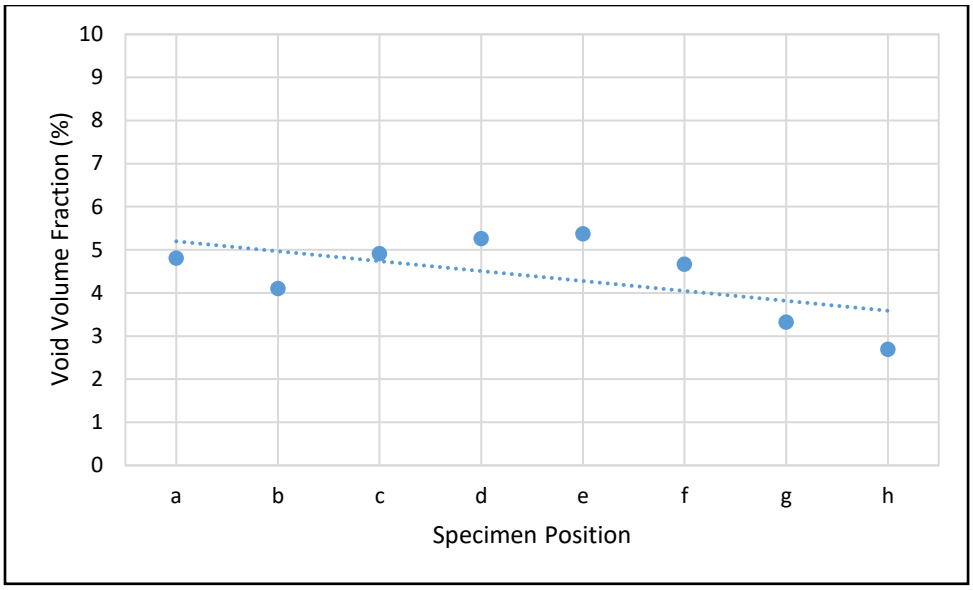

Figure 32: Void volume fraction vs. height of 0.4 mm layer height section 5 stiffener rib specimens.

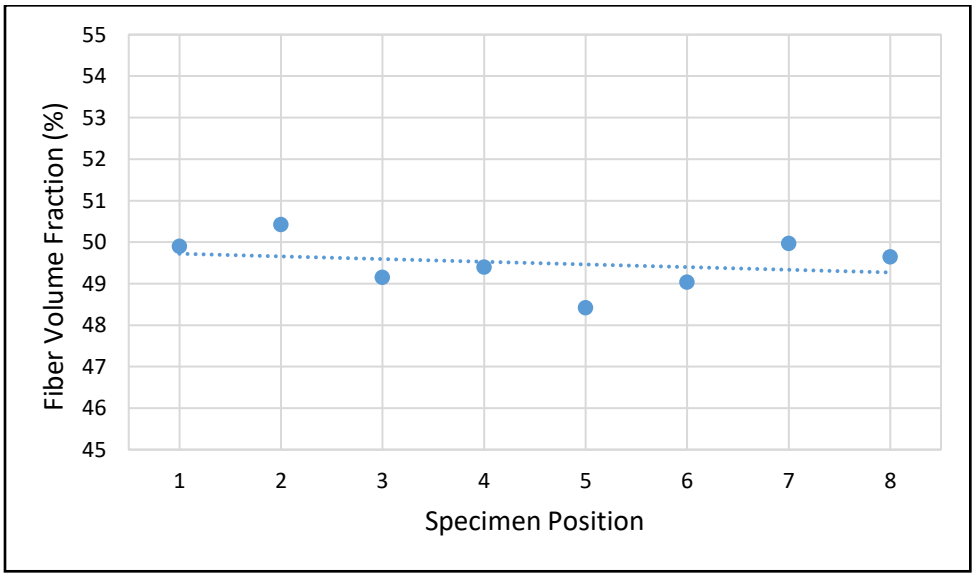

Figure 33: Fiber volume fraction vs. height of 0.5 mm layer height section 5 stiffener rib specimens.

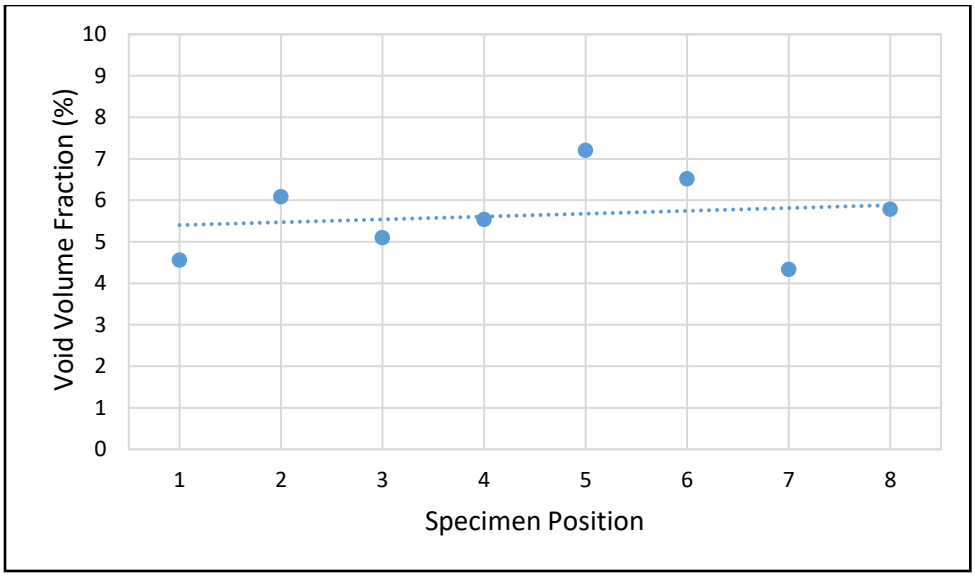

Figure 34: Void volume fraction vs. height of 0.5 mm layer height section 5 stiffener rib specimens.

The constituent volume fraction results do not indicate the presence of any significant trends in the fiber volume fraction or void volume fraction through the height of the stiffener beams. The fiber volume fraction graph trendlines are relatively horizontal in both the 0.4 mm layer height sample data and the 0.5 mm layer height sample data, suggesting that there was little change in the fiber volume fraction of the composite through the height of the stiffener beam. The void volume fraction graph trendline of the 0.4 mm layer height stiffener rib sample appears less horizontal and shows a decreasing slope, especially due to the specimens towards the top of the beam. This suggests that the void volume fraction slightly decreased through the height of the 0.4 mm layer height stiffener rib sample, further suggesting that the composite quality slightly improved through the height of the tall stiffener beam. The void volume fraction graph trendline of the 0.5 mm layer height stiffener rib sample appears much more horizontal. This suggests that the void volume fraction remained relatively consistent through the height of the 0.5 mm layer

height stiffener rib sample. These results show that the quality of the printed composite remained consistent or slightly improved through the height of the stiffener rib samples. Similar trends observed in section 5 of the two stiffener rib samples were also observed in the other 4 sections of the stiffener rib samples.

3.2 Stiffener Rib Microscopic Inspection

Micrograph specimens taken from the loop print samples were inspected using a microscope set to 5x magnification. Images were taken of the samples using a Nikon D5300 DLSR camera fitted with a 2x magnification eyepiece adapter. Due to the size of the polished specimen, multiple pictures were captured to cover the entire width and height. Images were then spliced together to show the full sample.

Figure 35a and 35b show the micrograph images of the two specimens taken from the 0.4 mm layer height stiffener rib sample. Figure 35a shows the “S” specimen or the specimen taken from the start of the stiffener beam, and figure 35b shows the “E” specimen or the specimen taken from the end of the stiffener beam. Both images contain the full height of the specimens and include nominally 80 E-glass/PET layers. It can be seen in the image that the layer boundaries are not easily distinguishable in either specimen. Magnified portions of the specimens are shown in figure 35c and 35d to better show the layer boundaries of the specimens. While linear patterns in the reinforcement can be discerned, which indicate the boundaries between print layers, clear matrix-rich bands at the layer boundaries are not present. This suggests that the reinforcement is well distributed throughout the height of the composite stiffener ribs during manufacturing. It can also be seen that in both specimens the layers at the bottom of the specimens appear thinner and wider. This could suggest that the consolidation force experienced during printing was greater in the initial layers than those towards the top. This

could also be due to the lower print layers proximity to the heated bed. The residual heat from the bed could help keep the viscosity of the thermoplastic lower for longer, giving the material more time to spread and compact.

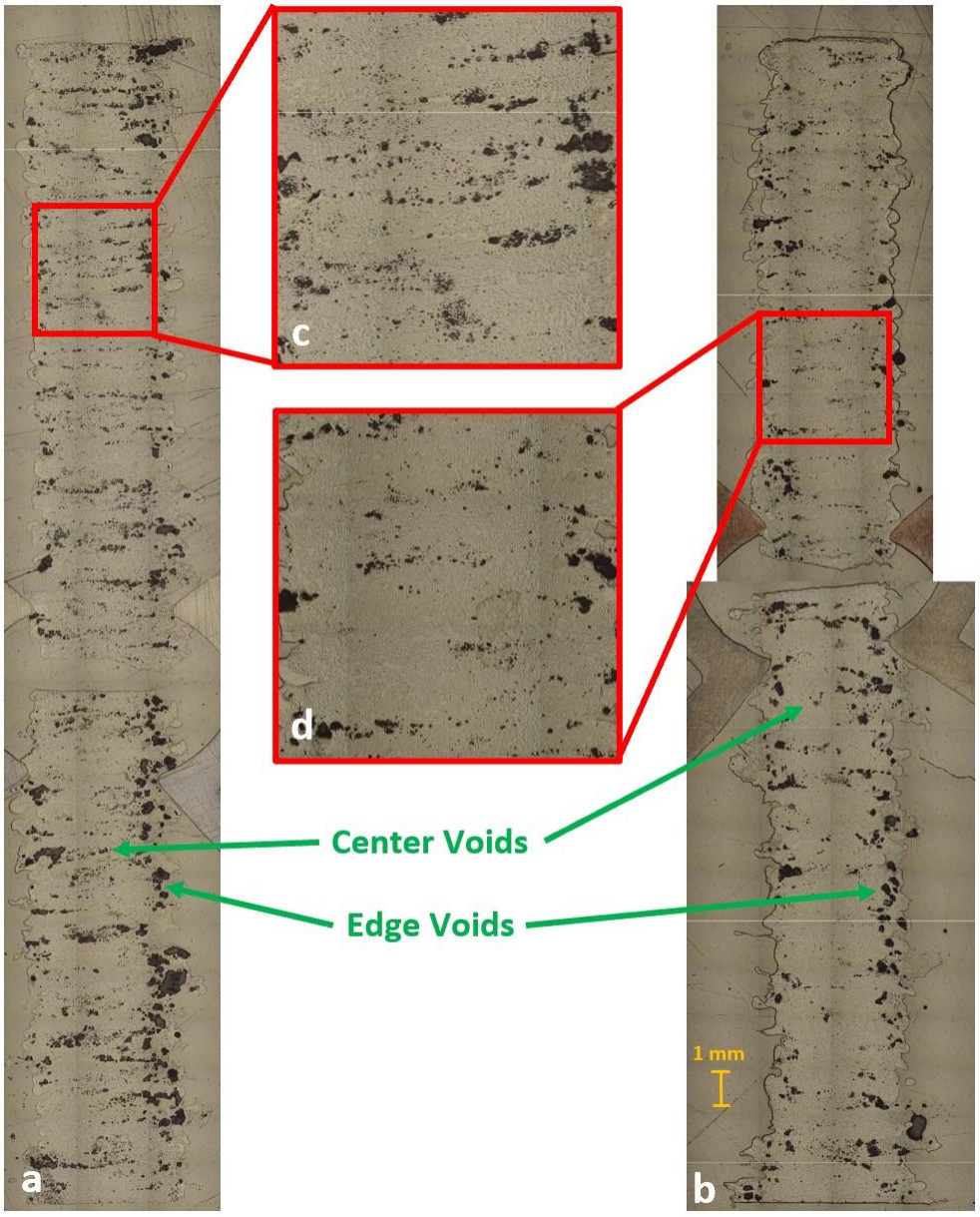

Figure 35: (a) Micrograph of 0.4 mm layer height S specimen. (b) Micrograph of 0.4 mm layer height E specimen. (c) Zoomed in portion of S specimen micrograph. (d) Zoomed in portion of E specimen micrograph.

When looking at the voids in both specimens, which are shown as dark spots in the images, it can be seen that the vast majority of the voids occur on the sides of the specimens. It can also be seen that the voids located on the edges of the specimens appear to be much larger in size than those located in the center of the specimens. This suggests that the quality of the composite material located on the edges of the stiffener beam samples is much poorer than the material located towards the center of the stiffener beam samples. When looking at the voids located towards the center of the two specimens, the image clearly shows that the concentration of center voids is higher in the "S" specimen than in the "E" specimen. This suggests that the quality of the composite material at the start of the stiffener beam sample was lower than the quality of the composite material towards the end of the stiffener beam. This is also supported by the results of the constituent volume fraction analysis, which found that the void volume fraction of the stiffener beam samples decreased through the length of the beam. When looking at the voids in the center of each specimen, the images show that the void concentration appears to slightly increase through the height of the specimens. This is more clear in the "E" specimen, which shows a lower concentration of center voids in the bottom section of the specimen than in the top section. This suggests that the quality of the composite gradually decreased through the height of the stiffener beam samples. This further suggests that the consolidation force experienced during printing gradually decreased between each print layer. It is unlikely that this gradual increase in void concentration through the height of the specimen could be caused by proximity to the heated bed, as it extends through the entire height of the tall, narrow stiffener rib sample which were nominally 30 mm tall.

Figure 36a and 36b show the micrograph images of the two specimens taken from the 0.5 mm layer height stiffener rib sample. Figure 36a shows the "S" specimen taken from the start of

the stiffener beam and figure 36b shows the “E” specimen taken from the end of the stiffener beam. Both images contain the full height of the specimens. Like with the micrographs of the 0.4 mm layer height stiffener rib specimens, it can be seen that the layer boundaries are not easily distinguishable. Magnified portions of the specimens are shown in figure 36c and 36d to better show the layer boundaries. As with the previously discussed micrograph specimens from the 0.4 mm layer height sample clear matrix-rich bands at the layer boundaries are not present, suggesting that the reinforcement was well distributed in the composite during printing.

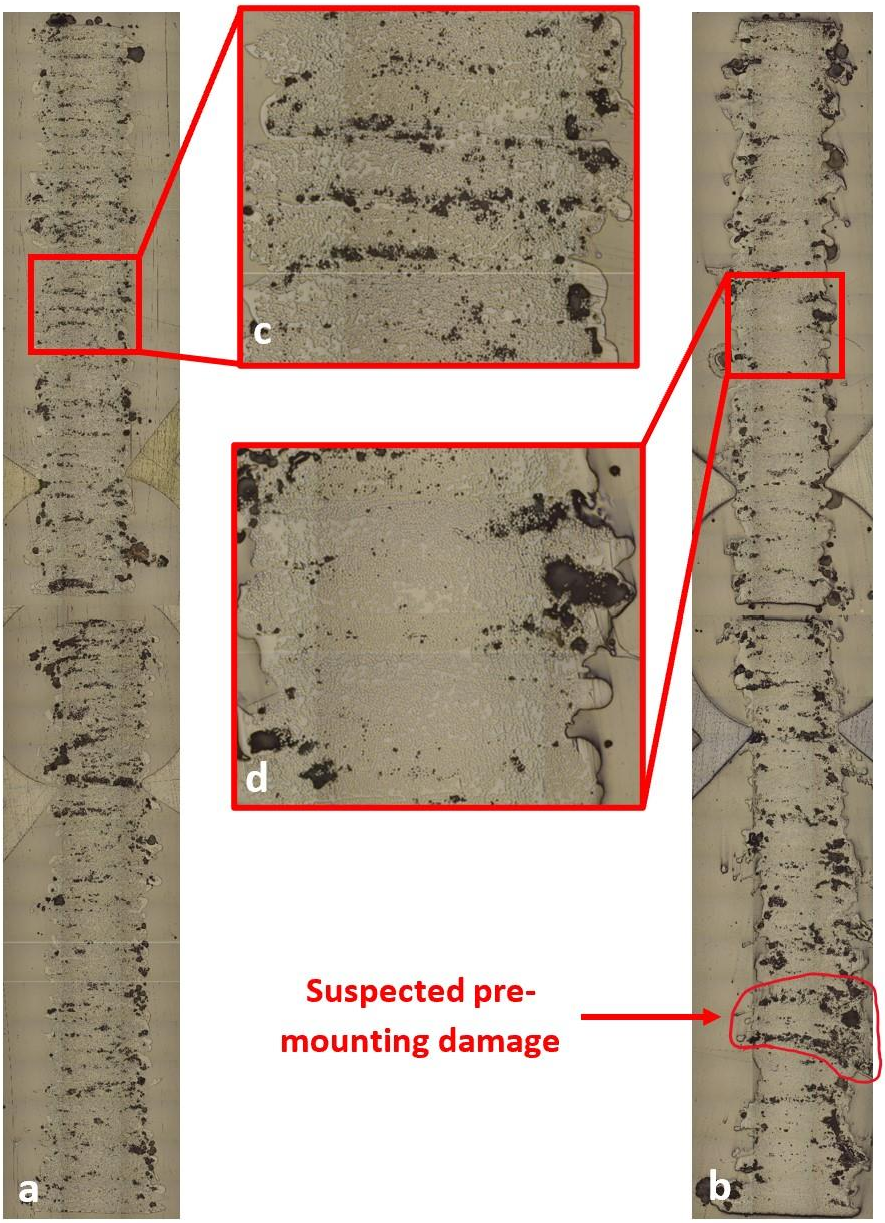

Figure 36: (a) Micrograph of 0.5 mm layer height S specimen. (b) Micrograph of 0.5 mm layer height E specimen. (c) Zoomed in portion of S specimen micrograph. (d) Zoomed in portion of E specimen micrograph.

When looking at the voids in both specimens, similar trends to those seen in the 0.4 mm layer height stiffener rib specimens can be seen. The vast majority of the voids in both of the 0.5 mm layer height stiffener beam specimens occur on the edges of the specimens. The voids on the

edges are also much larger than voids located more towards the center of the specimens. When looking at the center voids, the concentration in the “S” specimen is much higher than the concentration in the “E” specimen, suggesting that the quality of the composite material at the start of the stiffener beam was lower than at the end of the stiffener beam. This is supported by the 0.5 mm layer height stiffener beam constituent volume fraction analysis results, which found that the void content decreased through the length of the beam. However, in the “E” specimen shown in figure 36b, a large cluster of voids can be seen towards the bottom of the specimen, appearing as dark bands across the entire width of the specimen. It is believed that this was caused by minor damage inflicted on the specimen prior to mounting and does not represent the actual center void concentration of the printed material.

Figure 37a and 37b show the micrograph images of both the 0.5 mm layer height stiffener rib specimen and the 0.4 mm layer height stiffener rib specimen. The 0.5 mm layer height specimen is shown in figure 37a, and the 0.4 mm layer height specimen is shown in figure 37b. Both of the micrograph specimens shown are the “E” specimens or the specimens taken from material next to the end of the stiffener beams. Magnified images of sections of the specimens are shown in figure 37c and 37d. Comparing the magnified images of the two specimens shows that the 0.5 mm layer height specimen contains more resin rich areas in the specimen than the 0.4 mm layer height specimen. This suggests that the reinforcement fibers were better consolidated in the 0.4 mm layer height specimen than in the 0.5 mm layer height specimen. Additionally, when looking at the two specimens, it can be seen that the 0.5 mm layer height specimen appears thinner and taller than the 0.4 mm layer height specimen. The 0.4 mm layer height specimen was measured to be about 31 mm tall, and the 0.5 mm layer height specimen was measured to be about 38 mm tall. This suggests that the consolidation force experienced during printing of the

0.4 mm layer height stiffener beam sample was higher than the consolidation force experienced during the printing of the 0.5 mm layer height stiffener beam sample. Wider print layers would have larger areas over which the consolidation force was applied, directly affecting the consolidation pressure experienced during printing of these layers. However, further research is required to fully understand the relationship between consolidation force and consolidation pressure with changing tow width.

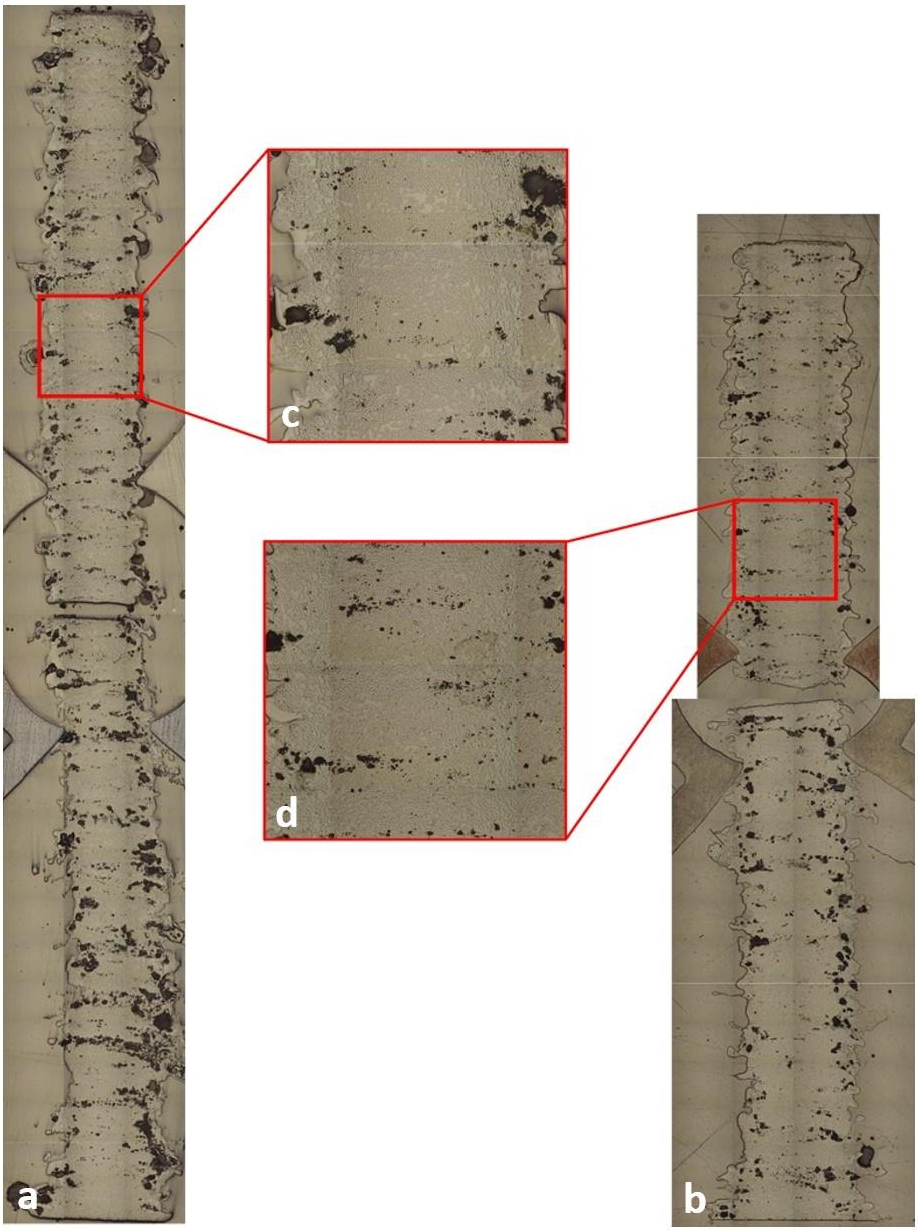

Figure 37: (a) Micrograph of 0.5 mm layer height E specimen. (b) Micrograph of 0.4 mm layer height E specimen. (c) Zoomed in portion of 0.5 mm layer height specimen micrograph. (d) Zoomed in portion of 0.4 mm layer height specimen micrograph.

A further analysis of the micrographs by means of a layer height measurement was attempted for the stiffener rib microscopy samples discussed above and the stiffener grid intersection sample discussed in later sections. Using the image analysis program ImageJ, the

height of the layers of the different micrographs was measured. However, during this process it was realized that due to the inconsistency of the height within each layer, determining an accurate measurement for a layer height would be extremely difficult. In addition, it was found that in many micrograph samples the layer boundaries were unclear or indistinguishable, further complicating the ability to measure layer heights. For these reasons, it was concluded that the largely inaccurate micrograph layer height measurements would not provide meaningful insight into the microstructure of the stiffener rib specimens, and therefore were not included in this report.

3.3 Stiffener Rib Consolidation Force Measurement

The consolidation force was measured during the full manufacturing of a third high aspect ratio stiffener beam sample using the consolidation force measurement system to better understand the force experienced during printing of the high aspect ratio samples. The force measured stiffener beam sample was printed with the same parameters as the previously printed 0.4 mm layer height stiffener beam sample. The stiffener beam sample consolidation force per layer is plotted in figure 38.

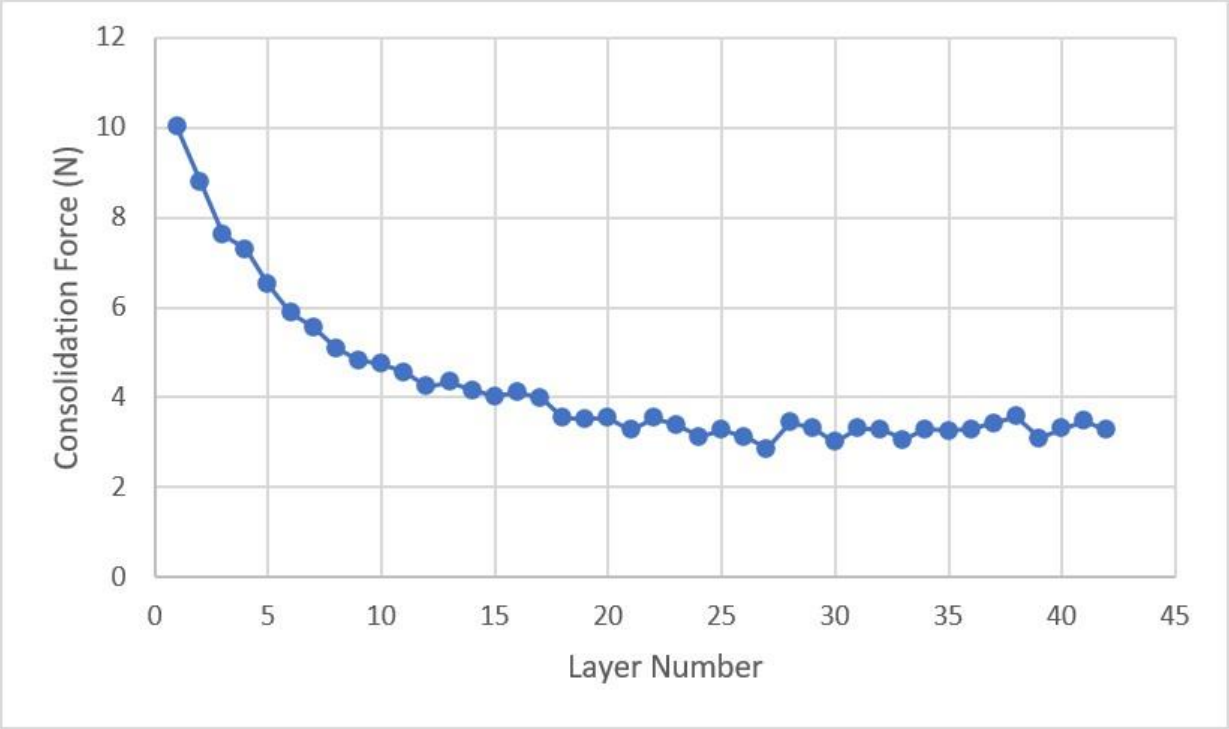

Figure 38: Results of the stiffener beam consolidation force measurement per layer.

The results of the consolidation force measurement test show a significant decrease in consolidation force with the addition of layers to the composite. The graph shows that the consolidation force experienced by the materials, during commingled tow placement, dropped by more than 50% by layer 10. The graph shows that, by layer 25, the consolidation force reached an equilibrium of approximately 30% of the original value. The consolidation force measurement test was configured to continue recording over all 80 layers of the stiffener beam print; however, a data recording error caused a loss of data after layer 43. Independent of the lack of the layer ply data, it is clearly shown that a drop in consolidation force occurs as layers are added until a force equilibrium is reached after approximately the first 20 – 25 layers.

3.4 Force Measured Stiffener Rib Volume Fraction Measurement

The fiber volume fraction and void volume fraction of section 1 and 5 of the stiffener beam sample were found by summing the average fiber volume fraction and void volume fraction of the 4 specimens taken through the height of each section. The fiber volume fraction of both sections of the consolidation force measured stiffener beam sample are shown in figure 39. The void volume fraction of both sections of the stiffener beam sample are shown in figure 40.

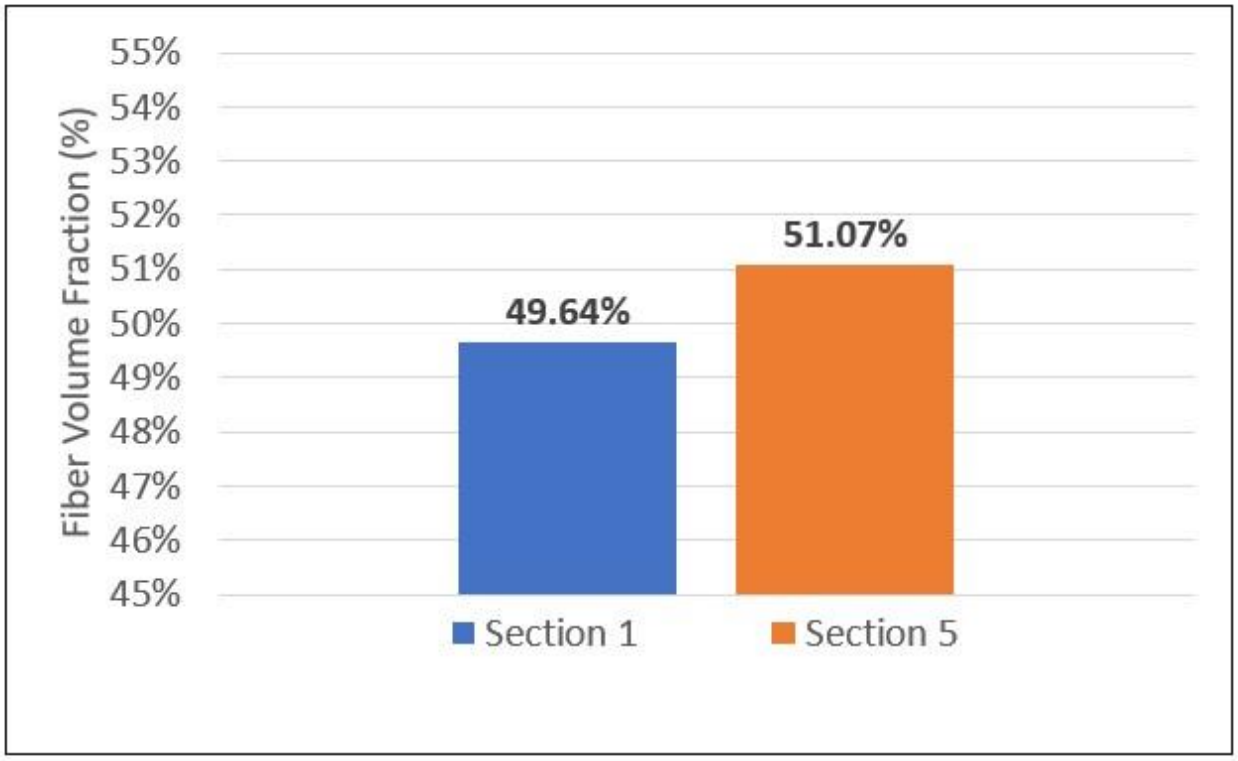

Figure 39: Average fiber volume fraction of sections of force measured stiffener rib sample.

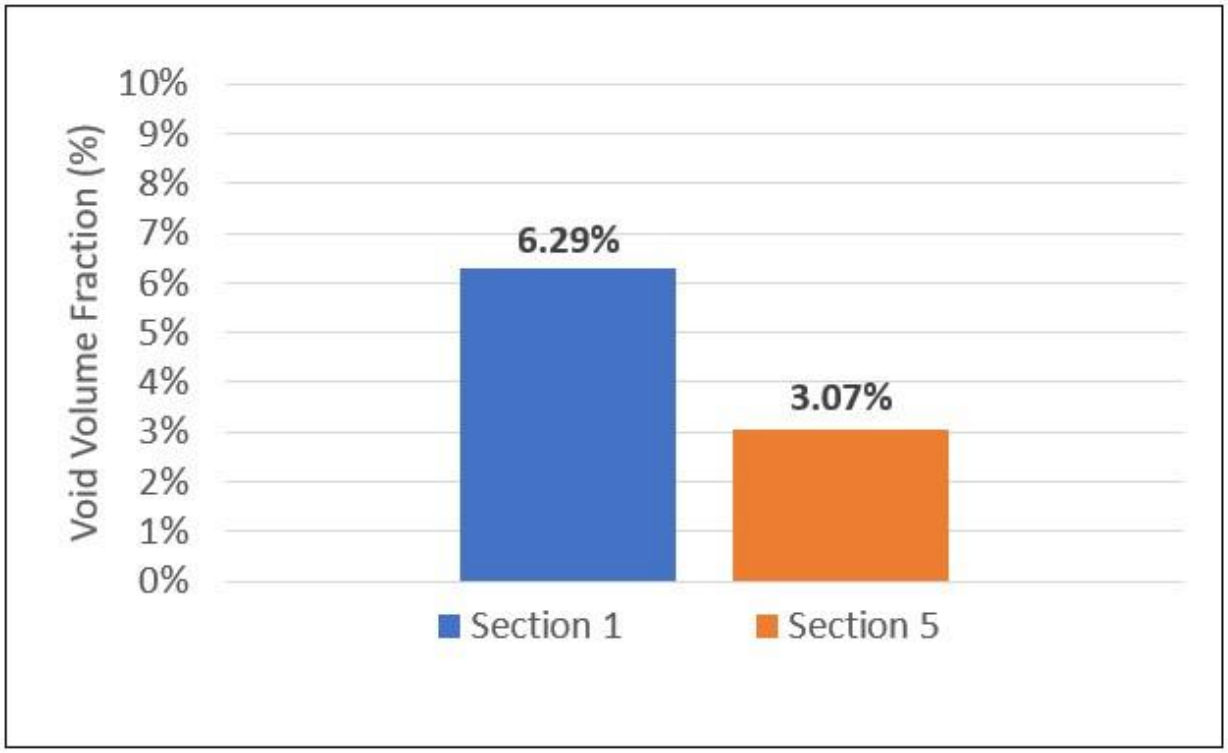

Figure 40: Average void volume fraction of sections of force measured stiffener rib sample.

The fiber volume fraction results indicate that the fiber volume fraction of section 1 at the start of the stiffener beam was slightly lower than the fiber volume fraction of section 5 at the end of the beam. This same trend was also observed in the section constituent volume fraction results of the original 0.4 mm layer height stiffener beam sample. However, the increase in section average fiber volume fraction of the consolidation force measured stiffener beam sample data shown here is greater than the increase seen in the data from the original 0.4 mm layer height sample discussed in section 3.1.5.1 of this publication.

The void volume fraction results indicate that void volume fraction of section 1 at the start of the stiffener beam was significantly higher than the void volume fraction of section 5 at the end of the beam. This same trend was observed in the results of the previous constituent

volume fraction analysis for both the 0.4 mm layer height and 0.5 mm layer height stiffener beam samples. However, the results of the force measured stiffener beam sample show that the void volume fraction of both section 1 and section 5, which were measured to be 6.29% and 3.07%, were lower than the void volume fraction of section 1 and section 5 of the previously tested 0.4 mm layer height stiffener beam sample, which were measured to be 7.12% and 4.39%. The results suggest that the overall void content of the force measured stiffener beam sample was lower than the overall void content of the original 0.4 mm layer height stiffener beam sample. Although the two samples were printed with the same process parameters, the results suggest that the quality of the force measured sample was higher than the quality of the original 0.4 mm layer height sample.

A total of 8 specimens were tested from the stiffener rib sample to examine the relationship between height and the constituent volume fractions of the stiffener ribs. Section 1 and 5 of the stiffener beam sample were each divided into 4 specimens through the height of the sections. The fiber volume fractions and void volume fractions of the specimens were tested and calculated. The fiber volume fractions and void volume fractions of specimens from section 1 of the stiffener beam are plotted in figure 41 and 42. The fiber volume fractions and void volume fractions of the specimens from section 5 of the stiffener beam are plotted in figure 43 and 44.

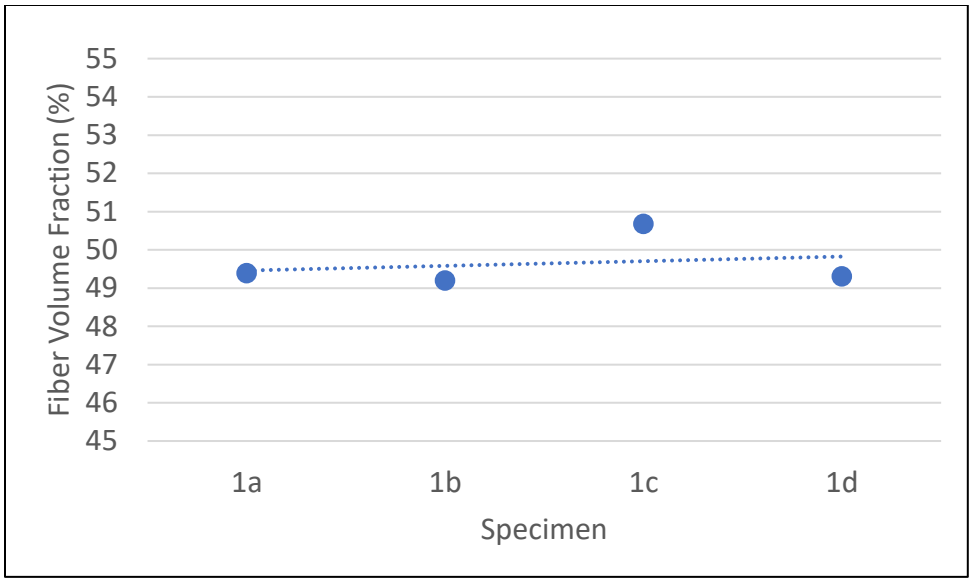

Figure 41: Fiber volume fraction vs. height of section 1 of force measured stiffener rib sample.

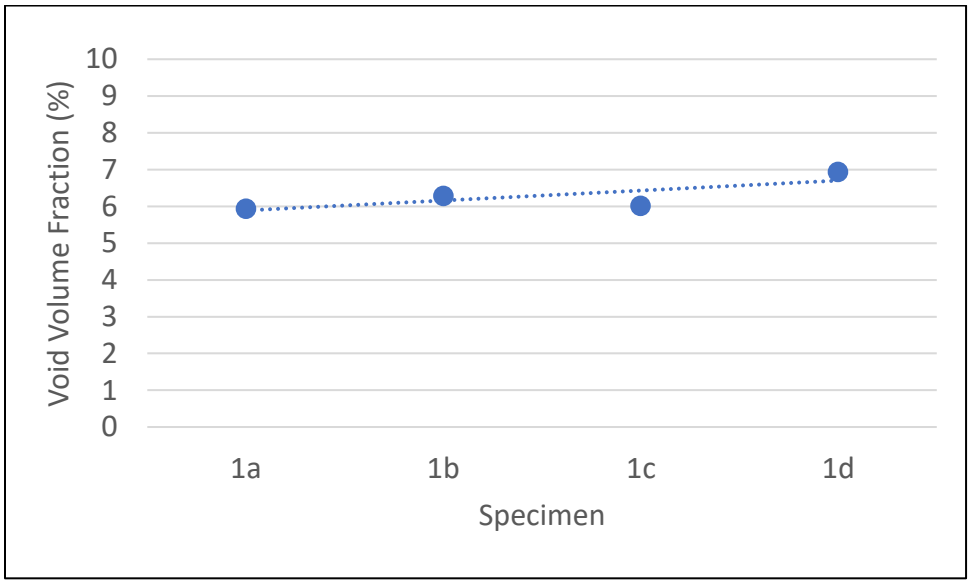

Figure 42: Void volume fraction vs. height of section 1 of force measured stiffener rib sample.

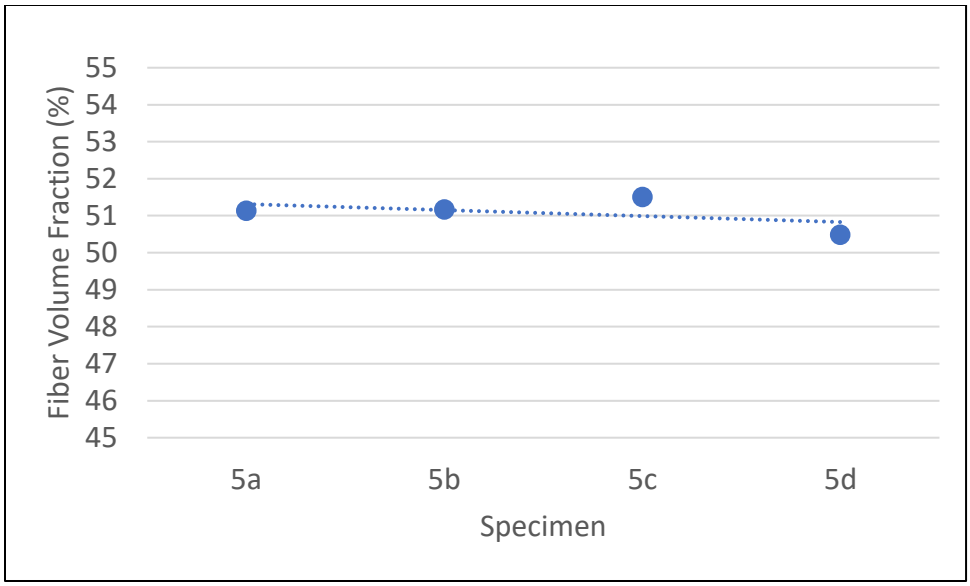

Figure 43: Fiber volume fraction vs. height of section 5 of force measured stiffener rib sample.

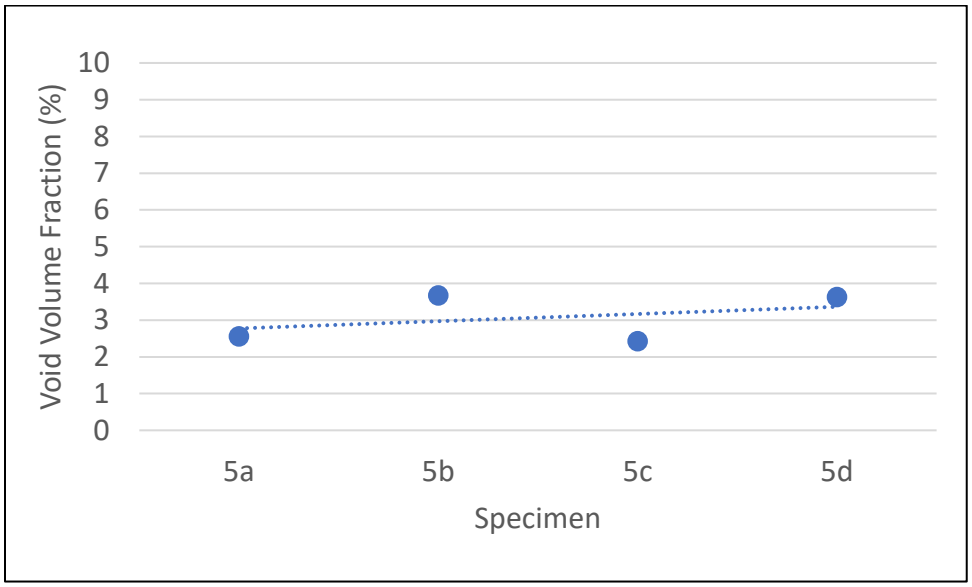

Figure 44: Void volume fraction vs. height of section 5 of force measured stiffener rib sample.

The constituent volume fraction results do not show any significant trends in the fiber volume fraction or the void volume fraction through the height of the stiffener beams. When

looking at the fiber volume fraction of the section 1 and section 5 specimens, shown in figure 41 and 43, it can be seen that the graph trendlines remain relatively horizontal and relatively little variation occurs between the specimens through the height of the sections. The results suggest that there was little change in the fiber volume fraction of the composite through the height of the stiffener beam. When looking at the void volume fraction of the section 1 and section 5 specimens, shown in figure 42 and 44, it can be seen that those graph trendlines also remain relatively horizontal, suggesting that there was also little change in the void volume fraction of the composite through the height of the stiffener beam. However, it can also be seen that a slight positive slope exists in both of the void volume fraction graphs. This suggests that the void content slightly increased through the height of the stiffener beam sample. While minor, the increase seen in the void volume fraction through the height of the stiffener beam contradicts the results of the previous constituent volume fraction test results, which showed that the void volume fraction of the 0.4 mm layer height stiffener beam slightly decreased through the height of the sample. The results of the constituent volume fraction analysis of the consolidation force measured stiffener beam sample suggest that the quality of the stiffener beam composite material slightly decreased through its height.

3.5 Force Measured Stiffener Rib Microscopic Inspection

Figure 45a and 45b show the micrograph images of the two specimens taken from the consolidation force measured stiffener beam loop print sample. Figure 45a shows the “S” specimen taken from material adjacent to the start of the stiffener beam and figure 45b shows the “E” specimen taken from material adjacent to the end of the stiffener beam. Both images contain the full height of the specimens and include nominally 80 print layers. Like with the micrographs of the original stiffener beam specimens, it can be seen that the layer boundaries are not easily

distinguishable. Magnified portions of the specimens are shown in figure 45c and 45d to better show the layer boundaries. Clear matrix-rich bands at the layer boundaries are not present, suggesting that the reinforcement was well distributed in the consolidation force measured stiffener beam sample during printing.

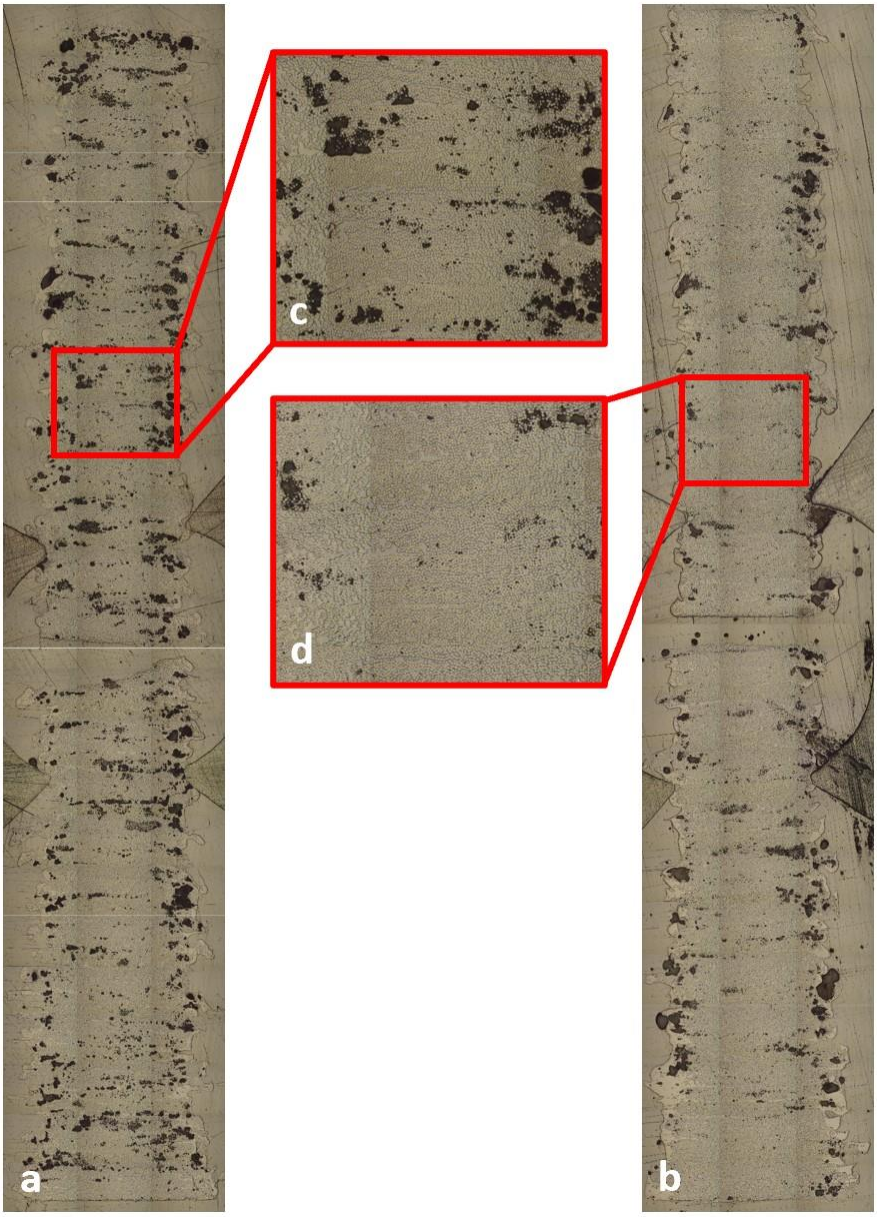

Figure 45: (a) Micrograph of force measured S specimen. (b) Micrograph of force measured E specimen. (c) Zoomed in portion of S specimen micrograph. (d) Zoomed in portion of E specimen micrograph.

When looking at the voids in both specimens, it can be seen that, like with the previously analyzed microscopy specimens, the vast majority of the voids occur on the sides of the specimens. This suggests that the quality of the composite material in the center of the stiffener beam sample higher than the quality of the composite material at the edges of the stiffener beam sample. When looking at the center voids in the two specimens, the image clearly shows that the concentration of center voids is higher in the "S" specimen than in the "E" specimen. This suggest that the quality of the composite material at the start of the stiffener beam sample was lower than the quality of the composite material at the end of the stiffener beam. Additionally, it can be seen in both specimens that the concentration of edge voids and center voids remains relatively consistent through the height of the specimens. This suggests that the quality of the composite material remained consistently high through all layers of the printing process.

3.6 Stiffener Grid Intersection Geometry Measurement

The results of the stiffener grid intersection point sample height and width measurement test are shown in table 2. To measure the tow width at the intersection node, the width just before and just after the intersection were measured for both stiffener rib directions. Then the average of the 4 measurements was used.

Table 2: Results of the stiffener grid intersection point sample geometry measurement test.

40 Layer Crossover Point Print Measurements			
Position	**Height**	**Bottom Width**	**Top Width**
	mm	*mm*	*mm*
A1	14.196	6.55	3.76
A2	14.267	6.92	3.90
B1	14.204	6.70	3.90
B2	14.212	6.65	3.99
C	13.211	6.88*	5.40*
D1	14.167	5.94	3.71
D2	14.236	6.75	4.24
E1	14.178	6.00	3.88
E2	14.223	6.38	3.47

The results of the height measurements indicate that the height of the intersection point sample at the intersection node was about 1 mm shorter than the height of the rest of the sample. This suggests that the tow spreading procedure overcompensated for the intersection node by spreading and compacting the material at the intersection node more than necessary to achieve a uniform sample height. This further suggests that decreasing the magnitude of the increase in consolidation force experienced at the intersection node could result in a sample height at the intersection node equal to the height of the rest of the sample.

The results of the width measurements indicate that the width at the bottom of the intersection point sample was greater than the width at the top of the sample at all locations on the sample. This supports the results of the microscopic inspections performed on the high aspect ratio stiffener beam samples as described in the previous section. In all high aspect ratio samples subject to microscopic inspection, the bottom layers of the samples were thinner and wider than the rest of the sample layers. The results of the width measurements also indicate that the width

of the tows at the intersection node were wider than at the rest of the measurement locations on the sample, suggesting that the tow spreading procedure was effective at spreading the commingled tow when printing the intersection node.

3.7 Stiffener Grid Intersection Consolidation Force Measurement

The consolidation force data over time is shown in figure 46 and figure 47 for the first layer of the two stiffener rib directions. Figure 46 shows the consolidation force data for the first print layer of the first stiffener rib direction, which was fully in contact with the print bed during printing. Figure 47 shows the consolidation force for the first print layer of the second stiffener rib direction, which had to overlap the first stiffener rib direction at the intersection node.

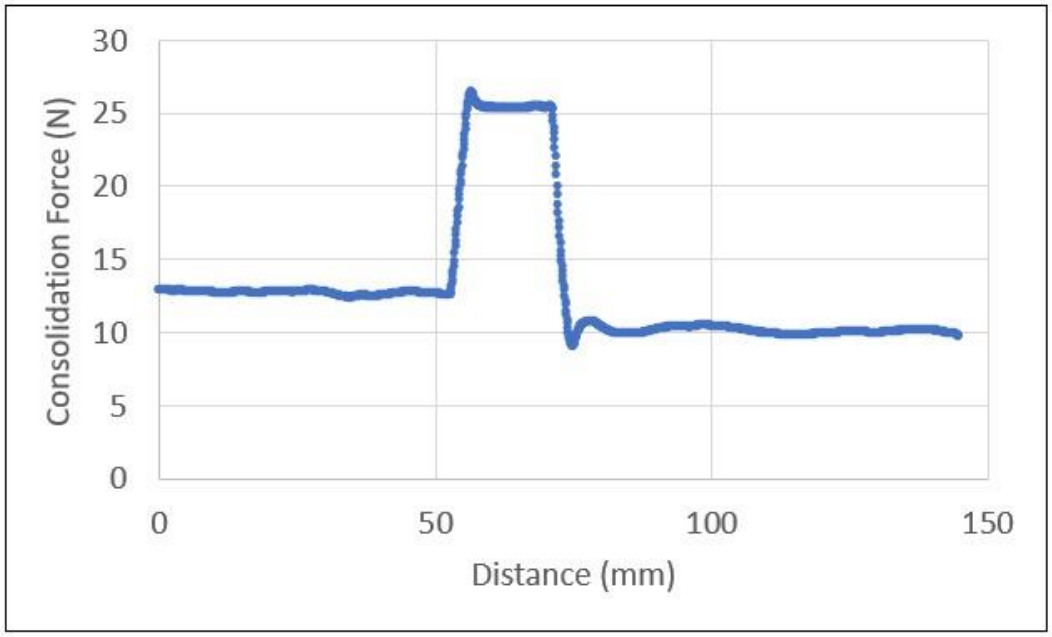

Figure 46: Consolidation force of first layer of the first stiffener rib direction.

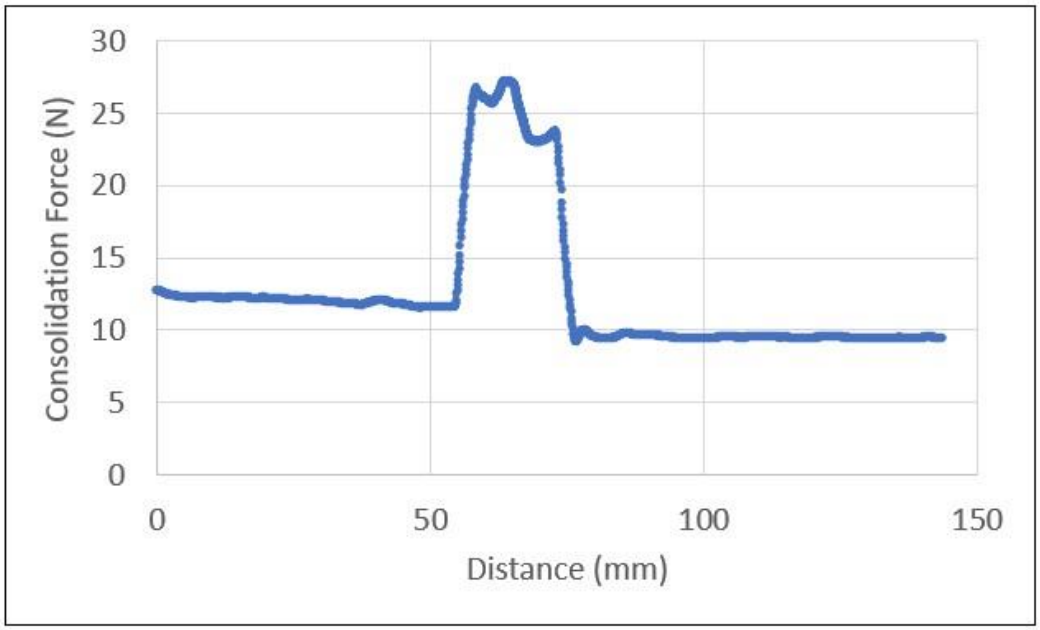

Figure 47: Consolidation force of the first layer of the second stiffener rib direction.

When looking at the two graphs, it can be seen that a large increase in consolidation force exists towards the middle of the graphs. This increase in measured consolidation force corresponds to the location of the intersecting node, where the consolidation force was locally increased and the print speed decreased. When comparing the two graphs, it can be seen that during the increased consolidation portion the graph on the left exhibits a horizontal pattern while the increase consolidation of the graph on the right exhibits a wavy pattern with a raised peak in the center. This raised peak, shown in the first layer of the second stiffener rib direction graph, represents the consolidation force experienced when the placement head was crossing over the first layer of the first stiffener rib direction. It can be seen that the consolidation force experienced at this center peak is higher than the consolidation force experienced during the printing of the first stiffener rib direction intersection node region. For printing of the stiffener grid intersection point sample, the printer was programmed such that for each print layer, the Z-

position of the placement head was the same for both of the stiffener rib directions. The consolidation force experienced during printing of the second stiffener rib intersection node is higher because the placement is programmed to apply the same consolidation pressure as was applied when printing of the first stiffener rib direction intersection node, but now must also overlap the previously printed stiffener rib at the node.

It can also be seen in both graphs that the consolidation force experienced prior to the intersection node is higher than the consolidation force experienced after the intersection node, represented by the horizontal portions before and after the increased central region of the graphs. Although the placement head was programmed to be at the same Z-axis position to apply the same amount of consolidation force before and after the intersection node, the graphs show that the print experienced less force after the node. It is possible that this is related to the increased consolidation force experienced at the intersection node. It is also possible that there was friction in the spring loaded placement head that did not allow the head to fully return to its initial position.

A full analysis of the consolidation force experienced through all of the layers of the intersection point print was desired. However, it was understood that combining the graphs for all of the layers would be much too cluttered to discern any trends from the data. Thus, single data point values were gathered from each data set to represent the forces experienced before, during, and after the intersection node of each layer of the print. Figure 48 shows a graph of one of the data sets and highlights the data points gathered for the analysis.

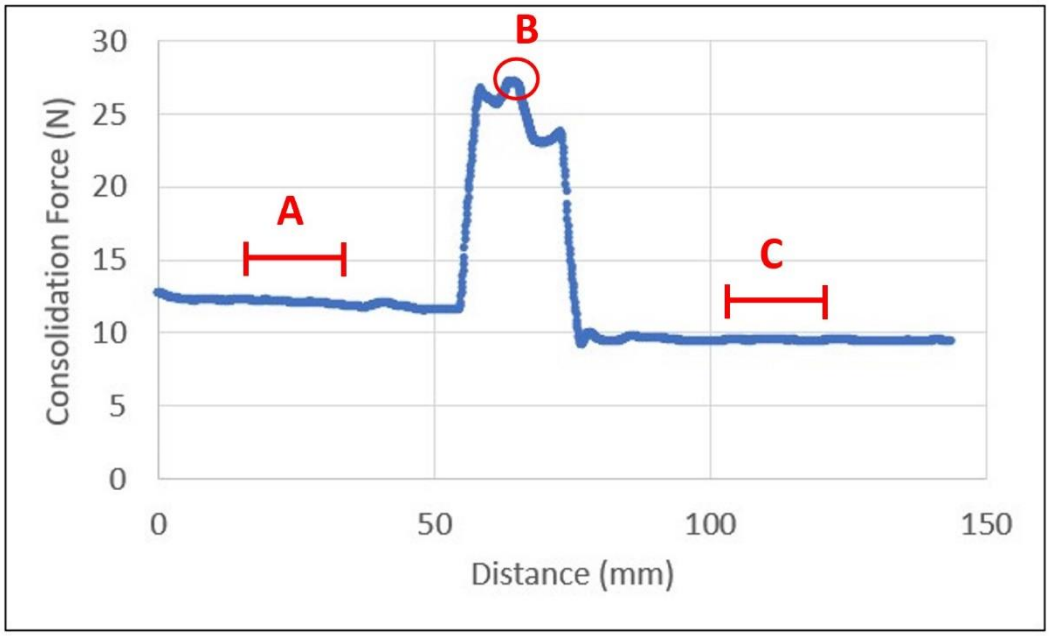

Figure 48: Graph of consolidation force with the points gathered for force analysis of all print layers highlighted.

To represent the consolidation force experienced at the intersection node for each print layers, the maximum value of the peak at B was found for each data set. To represent the consolidation force experienced before and after the intersection node, values A and C were found by taking the average of 300 data points located at the middle of the two horizontal regions. A MATLAB code was written to efficiently find these values for all of the consolidation force data sets gathered during the force measurement test.

Figure 49 shows the consolidation force data for all of the layers of the intersection point print. The graph shows 6 data sets which represent the consolidation force values of before, during, and after the intersection node for both stiffener rib directions. The data sets are labeled with a direction of D1 or D2 followed by a location of Pre, Int, or Post. D1 represent the first stiffener rib direction and D2 represent the second stiffener rib direction. Pre represents the

consolidation force prior to the intersection node, Int represent the consolidation force at the intersection node, and Post represents the consolidation force after the intersection node.

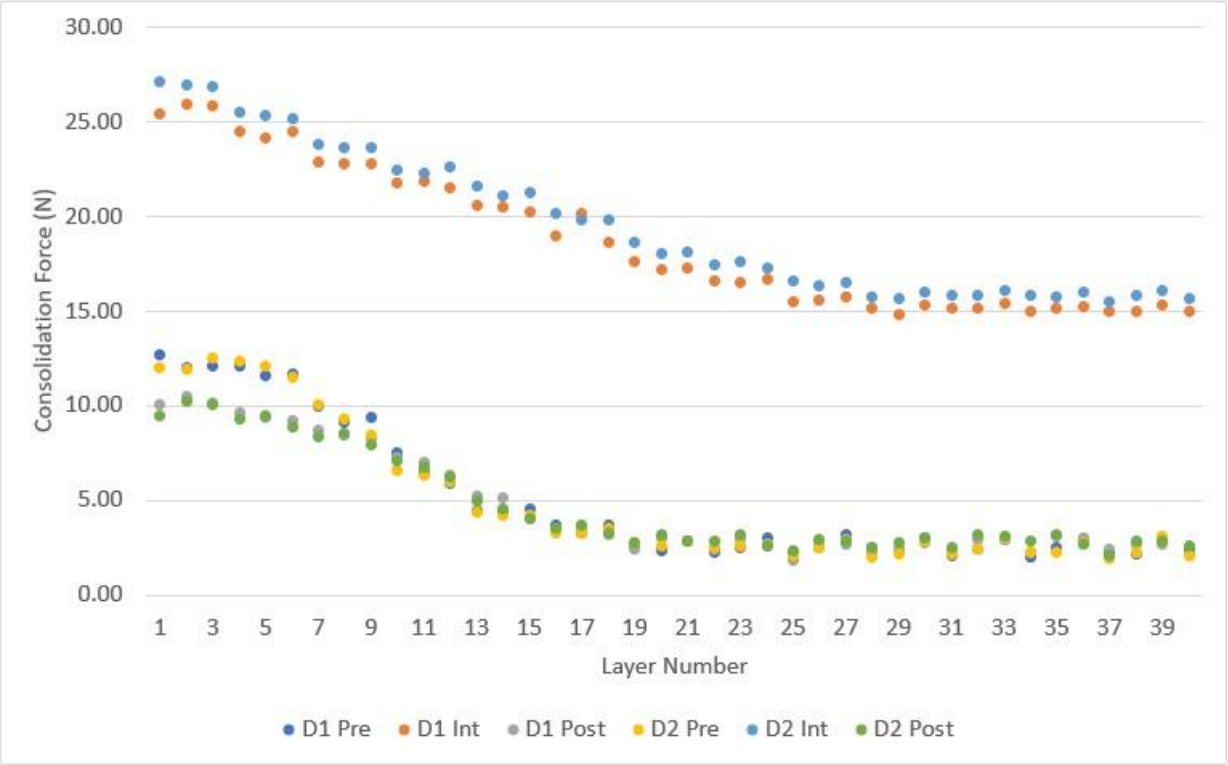

Figure 49: Consolidation force of all layers of the stiffener grid intersection sample.

It can be seen in the graph that all of the data sets show significant decreases in consolidation force with the addition of layers to the composite. This suggests that the consolidation force experienced during printing decreased with increasing layers at all locations of the intersection point print sample. The graph shows that at the intersection node, the consolidation force started at a force of around 26 N at the first layer of the print. The graph shows that the force decreased with the addition of layers to the composite until around layer 30, at which the force reached an equilibrium at around 15 N, which is approximately 58% of the consolidation force experienced at layer 1. However, the graph shows that the regions before and

after the intersection node reached a consolidation force equilibrium earlier than at the intersection node. The graph shows that at the regions before and after the intersection node, the consolidation force decreased with the addition of layers until around layer 20, at which the force reached an equilibrium at around 3 N. This is consistent with the results of the stiffener rib consolidation force measurements discussed in section 3.3.

When looking at the data sets for the intersection node consolidation force, it can be seen that for all but one of the layers the consolidation force experienced at the intersection node in stiffener rib direction 2 was higher than in stiffener rib direction 1. This is due to how the placement head was programmed to print the two stiffener rib directions. As explained above, the printer was programmed such that for each print layer, the Z-axis position of the placement head was the same for both of the stiffener rib directions. The consolidation force experienced during printing of the second stiffener rib intersection node is higher because the placement head is programmed to apply the same consolidation force as was applied when printing of the first stiffener rib direction intersection node, but now must also overlap the previously printed stiffener rib at the node requiring more compression of the spring in the placement head and resulting in a higher consolidation force. This suggests that the layer height of the first stiffener rib direction at the intersection node would be slightly more than the layer height of the second stiffener rib direction at the intersection node, as the second stiffener rib direction layers at the node experienced slightly more consolidation force at the node.

To better analyze the consolidation force experienced during printing of the intersection point sample, several print layer graphs were combined for comparison. Figure 50 shows consolidation force data for the second stiffener rib direction at layers 1, 5, 10, 15, 20, 25, 30, 35, and 40. Although only data from the second stiffener rib direction was used, and only selected

print layers were shown, it should be noted that the trends observed here were observed through all of the print layers for both stiffener rib directions.

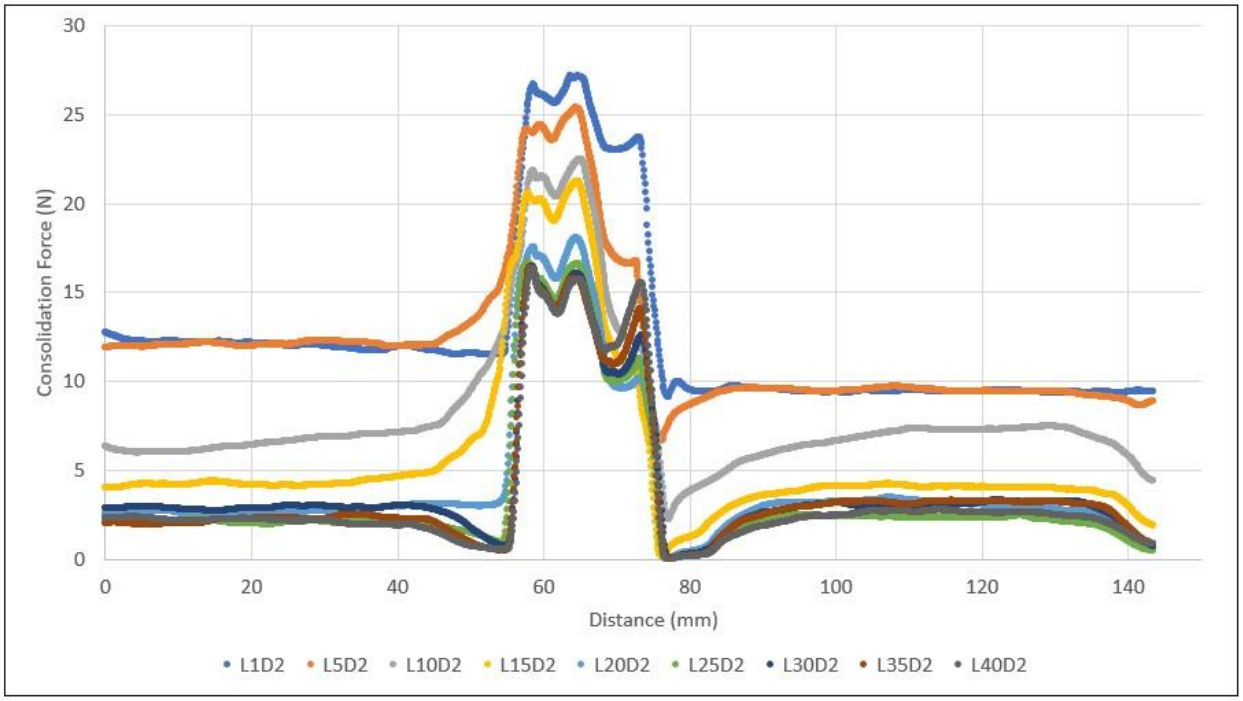

Figure 50: Consolidation force graph of multiple layers of the stiffener grid intersection sample. Graph shows consolidation force data for layers 1, 5, 10, 15, 20, 25, 30, 35, and 40.

It can be seen on the graph that, just as was observed in the previously discussed graph showing the consolidation force for all of the print layers on figure 49, the consolidation force of the regions before and after the intersection node become equal and reach equilibrium around layer 20, while the consolidation force at the intersection node reaches equilibrium around layer 30. When looking at the region of the graph just before the higher consolidation force area, it can be seen that at lower layers, the consolidation force increases before reaching the intersection node, but at higher layers the consolidation force decreases before reaching the intersection node. This suggests that the top surface profile was changing as print layers were added.

When looking at the higher layers of the graph, specifically layers 25, 30, 35, and 40, it can be seen that for the most part the curves stay relatively similar. However, there is a notable exception. It can be seen that on the right side of the increased consolidation force region of the graph there is a peak just before the curves fall almost vertically down to the post intersection node region. When looking at that peak, it can be seen that the height of the peak increases with increasing layer count. This suggests that at higher print layers above layer 20 the consolidation force experienced at the very end of the intersection node region right before the Z-axis position was raised and the consolidation force was greater in higher layers, possibly due to a changing height of the stiffener grid intersection sample.

3.8 Stiffener Grid Intersection Volume Fraction Measurement

The fiber volume fraction and void volume fraction were found for each of the specimens located at the stiffener rib regions as well as the C1V intersection node specimen. Figure 51 shows the fiber volume fractions of the specimens.

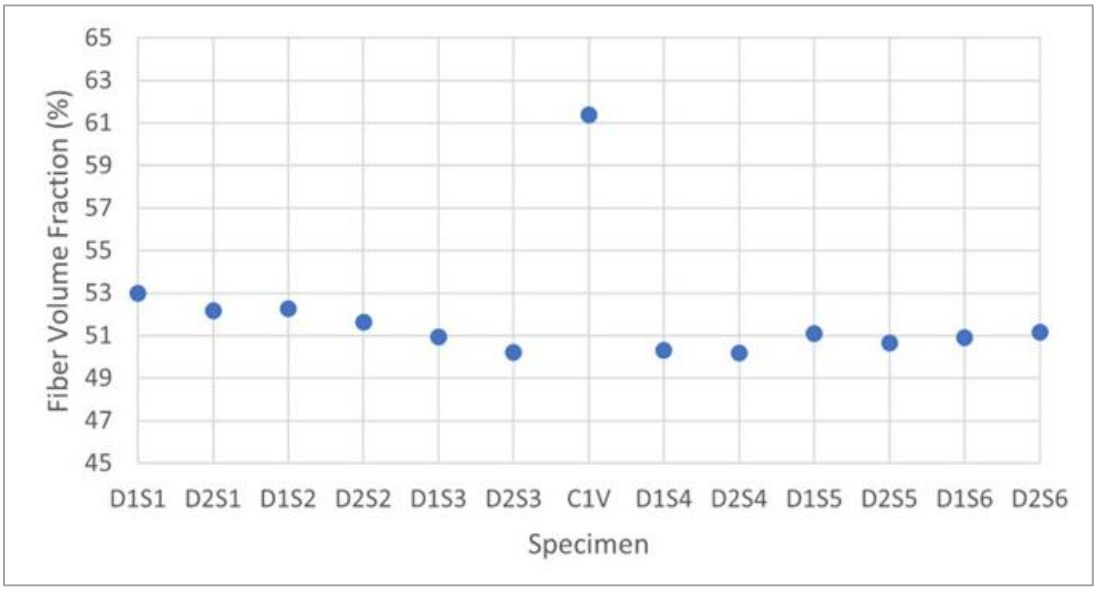

Figure 51: Fiber volume fraction of the stiffener grid intersection specimens.

The fiber volume fraction results indicate that for the specimens located in the stiffener rib region, the fiber volume fraction was relatively the same. However, the fiber volume fraction results show that at the intersection node the fiber volume fraction was significantly higher. The results show that the fiber volume fraction at the intersection node was above 61%. This is especially significant because the unprocessed fiber volume fraction of the commingled tow is only 55%. In order to achieve a processed fiber volume fraction that is higher than the unprocessed fiber volume fraction, some amount of the matrix material must have been removed or moved outside of the area of the intersection node pyrolysis specimen.

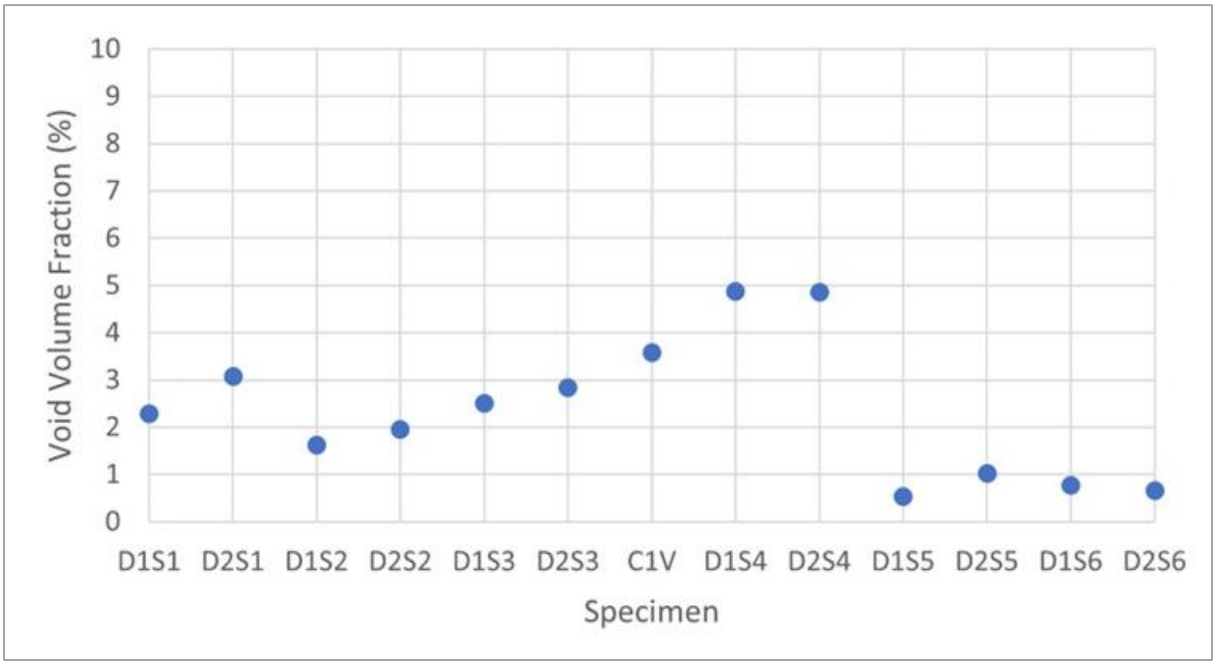

Figure 52: Void volume fraction of the stiffener grid intersection specimens.

Figure 52 shows the void volume fraction of the intersection point sample specimens. The results show that the void content at the intersection node was higher than the void content in the stiffener rib regions before the node. The results show that the void content in the sample

appear to increase through the intersection node, with the highest void content located at the specimens immediately after the node. Instead of a lower void volume fraction at the intersection node, as one might expect due to the higher consolidation force, the results show that the void content increased. It is possible that some aspect of the overlapping print layers is encouraging the formation of voids. It is also possible that the increased consolidation force at the intersection node caused resin to be squeezed out which while doing so captured excess voids.

3.9 Stiffener Grid Intersection Microscopic Inspection

Figure 53 shows the micrograph image of the intersection node specimen. Like with the previous microscopy specimen images, the size of the specimen required multiple pictures to be spliced together to show the full specimen. It can be seen in the image that, like with the high aspect ratio stiffener rib microscopy specimens, the layer boundaries in the intersection node specimen are not easily distinguishable. A magnified portion of a center region of the specimen is shown in figure 54. While layer boundary lines can be seen, clear matrix-rich bands at the layer boundaries are not present, suggesting that the reinforcement was well distributed in the intersection node of the stiffener grid intersection point print sample. In addition, it can be seen that the reinforcement fibers appear not as circles but as ovals. This is due to the orientation of the fibers. The intersection node of the sample was divided along the diagonal of the node, causing the reinforcement fibers to be oriented ± 45° from the cut surface of the specimen. The 45° angle of the fibers causes them to appear as ovals in the microscopy image. Additionally, the angle that the reinforcement fibers were cut was the same for both print directions, causing the fibers in both print directions to appear the same on the micrograph.

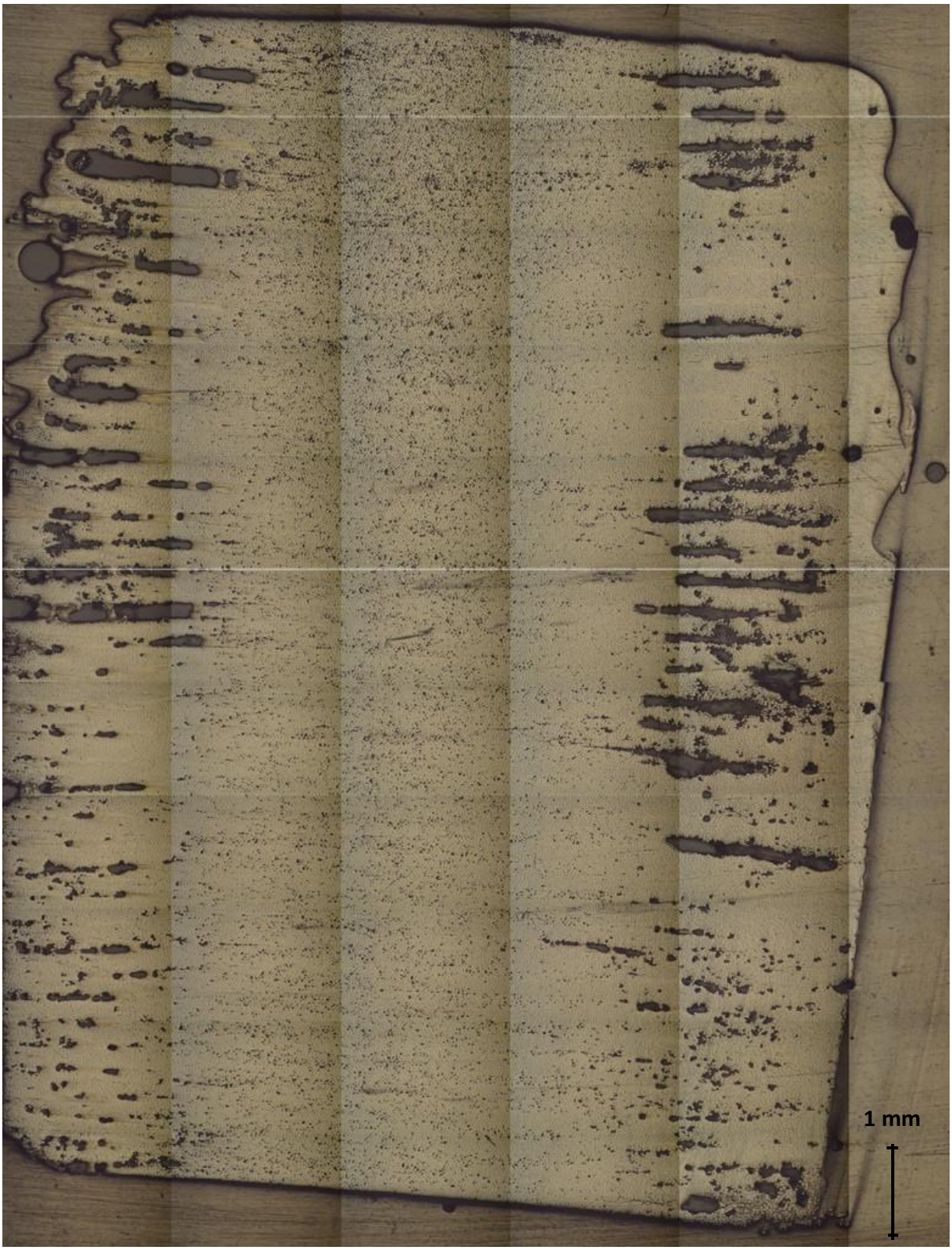

Figure 53: Micrograph of the stiffener grid intersection node specimen after the first polish.

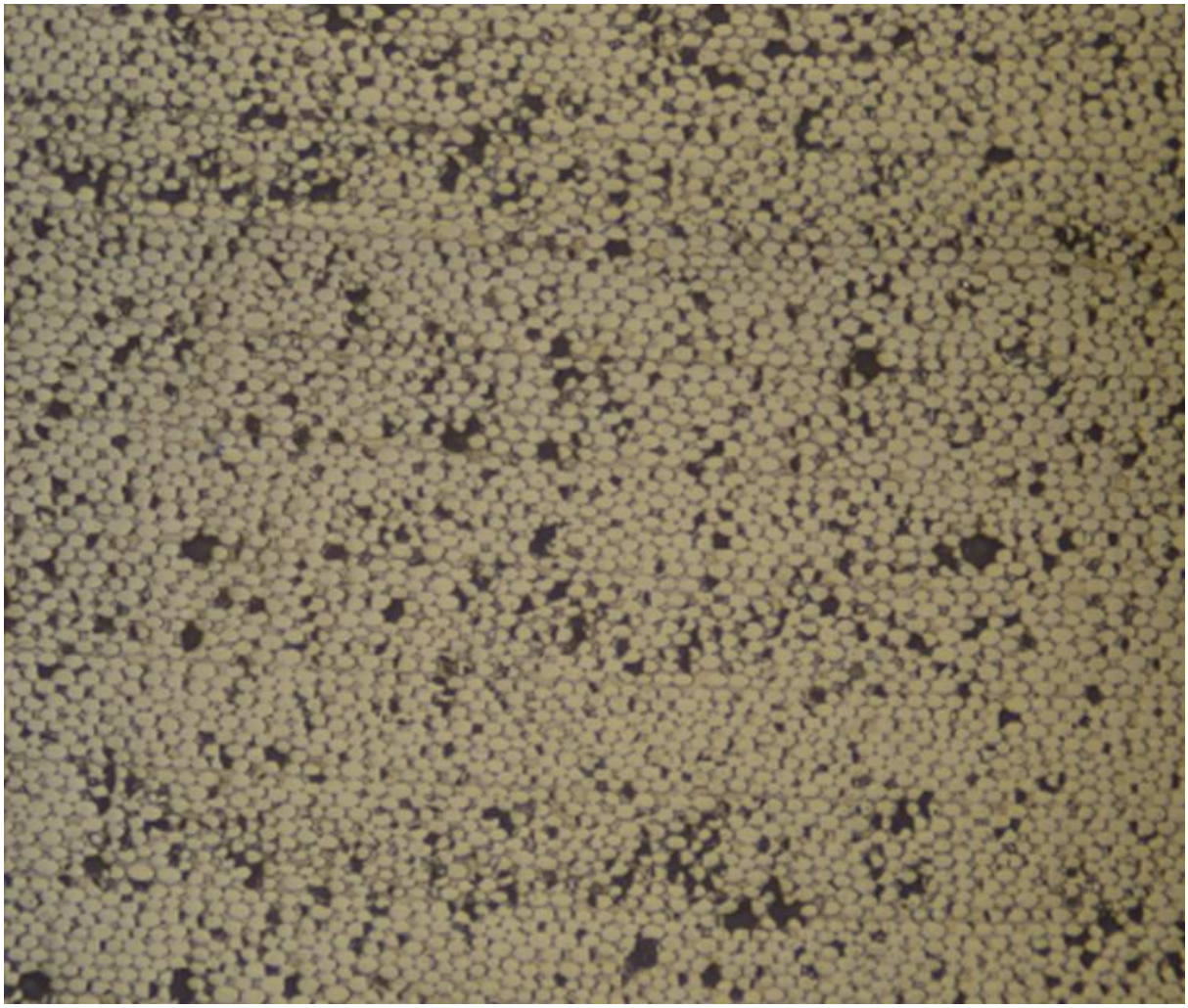

Figure 54: Magnified portion of the intersection node specimen micrograph.

When looking at the voids in the specimen it can be seen that, like with the high aspect ratio stiffener rib microscopy specimens, the vast majority of the voids are located towards the edges of the specimen. It can be seen that the center of the specimen appears to be relatively free of large voids. However, it can be seen that the center of the specimen appears to show a large concentration of black specks and exhibits a “peppered” appearance. Figure 54 shows a magnified portion of the center region of the specimen to better show the dark specks in the center. While it is possible that some of the dark specks could be voids formed between the

reinforcement fibers, it can be seen that many of the dark specks appear to cover up the fibers, suggesting that they instead consist of particles in front of the fibers. Due to this it is believed that the vast majority of the specks are not voids but instead polishing debris, and do not represent the void concentration that existed in the specimen. It should be noted that this specimen was polished using an earlier procedure which tended to leave polishing debris and produce poorer quality microscopy surfaces.

When looking at the edge voids, it can be seen that the voids appear to be quite large compared to those seen in the high aspect ratio stiffener rib microscopy specimens. Furthermore, it can be seen that the voids appear as long, sausage like shapes. Figure 55 shows a magnified portion of the specimens showing the large edge voids. When looking at the magnified image, it can be seen that the voids have formed in matrix-rich bands which appear to exist on the edge of print layers. Furthermore, it can be seen that the reinforcement of every other print layer appears to stop short on the right side of the image. The results suggest that there was an offset between the two stiffener rib directions at the intersection node, and that large voids formed at the edges of the print layers.

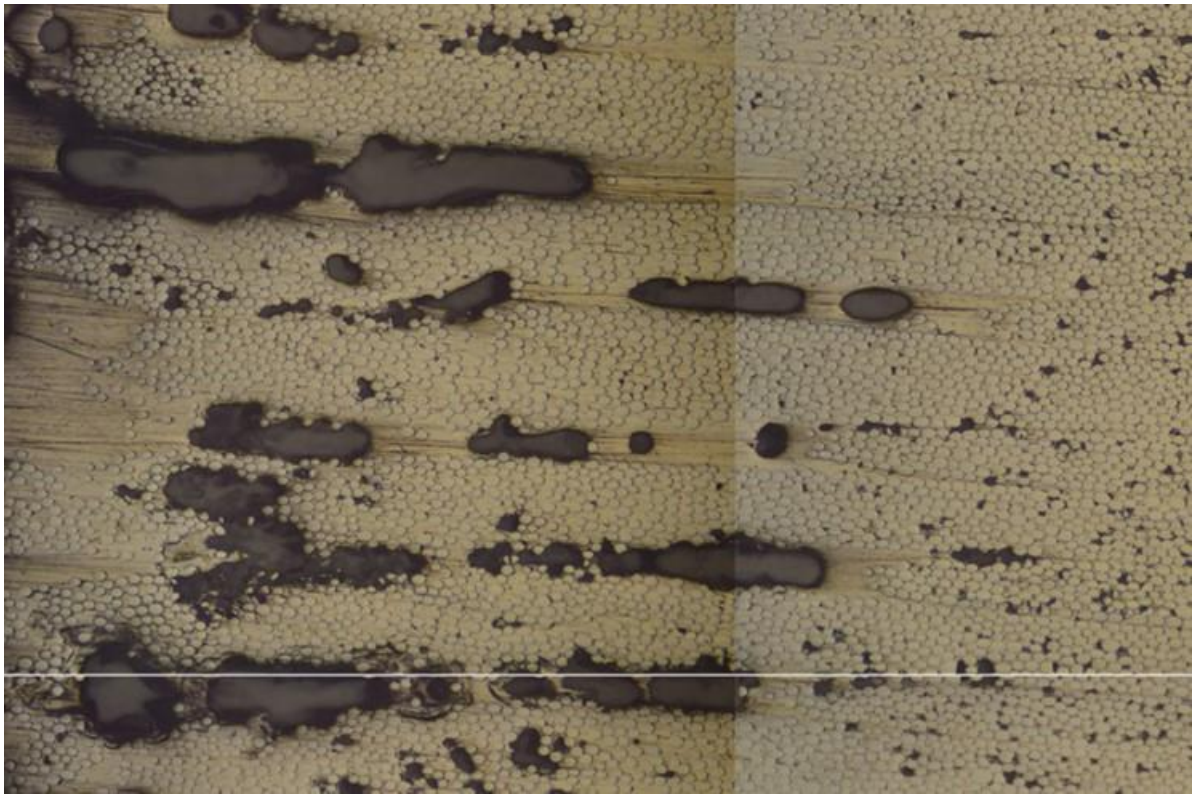

Figure 55: Magnified portion of the intersection node specimen micrograph showing large voids at the edges of the specimen.

A second microscopic inspection was performed on the intersection node specimen to observe how the print layer geometry and void distribution would change with depth into the specimen. The polished microscopy surface of the specimen was sanded approximately 1 – 2 mm back, and then repolished using the more refined polishing process which was used to produce all of the previously discussed high aspect ratio stiffener rib microscopy specimens. In addition, the light source of the microscope used for the inspection was better aligned to minimize the shading on the edge of each of the spliced images. Figure 56 shows the micrograph images of the intersection node sample after it was re-polished.

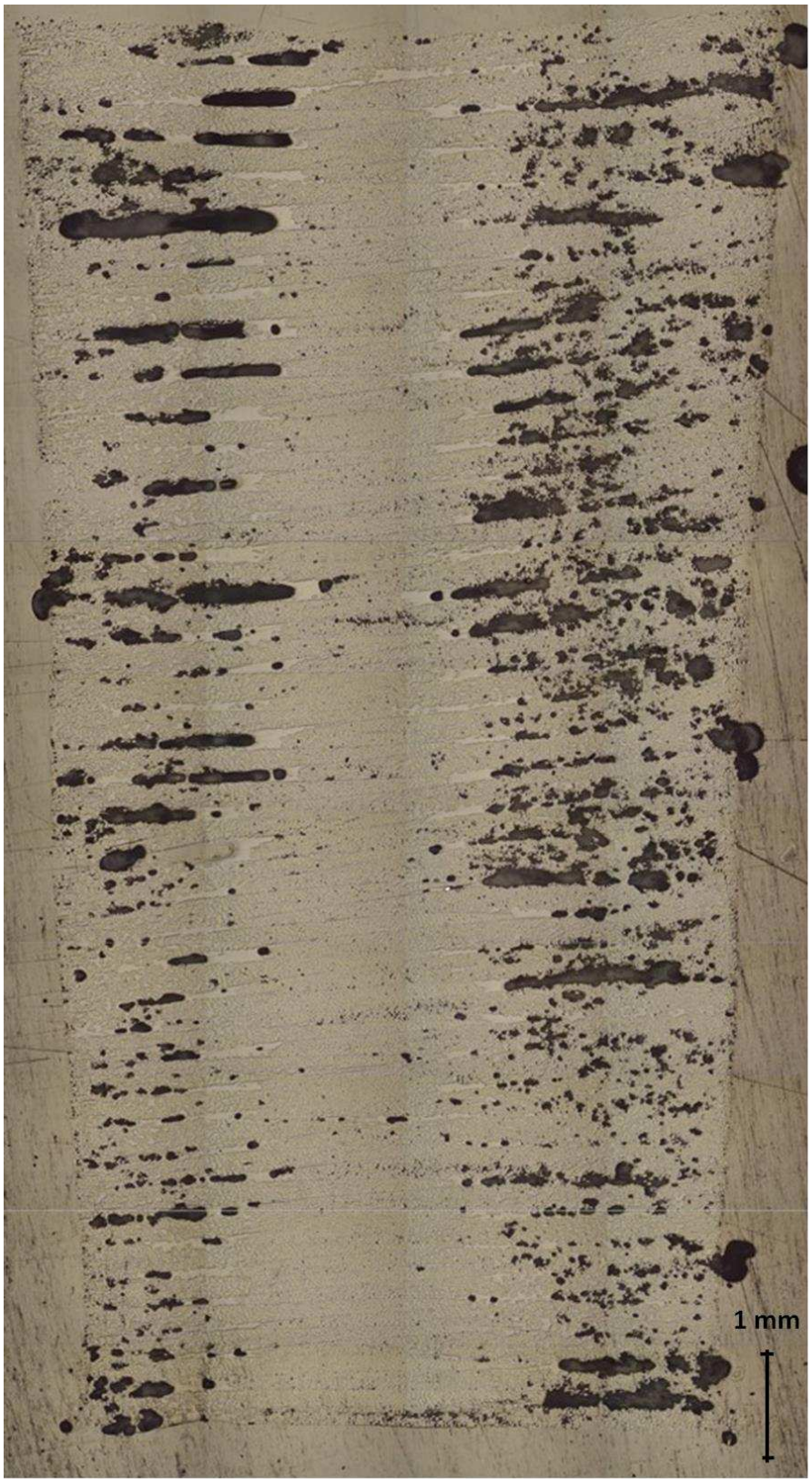

Figure 56: Micrograph of intersection node specimen after second polish.

When looking at the results of the second microscopic inspection, it can be seen that the specimen is significantly thinner than in the first microscopy image. This is due to the sanding back of the specimen for the second microscopic inspection. As discussed earlier, the intersection node of the intersection point print sample was divided in half along the diagonal. Doing so created two triangular prism shaped specimens, with one used for pyrolysis and one used for microscopy. Due to the triangular prism geometry of the microscopic inspection specimen, sanding back the polishing surface caused the overall width of the microscopy specimen to decrease, resulting in a narrower specimen. Additionally, it can also be seen that the specimen appears to be narrower at the bottom than at the top. This is most likely due to a slight angle that was mistakenly created on the polishing surface while sanding it back. A more precise sanding and polishing procedure, especially one which incorporated an automatic mechanism, would be able to better sand and polish the surface of the microscopy sample and ensure that the specimen was kept parallel to the sanding and polishing surface through the entirety of the procedure.

When looking at the voids on the edges of the specimen, it can be seen that the size of the voids appears to be much wider than the voids shown in the first microscopic inspection image. However, the second microscopic inspection specimen is significantly thinner than the first microscopic inspection image. Thus, it can be seen that the voids take up much more of the full width of the specimen, and the region in the center of the specimen containing fewer voids is much more narrow than the center region seen in the first microscopic inspection image. Instead of growing in size, the edge voids stayed relatively the same size as the ones observed in the first microscopic inspection specimen image.

4 Discussion

4.1 Stiffener Rib Volume Fraction Measurement

The results of the constituent volume fraction analysis through the length of the stiffener ribs shown in figures 27-30 in section 3.1 showed a clear decrease in void volume fraction along the length. This trend is likely due to the shallow turns in the loop print sample geometry, as the void content decreased with increasing distance from the turn in the print path (see figure 16). It is possible that tumbling of the fibers occurred while making the turns, which could trap air and induce a larger concentration of voids. It is also possible that the decreasing void content along the length of the stiffener beams is due to the nozzle temperature fluctuations when printing. While printing the turns of the loop print, cooling air was turned on to lower the temperature of the nozzle and help rigidize the material faster, increasing the positional fidelity of the material. When printing the straight sections of the loop print samples, the cooling air was not necessary and so it was turned off to improve consolidation and interlayer fusion. Immediately after a turn, the nozzle would be lower in temperature from the cooling air. While printing the straight sections, the nozzle would likely increase in temperature as it was no longer being cooled. This gradual increase in nozzle temperature while printing the straight sections of the loop prints could affect the resulting void content of the composite material being printed. Studies have shown that higher nozzle temperatures result in fewer voids for neat thermoplastic 3d printing [63, 64, 65, 66]. It is likely that a similar trend would exist for thermoplastic matrix composite printing processes.

The results of the constituent volume fraction analysis through the height of the stiffener ribs shown in figures 31-34 in section 3.1 showed that the void volume fraction remained relatively consistent or even slightly decreased through the height of the stiffener ribs. These

results were somewhat surprising. It was hypothesized that the void content would gradually increase through the height of the stiffener ribs due to the effects of the temperature field generated by the heated bed. Studies have shown that 3D printer heated beds generate significant temperature fields which can impact the properties of printed structures [67]. The residual heat emanating off of the heated print bed directly effects the cooling rate experienced by print layers depending on their proximity to the bed, causing the cooling rate of lower print layers closer to the bed to be slower than the cooling rate of higher layers further away from the print bed. Other studies have shown that the cooling rate effects the void formation in fiber reinforced thermoplastic matrix composite materials [68]. Studies show that slower cooling rates result in lower void contents. However, the results of the constituent volume fraction analysis on the stiffener rib showed no evidence of an increase in void content through the height of the stiffener rib, and even showed a small decrease in void content through the height in the 0.4 mm layer height stiffener rib sample. Further analysis is required to determine the cause of this trend.

4.2 Stiffener Rib Microscopic Inspection

The results of the stiffener rib microscopic analysis shown in figures 35-37 in section 3.2 showed that the vast majority of the voids in the specimens were located at the edges of the specimens. This was possibly due to the how the material was compacted by the placement head during printing. While printing, the placement head was applying a consolidation pressure to the print layer, which was causing the material to compress and squeeze the molten matrix material. Excess matrix material was forced out toward the edges of the print layers, where it collected and formed matrix rich regions as shown in the micrographs. Voids that formed between print layers would also be squeezed and forced towards the edges, where they would collect in these matrix rich regions. In addition, the lack of lateral constrain at the edges of the print layers means that

the edges experience less consolidation pressure than at the center, allowing for more voids to form at the edges. This effect has also been observed in a thermoplastic composite laminate consolidation study, which found that the thickness and number of voids at the edges of the laminate were larger than those at the middle of the laminate [69].

It is also possible that the high concentration of voids at the edges of the specimens is due to lateral shifting of the tow while printing. If the print layers were not placed exactly on top of one another but instead had small overhangs along the sides of the print layers. If this was the case, then the consolidation force experienced at the overhanging regions would be much lower, as there would not be material under it to support it while it was being compressed by the placement head. The rough, uneven edges of the specimens in the micrographs supports this possibility, as there are numerous overhanging regions that can be seen at the edges. While it is possible that lateral shifting of tows could be caused by a malfunction with the composite placement system, it is more likely that the print layer misalignment would be due to precision limitations of the composite placement system associated with the X and Y axis gantry mechanisms.

4.3 Stiffener Rib Consolidation Force Measurement

The results of the stiffener rib consolidation force data shown in figure 38 in section 3.1.3 suggest that after enough layers have been built up, the consolidation force experienced when placing higher layers remains consistent between each layer. It can be assumed that once the force between layers reaches equilibrium the height of printed layers would also remain consistent, and should approximately be the programmed layer height of 0.4 mm. Conversely, the data suggests that this was not the case for the initial layers of the print. The data shows that initial print layers experienced significantly higher consolidation forces than the equilibrium

value. It can be assumed that a higher consolidation force would have an effect on the resulting height of a printed layer and would produce a thinner layer. It can also be assumed that due to the parabolic decrease in consolidation force seen in the initial print layers, the height of those print layers must also have gone through some form of gradual increase between each layer until reaching the force equilibrium around layer 25, at which subsequent print layers should exhibit a consistent layer height of around 0.4 mm. It should be noted that the nature of the layer height increase in the initial layers is not yet understood, and it cannot be assumed that the layer height increase simply has an inverse relationship to the consolidation force data. It must be recognized that only the consolidation force, not the consolidation pressure, is directly measured. As the tow thins, it also spreads, increasing the tow width and the area over which the consolidation face of the nozzle applies force. This increased area suggests that the actual consolidation pressure does not exactly track the consolidation force, and that a more complicated relationship between consolidation force and printed layer height may exist.

In composite manufacturing, an increase in consolidation force generally results in a decrease in void content and an increase in quality of the composite [70]. Therefore, it would be expected that a large decrease in consolidation force like the one seen in the consolidation force test results would accompany a significant increase in void content. Instead, the results of the constituent volume fraction analysis found that the void volume fraction showed little to no change through the height of the stiffener beam samples. Furthermore, the results of the stiffener rib specimen microscopy analysis did not show any significant increase in void content through the height of the specimens. While minor increases in void content were seen in some of the specimens, like the center voids of the 0.4 mm layer height specimens, no major increases in void concentration through the height were observed for any of the specimens. Considering the

magnitude of the decrease in consolidation force recorded in the consolidation force measurement test, the results of the constituent volume fraction test and the microscopy analysis are especially surprising. Even with such a large decrease in consolidation force through the height of the stiffener rib samples, the results of the constituent volume fraction test and the microscopy analysis show that the composite placement system is able to manufacture tall, narrow stiffener ribs which exhibit high fiber volume fractions of around 50 % and low void volume fractions of around 5% with good reinforcement distribution.

4.4 Force Measured Stiffener Rib Volume Fraction Measurement

The results of the constituent volume fraction analysis of the force measured stiffener beam shown in figure 39-44 in section 3.1.4 showed that the void content of the force measured beam was lower than the void content of the original 0.4 mm layer height stiffener beam, despite the two stiffener beam samples being produced using the same process parameters. The most likely cause of this discrepancy was the use of the consolidation force measurement system to find the first print layer Z-axis position. Before the consolidation force measurement system was installed, the magnitude of consolidation force being applied on the first layer of printing was calculated using the spring displacement in the placement head. After the consolidation force measurement system was installed, that system was used to find the Z-position at which the first print layer would experience the same consolidation force, which was about 10 N. It is possible that the original method of calculating the first layer consolidation force was not accurate, and the actual first layer consolidation force experienced when printing was less than what was calculated using spring displacement. This would also cause the consolidation force of all subsequent print layers to be lower as well because the Z-axis movement between print layers was kept constant and the Z-axis position that each print layer was printed at was based on the

position of the first print layer. This was confirmed by examining the results of preliminary testing performed with the consolidation force measurement system and comparing them with the old spring constant. The preliminary testing found that the placement head nozzle would just contact the print bed at a Z-axis height of 0.7 mm, and also found that the desired consolidation force of about 10 N occurred at the Z-axis height of -1.0 mm. This equates to a total spring displacement of 1.7 mm for a consolidation force of 10 N. Calculating a spring constant from this results in a spring constant of 5.88 N/mm, which is less than the assumed 7.5 N/mm spring constant used prior to the installation of the consolidation force measurement system. Therefore, the consolidation force experienced when printing the original 0.4 mm layer height stiffener rib sample was lower than anticipated and was lower than the consolidation force experienced when printing the force measured stiffener rib sample, resulting in a lower void content in the force measured sample.

The results of the constituent volume fraction analysis showed that both the original stiffener rib samples and the force measured stiffener rib sample exhibited a high fiber volume fraction, of over 50%, and a low void volume fraction, of below 5%. These properties would be sufficient for many commercial composite applications outside of the aerospace industry. Additively manufactured composite grid stiffened panels exhibiting these properties could be used as shear webs in the cores of wind turbine blades, and the ability to additively manufacture them would be extremely beneficial to that industry. Additionally, composite parts exhibiting these properties could be used in automotive applications. The ability to additively manufacture high quality continuous fiber composite parts may allow for the replacement of many traditionally manufactured parts with composite ones, which could lead to improved performance in vehicles.

4.5 Force Measured Stiffener Rib Microscopic Inspection

The results of the force measured sample microscopic inspection shown in figure 45 in section 3.5 are very similar to the results of the first microscopic inspection shown in figures 35-37 in section 3.2. However, they are significant due to the sample tested. This microscopic inspection was performed on the same stiffener beam sample that was measured for consolidation force during printing. The results provide evidence that the large parabolic decrease in consolidation force experienced during printing of the different layers of the sample had little effect on the quality of the composite material through the height of the stiffener beams. The results suggest that the composite placement system is able to manufacture high quality continuous fiber composite stiffener beams exhibiting high fiber volume fractions and low void volume fractions with radically reduced tooling requirements.

4.6 Stiffener Grid Intersection Geometry Measurement

The results of the stiffener grid intersection geometry measurement shown in Table 2 in section 3.6 suggest that the tow spreading procedure was effective at spreading the commingled tow when printing the intersection. However, the degree of spreading achieved needs to be discussed further. As discussed previously the goal of the tow spreading at the intersections is to reduce the inherent buildup of material that would occur at the intersections due to their being twice the number of layers there. In order to maintain a constant height over the entire stiffener grid structure throughout the manufacturing process, the height of the layers at the intersection nodes need to be effectively halved by the tow spreading process [71]. It would be expected, then, that this process would also result in the width of the tow at the intersection nodes to double so as to conserve the cross-sectional area of the tow. The results of the stiffener grid sample height measurements showed that the height of the sample at the intersection node was

even lower than the rest of the sample, suggesting that the width of the tow at the node should be slightly greater than double. However, the stiffener grid sample width measurement results show that the width of the tow at the intersection node was nowhere near double the width of the tow at the rest of the sample. In order to fulfill the conservation of mass the "missing" material must have been displaced during processing to an area not represented in the width and height measurements, such as the corners formed at the intersection stiffeners. It can be assumed that the displaced material would be thermoplastic matrix material as it was molten and flowed during processing. Furthermore, it can be assumed that the displacement of the matrix material would alter the composition of the material at the intersection node, resulting in a difference in constituent volume fractions at the node.

4.7 Stiffener Grid Intersection Consolidation Force Measurement

The grid stiffener intersection consolidation force measurement results for the first layer shown in figure 46 and 47 in section 3.7 showed that the consolidation force experienced before the intersection node was higher than the consolidation force experienced after the intersection node, despite the programmed placement head position being the same. It is possible that this is caused by the increased consolidation force experienced at the intersection node. When printing the intersection node, the increased consolidation forces the commingled tow material to spread thinner and compact more. It is possible that this also helps better orient the reinforcement fibers within the tow. After the consolidation force is reduced, the tow stops spreading and returns to its original shape, however the increased orientation of the reinforcement fibers may be preserved. This would decrease the consolidation force experienced because the tow would have less overlapping and misaligned reinforcement fibers. It is also possible that the increased consolidation force experienced before the intersection node has to do with the direction that the

placement head travelled to reach the Z-axis position for printing. It's possible that if the placement head moves from a higher position and travels downward to reach the printing position that some form of friction build up is experienced when compressing the spring in the placement head, increasing the total consolidation force felt by the material. If the placement head moves from a lower position upward to reach a printing position the compression spring is instead relaxed, and the friction in the system is not felt in the consolidation force.

The results of the stiffener grid intersection consolidation force measurement for all layers of the sample shown in figure 49 in section 3.7 suggest that more print layers need to be built up at the intersection node to reach the point at which the consolidation force experienced when placing higher layers remains consistent between each layer. As discussed in section 3.3, it can be assumed that once the force between layers reaches equilibrium the height of the printed layers would also remain consistent, and should approximately be the programmed layer height of 0.4 mm. This suggests that at around layer 20, the stiffener rib regions of the intersection point sample reached equilibrium and began printing subsequent print layers to be 0.4 mm tall. However, the intersection node did not reach equilibrium until layer 30. At layer 30, the intersection node finally reached equilibrium and subsequent print layers were manufactured to be 0.4 mm tall. But, because the intersection node of each print layer consisted of two overlapping stiffener rib directions, the height of the individual layers at the intersection node would be half the height and would each be about 0.2 mm tall.

To discuss the results of the multi-layer consolidation force data more easily, a modified version of the data was plotted with respect to time instead of distance and is shown in figure 57. Plotting the data with respect to time widens the intersection node region of the graph as the

printing speed was reduced during that section. The wider intersection node region makes it easier to see trends in the data.

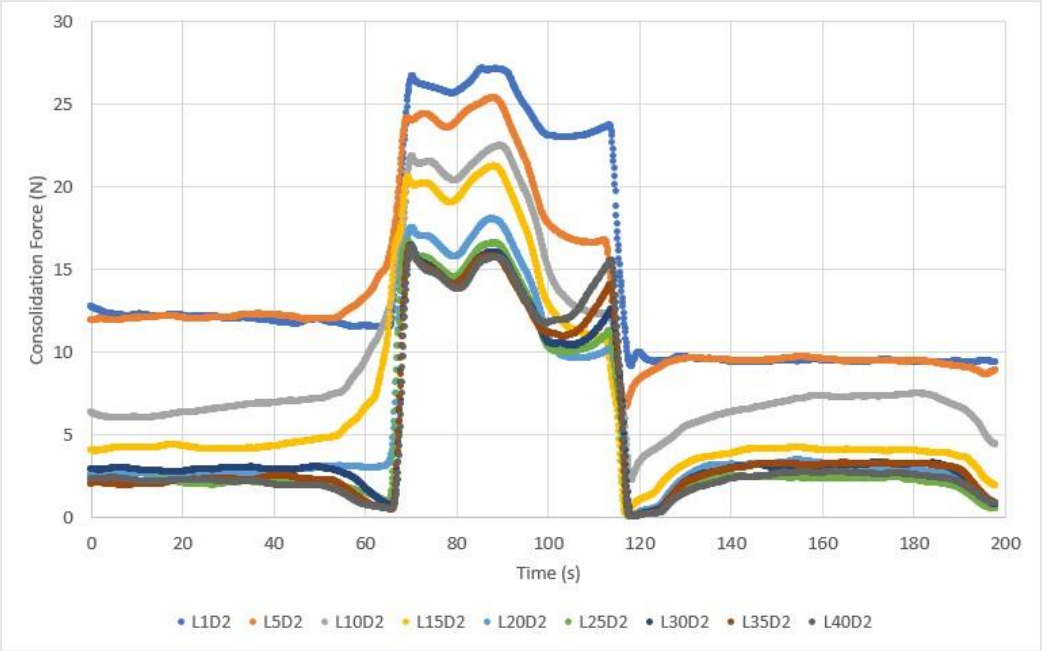

Figure 57: Stiffener grid intersection multi-layer consolidation force data plotted versus time instead of distance.

The results of the multi-layer consolidation force analysis showed that at lower layers the consolidation force increased before reaching the intersection node, but at higher layers the consolidation force decreased before reaching the intersection node. This is most likely due to the changing surface geometry of the intersection point print as more print layers were added. While printing the intersection point sample, it was observed at lower print layers that the intersection node appeared as a bump and was taller than the rest of the sample, However, the intersection node of the finished sample was found to be shorter than the rest of the sample, as described in section 3.2.1. Therefore, during printing the intersection node must have transitioned from exhibiting a convex, protruding profile to exhibiting a concave, sunken profile

as print layers were added. Figure 58 shows a cartoon depicting the printing of the intersection node at lower, middle, and higher print layers. The cartoon shows the changing profile of the intersection node top surface, from a convex bump at lower layers to a concave pit at higher layers.

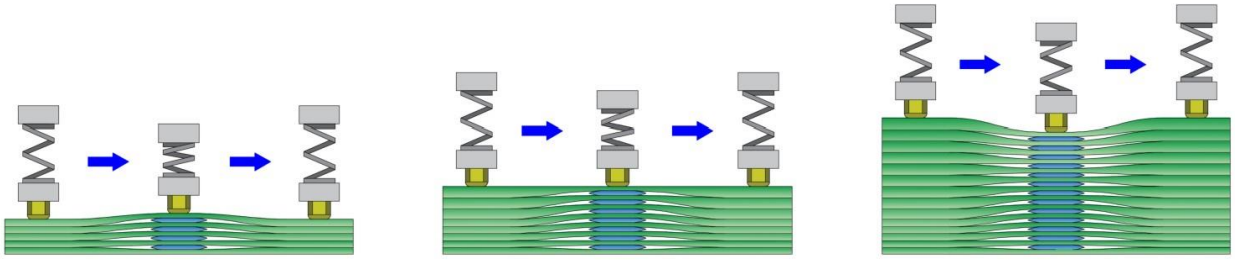

Figure 58: Cartoon showing the printing of the intersection node at lower (left), middle (middle), and higher (right) print layers.

The presence of a changing intersection node top surface profile is supported by the results shown in the multi-layer graph shown in figure 57 at the region just before the intersection node. Lower print layers exhibit an increasing consolidation force before the intersection node, suggesting that the amount of compression in the placement head was increasing. If the intersection node was a convex bump, then the region before the node would be an upward slope. Printing along this upward slope would force the placement head to compress more, increasing the consolidation force experienced. Furthermore, the graph shows that higher print layers exhibited a decreasing consolidation force before the intersection node, suggesting that the amount of compression in the placement head was decreasing. If the intersection node at that point had transitioned into a concave pit, then the region before the node would be a downward slope. Printing along this downward slope would allow the placement head to lengthen and would decrease the consolidation force experienced. Figure 59 illustrates the

lengthening of the placement head at the downward slope before the increased consolidation region. Additionally, it can be seen that at layer 20, the region before the intersection node appears relatively horizontal, suggesting that the consolidation force experienced before the intersection node remained consistent right up until the increase in force at the node. It can be concluded, then, that based on the data the intersection node of the print was equal in height to the rest of the print at layer 20.

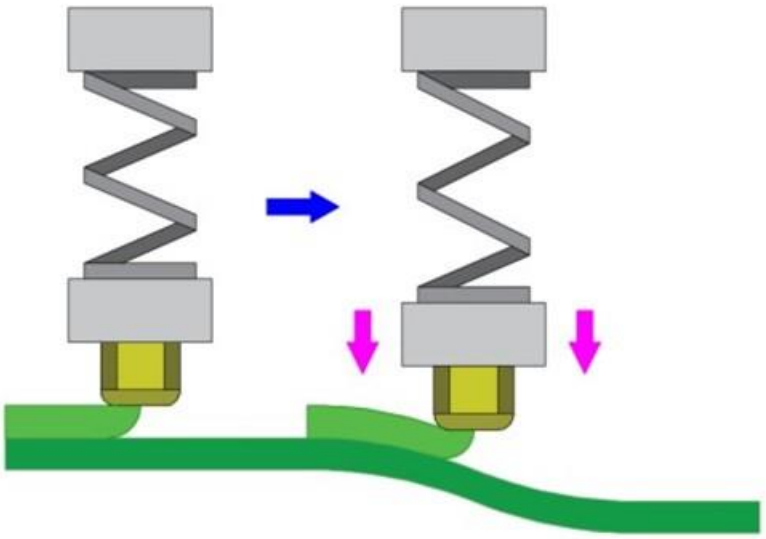

Figure 59: Illustration of the lengthening of the placement head experienced when printing over the edge of a downward slope.

The results of the multi-layer consolidation force analysis also showed that an increase in consolidation force with increasing layer count occurred at the end of the intersection node. The results suggest that this increase was due to the changing height of the stiffener grid intersection sample. As discussed above, the results of the intersection point sample height measurement discussed in section 3.6 showed that the height of the sample at the intersection node was about 1 mm shorter than the height of the rest of the sample. This height difference means that there was

an upward slope in the sample at the end of the intersection node region. When printing on this upward slope, it is possible that the front edge of the placement nozzle contacted the slope, forcing the placement nozzle to compress and increasing the consolidation force experienced during the upward slope. Figure 60 illustrates the placement nozzle contacting the upward slope.

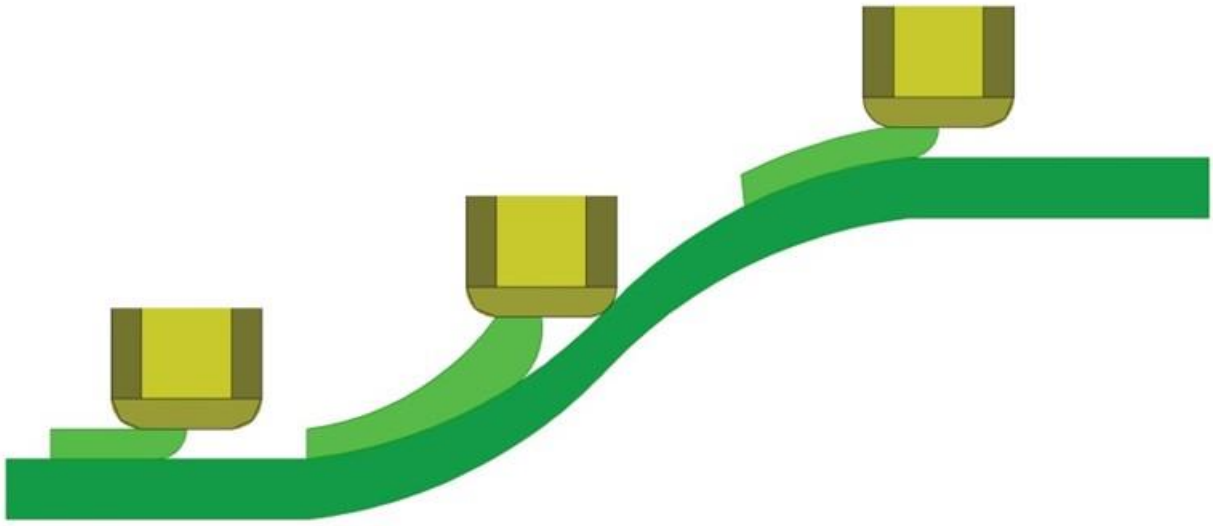

Figure 60: Illustration of placement nozzle contacting the upward slope at the end of the intersection node.

If the front edge of the placement nozzle was contacting the upward slope while printing the end of the intersection node, this would not just increase the consolidation force experienced. As shown in the illustration in figure 60, the upward slope would also cause the height of the print layer placed on the slope to be taller than intended. If the upward slope was causing the nozzle to compress more, this would in turn cause the amount of consolidation force experienced by the material when printing the upward slope to be significantly less than intended, resulting in these taller layers. However, this effect would not be experienced once the nozzle crested the slope. The result of this would be that the thicker layers at the upward slope would cause the

slope to shift backward, happening sooner and sooner along the print path. This shifting of the upward slope at the end of the intersection node would result in the increased consolidation force caused by the front edge of the placement nozzle contacting the slope to increase in magnitude with increasing layers, as is seen in the multi-layer graph data shown in figure 57. The results suggest that if the equal height of the intersection node and stiffener rib regions at layer 20 was preserved through the remaining layers of the print, then the upward slope after the intersection node would not be present and the consolidation force experienced at higher layers would be more consistent. The results suggest that the difference in the layer that an equilibrium was reached at the intersection node versus the layer that an equilibrium was reached at the stiffener rib regions caused the formation of the concavity at the node. If the consolidation force applied at the intersection node were reduced, it is possible that it would shift the layer at which a consolidation force equilibrium was experienced.

4.8 Stiffener Grid Intersection Volume Fraction Measurement

The results of the stiffener grid intersection volume fraction measurement showed that the fiber volume fraction at the intersection node was much higher than at the rest of the sample and was roughly 6% higher than the unprocessed fiber volume fraction of the commingled feedstock. The results suggest that some of the matrix material must have been removed or moved outside of the area of the intersection node pyrolysis specimen prior to testing. The removal of matrix material most likely occurred during cutting of the intersection node specimens. Figure 61 shows a closeup of the intersection node of the uncut intersection point sample.

Figure 61: Close-up of intersection node of the stiffener grid intersection point sample.

When looking closer at the intersection node of the uncut intersection point sample, shown in figure 61, it can be seen that in the front corner of the intersection node there is a darker, orange region. This darker hue represents a large concentration of matrix material. This suggests that, when printing the intersection node, the higher consolidation force squished the matrix material out towards the corners of the intersection node where it collected and built up. This is significant when looking at a closeup of the intersection node pyrolysis and microscopy specimens, which are shown in figure 62.

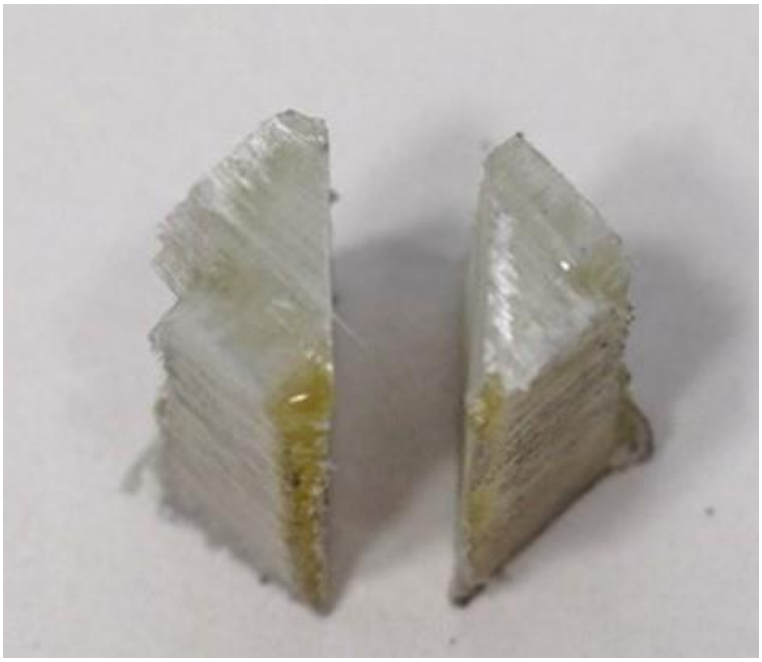

Figure 62: Microscopic inspection specimen C1M (left) and constituent volume fraction specimen C1V (right) of the intersection node.

When looking at the front of the two specimens taken from the intersection node, it can be seen that the majority of the orange hue matrix rich region is on the C1M specimen, which was reserved for microscopic inspection. It can be seen that the C1V specimen, which was used for volume fraction analysis, had much less of the resin rich area. It is possible that this is the reason that the fiber volume fraction is so high at the intersection node. Due to a broken positioning mechanism on the laboratory precision saw used to cut the intersection node specimens, the blade had to be manually positioned by eye in the center of the node. The image shows that the position of the cut was slightly off and left more of the matrix rich region with the microscopic inspection specimen than with the volume fraction analysis specimen.

The results of the stiffener grid void volume fraction measurement showed that the void content increased at the intersection node and was highest in the specimens located immediately

after the intersection node, suggesting that some aspect of the overlapping print layers at the node is encouraging the formation of voids. The cause of this is most likely related to the changing profile of the top surface of the intersection point sample. The height of the intersection node was about 1 mm shorter than the height of the stiffener rib regions of the print sample, resulting in an upward slope at the top profile of the sample at the end of the node. As discussed in section 4.2, it is possible that the front edge of the placement nozzle contacted the upward slope while printing, causing the consolidation force measured by the system to increase while simultaneously causing the consolidation force experienced by the commingled tow to be significantly reduced. It is possible that the reduced consolidation force experienced at the upward slope allowed for the formation of a higher concentration of voids at the slope. This is supported by the results of the void volume fraction of the S5 specimens, which were located immediately after the stiffener rib specimens exhibiting the high void content. The results show that the void volume fraction of the S5 specimens was much lower than the S4 specimens. This suggests that some feature of the S4 specimens was causing the increased void concentration, such as an upward slope. This is supported further when inspecting a side view image of the S4 specimen before it was tested, as shown in figure 63. In this image it can be clearly seen that the top surface profile of the S4 specimen exhibits a clear upward slope while the top surface profile of the S5 specimen is flat, providing evidence that the upward slope existed in the S4 specimens.

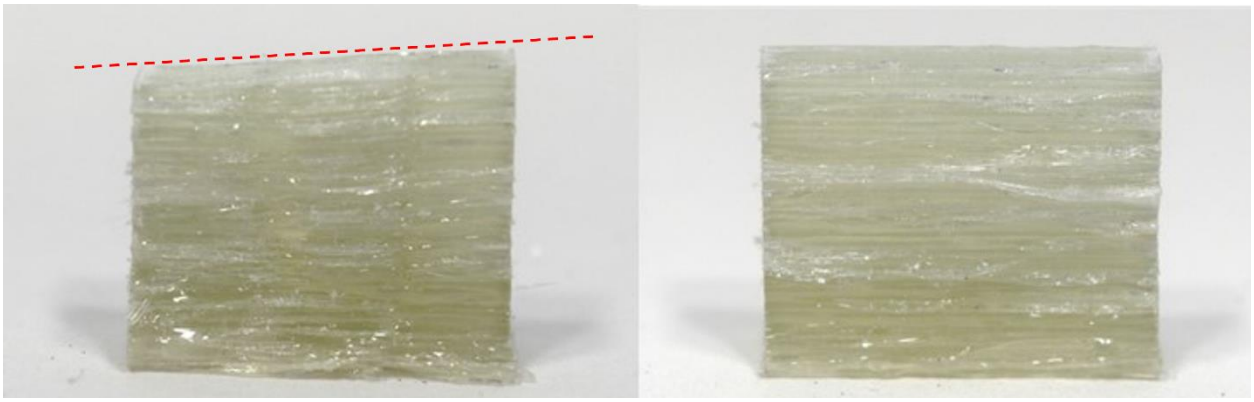

Figure 63: Comparison of the D1S4 (left) and D1S5 (right) specimens of the stiffener grid intersection sample.

The results suggest that the height difference between the intersection node and the stiffener rib regions of the intersection point sample resulted in a higher concentration of voids in the composite following the intersection node. If instead an equal height was maintained after it was reached at layer 20, the upward slope after the intersection node would not be present and the void volume fraction of the composite after the node would be lower.

4.9 Stiffener Grid Intersection Microscopic Inspection

The results of the stiffener grid intersection microscopy showed that the print layers of the two stiffener rib directions were offset from each other, and that large voids formed at the edges of the print layers. This was due to the two different stiffener rib directions of the stiffener grid intersection print sample. As the commingled tow material is compressed during printing, the matrix material is squeezed to the edges of the tow where it collects, as was shown in the high aspect ratio stiffener rib microscopy results. For two overlapping stiffener ribs perpendicular to each other, this results in regions of the overlap which consist of layers of the

matrix rich region of one stiffener beam direction sandwiched between reinforcement rich layers of the other stiffener beam direction. This is illustrated in figure 64.

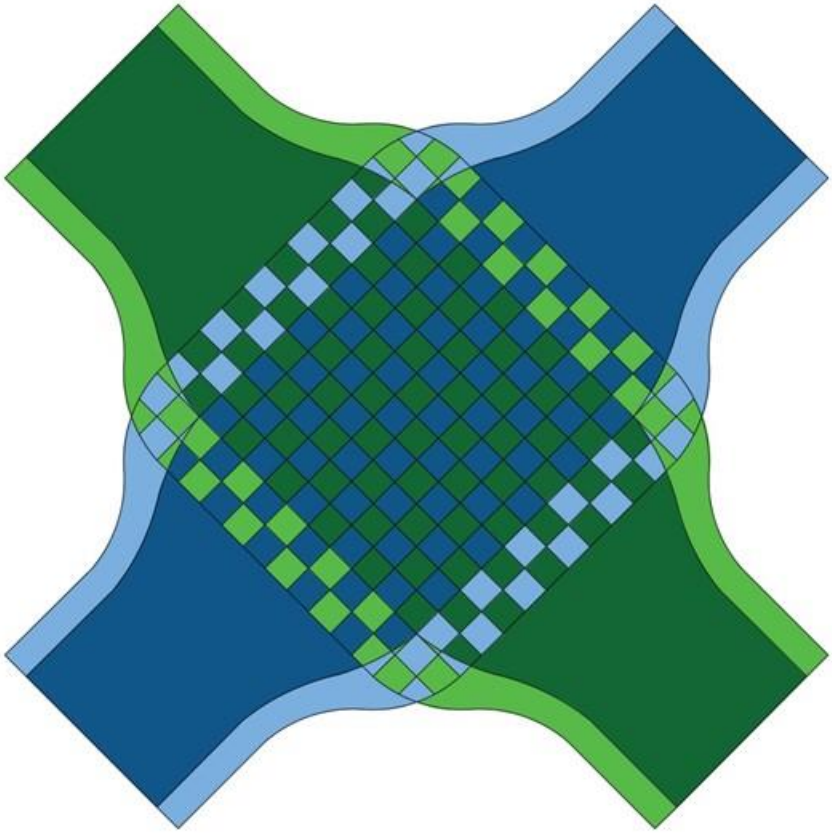

Figure 64: Illustration of the intersection node showing composition of print layers.

Figure 64 shows a drawing of the intersection node of the print sample. The two stiffener rib directions are represented by the different colors, with direction 1 represented by blue and direction 2 represented by green. As explained above, the compression of the placement head on to the commingled tow during printing squeezes the material and forces excess matrix towards the edges of the print layers where it collects. Comparing the result of the intersection node width measurement in section 3.6 with the dimensions of the placement nozzle described in

section 2.1.2 confirm that the diameter of the face of the placement nozzle is notably larger than the width of the spread tows at the intersection node, and thus the whole width of the print layers were still being consolidation while printing the node. The resin rich areas on the sides of the print layers are represented by the lighter colored blue and green regions. The checkered regions represent the areas of overlap in the intersection node, with the colors of the checkered pattern signifying what material is layered at that region. It can be seen that if the 45° cut isolating the volume fraction specimen and the microscopy specimen was made perfectly in the middle of the intersection node, and if the amount of material removed during polishing of the microscopy sample was negligible, then the microscopy specimen should exhibit completely resin rich areas on the sides of the specimen and should not exhibit the alternating fiber rich and then resin rich layers as are observed in the image. Figure 65 shows the region of the intersection node which would contain this perfectly cut triangular specimen. Notice that on the sides of the polished surface, which for reference is the hypotenuse of this triangular region, the composition of the material consists of layers of the matrix rich region of both the direction 1 stiffener rib and the direction 2 stiffener rib. The result would be that the sides of the microscopy would show completely resin rich areas, and the reinforcement would start and end at around the same position between each layer.

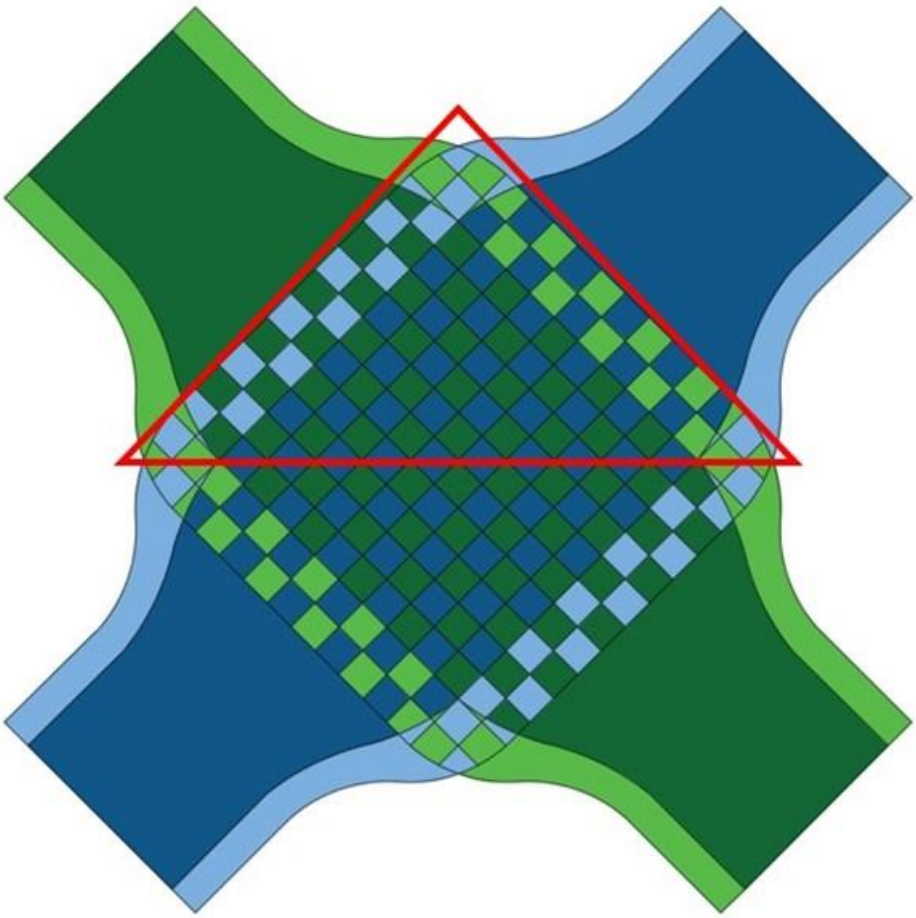

Figure 65: Illustration of intersection node showing micrograph specimen with polishing surface at center of node.

In reality, it cannot be assumed that a negligible amount of material was taken off during polishing. Instead, it should be assumed that enough material was removed during sanding and polishing of the microscopy specimen that the polishing surface was shifted up, reducing the size of the triangular specimen region of the intersection node. If the polishing surface was shifted up, then the composition of the layered material at the edges of the specimen would change. This is shown in figure 66.

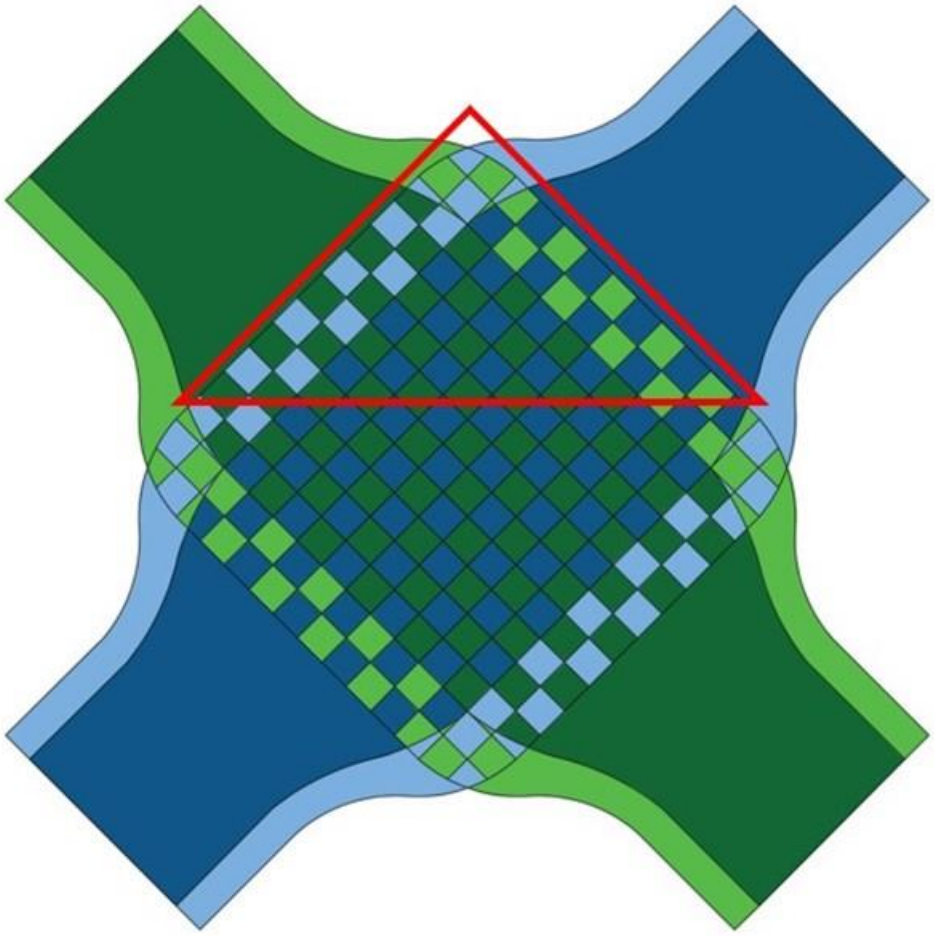

Figure 66: Illustration of intersection node showing actual shape of micrograph specimen after the first polish.

The triangular region shown in figure 66 more accurately represents the specimen shown in the microscopic inspection images. It can be seen that the regions on the sides of the polishing surface no longer contain layers of the resin rich areas from both stiffener rib directions. Instead, the sides of the polishing surface of the specimen now contain regions consisting of layers of the resin rich areas from one stiffener rib direction layered between the reinforcement rich areas of the other stiffener rib direction. This would result in alternating layers of matrix rich bands

between reinforcement rich layers at the edges of the microscopy specimen. It is for this reason that the matrix rich bands between reinforcement rich layers are observed in the microscopic inspection images.

When the intersection node was cut along the 45° angle it exposed these regions and resulted in the sides of the microscopy specimen showing the alternating matrix rich and reinforcement rich layered areas. The results of the microscopic inspection suggest that during the printing of the intersection node, large voids formed at these matrix rich bands at the edges of print layers, causing the void content of the intersection node to be higher than expected. These results support the results of the constituent volume fraction analysis, which found that the void concentration at the intersection node was higher than the void content of the stiffener rib regions of the print before the intersection node. It is possible that applying a lower consolidation force when printing the intersection node would not only minimize the difference in height between the intersection node and the stiffener rib regions of the intersection point sample, as explained earlier, but would also reduce the size of the resin rich areas on the sides of the print layers at the intersection node. This in turn would reduce the size of the alternating matrix rich and reinforcement rich layered regions of the intersection node where large voids were found to form. Decreasing these regions may decrease the size of the voids that form at those regions, resulting in a higher quality composite material at the intersection node with a lower void volume fraction.

The results of the second microscopic inspection of the stiffener grid intersection showed that while the width of the specimen decreased due to the sanding back of the inspection surface, the large voids at the edges of the specimen appeared to stay relatively the same size and concentration as was observed in the first microscopic inspection of the stiffener grid

intersection. The reason for the edge voids staying relatively the same size is illustrated in figure 67.

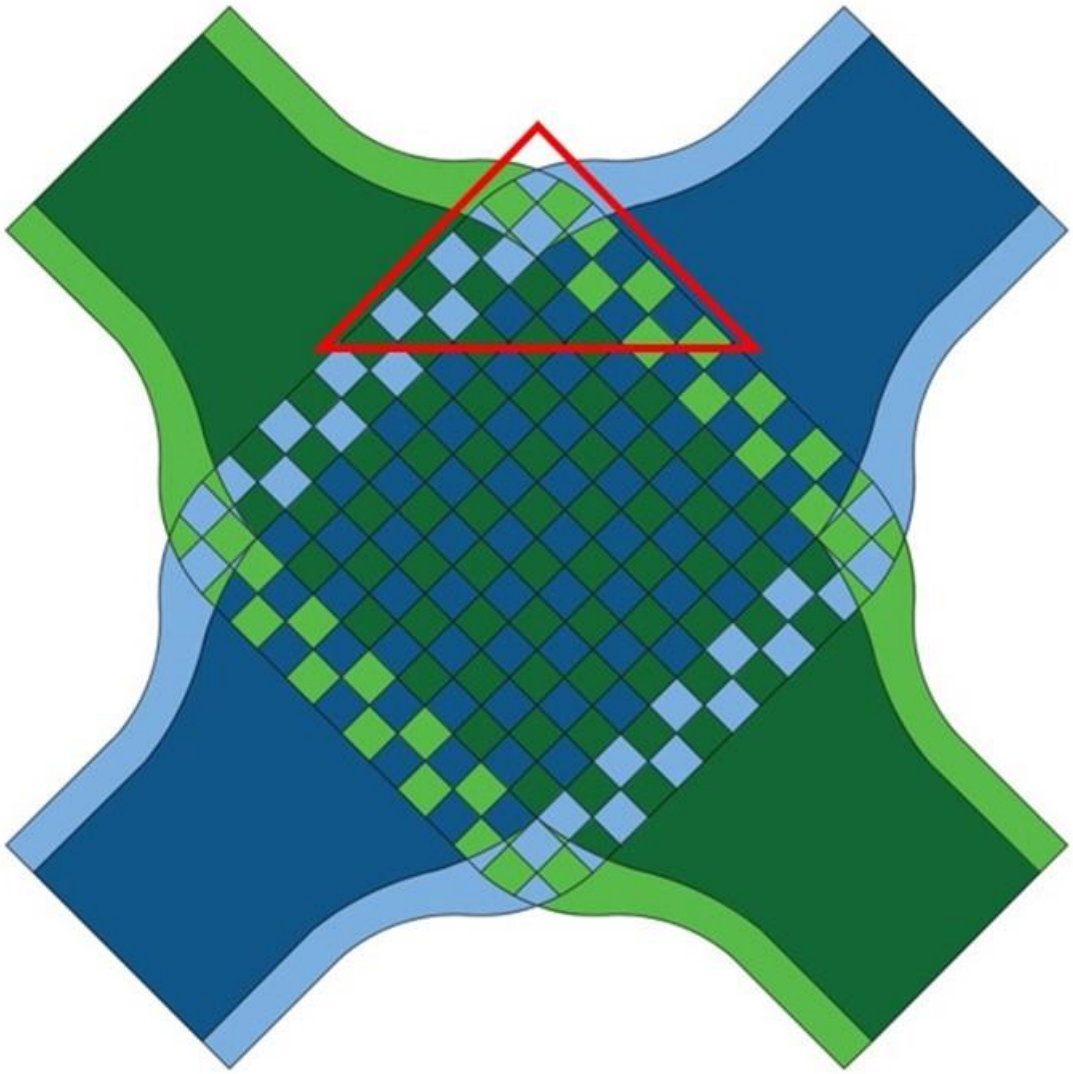

Figure 67: Illustration of the intersection node showing the shape of the micrograph specimen after the second polish.

Figure 67 shows the same illustration of the intersection node with a triangular region representing the second microscopic inspection specimen. It can be seen that the triangular

region is much smaller than the triangular region previously shown to represent the first microscopic inspection specimen. This is due to the sanding back of the polishing surface of the specimen in order to observe how the print layer geometry and void distribution would change with depth into the specimen. When looking at the sides of the polishing surface of the triangular region, it can be seen that the sides contain the same regions consisting of layers of the resin rich areas from one stiffener rib direction layered between the reinforcement rich areas of the other stiffener rib direction. However, it can be seen that the length of the polishing surface containing this region is the same in this specimen as was contained in the polishing surface of the first microscopic inspection specimen. Even though the overall width of the second microscopic inspection specimen decreased when the polishing surface was sanded back, the width of the alternating resin rich and matrix rich layer regions on the sides of the specimen did not change.

5 Future Work

A significant defect of the samples manufactured using the composite placement system is the rough and wavy texture exhibited on the side walls of the samples. Such a texture would be unacceptable in the composite manufacturing industry. Manufacturing samples with smooth, even walls would require some modification to the system. Replacing the placement nozzle with a consolidation roller system, which could apply a consolidation force more evenly over a larger area, may result in an improvement to the texture of the walls. Additionally, a mechanical guide or slot defining the shape of the print layer could be installed immediately after the placement nozzle or roller, forcing the tows to conform to a defined geometry. Regardless, some form of modification to the system aimed at improving the edges of printed layers is required to develop the composite placement system manufacturing method into an industry desired technology.

The results of the consolidation force measurement tests also demonstrated the lack of the ability of the composite placement system to fully control the consolidation force, and instead is only capable of producing a resulting consolidation force through its control of the placement head position. Incorporation of a Z prime axis, in the form of a stepper motor controlled screw system capable of moving the placement head up and down independent of the movement of the gantries, which was wired in a feedback loop with the consolidation force measurement system would allow for full control of the consolidation force. This would have profound impact on the manufacturing of multi-layered structures, as the system would be capable of printing these structures such that the consolidation force experienced at each layer of the print was the same. However, this too would have limitations, as it is limited to controlling the consolidation force experienced. For composite manufacturing, a more desired metric for control would be the consolidation pressure experienced, as that also incorporates the geometry of the printed layers.

The use of optical or thermal cameras actively measuring the printed tow width, coupled with the feedback controlled consolidation force system, would allow for full control of the consolidation pressure during printing. Both the use of a Z prime axis as well as the use of cameras to actively measure tow width have been pursued at the CMMS laboratory, however the successful implementation of either technology has yet to be fully realized.

An issue with the intersection nodes was that the top wasn't flat. This is especially problematic if future studies want to pursue additively manufactured grid stiffened sandwich cores, which would need a flat top surface to build the top face sheet of the sandwich structure onto. The results showed that the relationship between layer count and difference in height of the stiffener rib height and intersection node height was non-linear. A more in-depth study investigating the relationship between intersection node consolidation force and the print layer at which the height of the intersection node and the stiffener ribs was the same would be beneficial to the manufacturing of the sandwich panel structures.

6 Conclusions

This study demonstrates that the use of the composite placement system for the manufacture of high aspect ratio grid stiffener ribs and grid stiffener intersections with radically reduced tooling is effective. High aspect ratio grid stiffener ribs and grid stiffener intersections were additively manufactured while the consolidation force experienced was measured. The quality of the composite in these samples was analyzed by constituent volume fraction analysis through pyrolysis and by microscopic inspection. Volume fraction analysis results show that manufactured stiffener ribs and stiffener grid intersections exhibit high fiber volume fractions and low void volume fractions which remain consistent through the height of the samples. Consolidation force measurement results show that a significant decrease in force is experienced between print layers. Overcoming this significant decrease in force between print layers would require the incorporation of feedback control of either force, pressure, or height to the composite placement system. Microscopic analysis results show that the majority of voids collect at the edges of print layers leading to an increase in void content at the intersection node and potentially masking any quality gradient through the height of samples that may exist. The large presence of voids at the edges of the print layers is related to the lack of consolidation pressure able to be built up at the edges due to lateral flow. The results of this study show the high potential for the manufacturing of high quality high aspect ratio continuous fiber composite grid stiffener structures through direct digital manufacturing technologies without the need for tooling.

References

[1] J. Mack, O. McGregor and P. Mitschang, "Prepreg Lay-up Technology for Manufacturing of Lattice Structure Fuselage Sections," *European Conference on Composite Materials,* 2014.

[2] A. Forcellese, V. Pompeo, M. Simoncini and A. Vita, "Manufacturing of Composite Isogrid Structures by 3D Printing," *Procedia Manufacturing,* no. 47, pp. 1096-1100, 2020.

[3] P. M. Wegner, J. E. Higgins and B. P. VanWest, "Application of Advanced Grid-Stiffened Structures Technology to the Minotaur Payload Fairing," *American Institue of Aeronautics and Astronautics,* 2002.

[4] S. Ananth and T. J. Whitney, "Stability Analysis of Additively Manufactured Isogrid," University of Dayton, Dayton, 2015.

[5] H. Khosravi and R. Eslami-Farsani, "Reinforcing Effect of Surface-Modified Multiwalled Carbon Nanotubes on Flexural Response of E-Glass/Epoxy Isogrid-Stiffened Composite Panels," Polymer Composites, 2018.

[6] S. M. Huybrechts, S. E. Hahn and T. E. Meink, "Grid Stiffened Structures: A Survey of Fabrication, Analysis and Design Methods," Air Force Research Lab, New Mexico.

[7] S. Kidane, "Buckling Analysis of Grid Stiffened Composite Structures," *LSU Master's Thesis,* no. 1504, 2002.

[8] D. Maricherla, "Advanced Grid Stiffened Composite Structures," *LSU Master's Thesis,* no. 916, 2005.

[9] H. Ebrahimnezhad-Khaljiri, R. Eslami-Farsani, H. Khosravi and A. Shahrabi-Farahani, "Improving the Flexural Properties of E-Glass Fibers/Epoxy Isogrid Stiffened Composites through Addition of 3-Glycidoxypropyltrimethoxysilane Functionalized Nanoclay," *Silicon,* vol. 12, pp. 2515-2523, 2020.

[10] T. D. Kim, "Fabrication and testing of thin composite isogrid stiffened panel," *Composite Structures,* no. 49, pp. 21-25, 2000.

[11] F. Gary, "Composites Evolution," 19 January 2021. [Online]. Available: https://compositesevolution.com/resources/what-is-automated-fibre-placement-afp/. [Accessed 18 January 2022].

[12] Z. Peng, S. Ronglei, Z. Xueying and H. Lingjin, "Placement Suitability Criteria of Composite Tape for Mould Surface in Automated Tape Placement," *Chinese Journal of Aeronautics,* vol. 5, no. 28, pp. 1574-1581, 2015.

[13] J. Tierney and J. W. Gillespie, "Modeling of In Situ Strength Developent for the Thermoplastic Composite Tow Placement Process," University of Delaware, Newark, 2005.

[14] W. M. van den Brink and W. J. Vankan, "Design for Manufacturing of Fuselage Panels with Curved Grid Stiffening," *17th International Conference on Composite Structures,* 2013.

[15] C. Zhao, M. J. Donough, B. Gangadhara Prusty and J. Xiao, "Influences of Ply Waviness and Discontinuity on Automated Fibre Placement Manufactured Grid Stiffeners," *Composite Structures,* no. 256, 2021.

[16] M. Azeem, H. Haji Ya, M. Axad Alam and M. Kumar, "Application of Filament Winding Technology in Composite Pressure Vessels and Challenges: A Review," *Journal of Energy Storage,* no. 49, 2022.

[17] F. H. Abdalla, S. A. Mutasher, Y. A. Khalid and S. M. Sapuan, "Design and Fabrication of Low Cost Filament Winding Machine," *Material & Design,* no. 28, pp. 234-239, 2007.

[18] F. C. Shen, "A Filament-Wound Structure Technology Overview," *Materials Chemistry and Physics,* no. 42, pp. 96-100, 1995.

[19] P. Mertiny and F. Ellyin, "Influence of the Filament Winding Tension on Physical and Mechanical Properties of Reinforced Composites," *Composites: Part A,* no. 33, pp. 1615-1622, 2002.

[20] M. Buragohain and R. Velmurugan, "Study of Filament Wound Grid-Stiffened Composite Cylindrical Structures," *Composite Structures,* no. 93, pp. 1031-1038, 2011.

[21] L. Sorrention, M. Marchetti, C. Bellini, A. Delfini and F. Del Sette, "Manufacture of high performance isogrid structure by Robotic Filament Winding," *Composite Structures,* no. 164, pp. 43-50, 2017.

[22] T. D. Kim, "Fabrication and Testing of Composite Isogrid Stiffened Cylinder," *Composite Structures,* no. 45, pp. 1-6, 1999.

[23] S. M. Huybrechts, T. E. Meink, P. M. Wegner and J. M. Ganley, "Manufacturing Theory for Advanced Grid Stiffened Structures," *Composites Part A,* vol. 33, pp. 155-161, 2002.

[24] T. Vialva, "Anisoprint Brings Continuous Fiber 3D Printing Technology to the UK," *3D Printing Industry,* 2019.

[25] C. J. Hunt, F. Morabito, C. Grace, Y. Zhao, B. K and S. Woods, "A Review of Composite Lattice Structures," *Composite Structures,* no. 284, 2022.

[26] D. Peeters, G. Clancy, V. Oliveri, R. O'Higgins, D. Jones and P. M. Weaver, "Concurrent Design and Manufacture of a Thermoplastic Composite Stiffener," *Composite Structures,* vol. 212, pp. 271-280, 2019.

[27] H. Wu, C. Lai, F. Sun, M. Li, B. Ji, W. Wei, D. Liu, X. Zhang and H. Fan, "Carbon Fiber Reinforced Hierarchical Orthogrid Stiffened Cylinder: Fabrication and Testing," *Acta Astronautica,* vol. 145, pp. 268-274, 2018.

[28] V. V. Vasiliev, V. A. Barynin and A. F. Rasin, "Anisogrid Lattice Structures - Survey of Development and Application," *Composite Structures,* vol. 54, pp. 361-370, 2001.

[29] S. W. Tsai and P. M. Manne, "Composite Grid Structures," Stanford University, Stanford, 1996.

[30] B. C. Kim, K. Potter and P. M. Weaver, "Continuous Tow Shearing for Manufacturing Variable Angle Tow Composites," *Elsevier,* no. 43, pp. 1347-1356, 2012.

[31] B. C. Kim, P. M. Weaver and K. Potter, "Manufacturing Characteristics of the Continuous Tow Shearing Method for Manufacturing of Variable Angle Tow Composites," *Composites: Part A,* vol. 61, pp. 141-151, 2014.

[32] E. Zympeloudis, K. Potter, P. M. Weaver and B. C. Kim, "Advanced Automated Tape Laying with Fiber Steering Capability Using Continuous Tow Shearing Mechanism," *21st International Converence on Composite Materials,* 2017.

[33] K. M. Warlick, "The Effect of Tow Shearing on Reinforcement Positional Fidelity in the Manufacture of a Continuous Fiber Reinforced Thermoplastic Matrix Composite via Pultrusion-Like Processing of COmmingled Feedstock," Colorado State University, Fort Collins, 2017.

[34] D. Wang, M. M. Abdalla and W. Zhang, "Buckling Optimization Design of Curved Stiffeners for Grid-Stiffened Composite Structures," *Composite Structures,* vol. 159, pp. 656-666, 2017.

[35] D. Wang, M. M. Abdalla and W. Zhang, "Sensitivity Analysis for Optimization Design of Non-Uniform Curved Grid-Stiffened Composite (NCGC) Structures," *Composite Structures,* vol. 193, pp. 224-236, 2018.

[36] D. Wang, M. M. Abdalla, Z.-P. Wang and Z. Su, "Streamline Stiffener Path Optimization (SSPO) for Embedded Stiffener Layout Design of Non-Uniform Curved Grid-Stiffened Composite (NCGC) Structures," *Computer Methods in Applied Mechanics and Engineering,* vol. 344, pp. 1021-1050, 2019.

[37] D. Wang, S.-Y. Yeo, Z. Su, Z.-P. Wang and M. M. Abdalla, "Data-Driven Streamline Stiffener Path Optimization (SSPO) for Sparse Stiffener Layout Design of Non-Uniform Curved Grid-Stiffened Composite (NCGC) Structures," *Computer Methods in Applied Mechanics and Engineering,* vol. 365, 2020.

[38] P. Parandoush and D. Lin, "A Review on Additive Manufacturing of Polymer-Fiber Composites," *Composite Structures,* vol. 182, pp. 36-53, 2017.

[39] B. Newman, C. Creighton, L. C. Henderson and F. Stojcevski, "A Review of Milled Carbon Fibres in Composite Materials," *Composites Part A: Applied Science and Manufacturing,* vol. 163, 2022.

[40] "3DXTECH Additive Manufacturing," [Online]. Available: https://www.3dxtech.com/product/carbonx-pa6-cf/. [Accessed 27 October 2022].

[41] T. Isobe, T. Tanaka, T. Nomura and R. Yuasa, "Comparison of Strength of 3D Printing Objects Using Short Fiber and Continuous Long Fiber," in *Conf. Series: Materials Science and Engineering*, 2018.

[42] M. Chapiro, "Current Achievements and Future Outlook for Composites in 3D Printing," *Reinforced Plastics,* vol. 60, no. 6, pp. 372-375, 2016.

[43] Z. Quan, Z. Larimore, A. Wu, J. Yu and X. Qin, "Microstructural Design and Additive Manufacturing and Characterization of 3D Orthogonal Short Carbon Fiber/Acrylonitrile-Butadiene-Styrene Preform and Composite," *Composites Science and Technology,* vol. 126, pp. 139-148, 2016.

[44] D. Ciccarelli, A. Forcellese, L. Greco, T. Mancia, M. Pieralisi, M. Simoncini and A. Vita, "Buckling Behavior of 3D Printed Composite Isogrid Structures," *Procedia CIRP,* vol. 99, pp. 375-380, 2021.

[45] A. J. Thilak Johnson and S. Paramasivam, "Compression Behavior of 3D Printed Isogrid Cylindrical Shell Structures using Experimental and Finite Element Modeling," *Polymer Composites,* vol. 43, no. 10, pp. 7278-7289, 2022.

[46] R. Matsuzaki, M. Ueda, M. Namiki, T.-K. Jeong, H. Asahara, K. Horiguchi, T. Nakamura, A. Todoroki and Y. Hirano, "Three-Dimensional Printing of Continuous-Fiber Composites by In-Nozzle Impregnation," *Scientific Reports,* 2016.

[47] X. Tian, T. Liu, C. Yang, Q. Wang and D. Li, "Interface and Perfomance of 3D Printed Continuous Carbon Fiber Reinforced PLA Composites," *Elsevier,* no. 88, pp. 198-205, 2016.

[48] P. Bettini, G. Alitta, G. Sala and L. Di Landro, "Fused Deposition Technique for Continuous Fiber Reinforced Thermoplastic," *Journal of Materials Engineering and Performance,* vol. 26, no. 2, pp. 843-848, 2017.

[49] "Mark Two," Markforged, 2019. [Online]. Available: https://markforged.com/3d-printers/mark-two?mfa=ga-search&adg=40301838887&kw=markforged&device=c&gclid=EAIaIQobChMInLeUioSI4QIVzrftCh0GaglPEAAYASAAEgKxnfD_BwE.. [Accessed 1 November 2022].

[50] "Desktop Metal Fiber Printer," Desktop Metal, [Online]. Available: https://www.desktopmetal.com/products/fiber. [Accessed 1 November 2022].

[51] D. R. Hetrick, S. H. Reza Sanei, C. E. Bakis and O. Ashour, "Evaluating the Effect of Variable Fiber Content on Mechanical Properties of Additively Manufactured Continuous Carbon Fiber Composites," *Journal of Reinforced Plastics and Composites,* vol. 40, no. 9-10, pp. 365-377, 2021.

[52] A. N. Dickson, J. N. Barry, K. A. McDonnell and D. P. Dowling, "Fabrication of Continuous Carbon, Glass and Kevlar Fibre Reinforced Polymer Composites Using Additive Manufacturing," *Additive Manufacturing,* vol. 16, pp. 146-152, 2017.

[53] F. Van Der Klift, Y. Koga, A. Todoroki, M. Ueda, Y. Hirano and R. Matsuzaki, "3D Printing of Continuous Carbon Fibre Reinforced Thermo-Plastic (CFRTP) Tensile Test Specimens," *Open Journal of Composite Materials,* vol. 6, 2016.

[54] J. M. Chacon, M. A. Caminero, P. J. Nunez, E. Garcia-Plaza, I. Garcia-Moreno and J. M. Reverte, "Additive Manufacturing of Continuous Fibre Reinforced Thermoplastic Composites using Fused Deposition Modelling: Effect of Process Parameters on Mechanical Properties," *Composites Science and Technology,* vol. 181, 2019.

[55] N. Ahmed Khan, "Prediction and Validation of Continuous Fiber Stiffened Plates Manufactured with Continuous Filament Fabrication," University of Texas, Arlington, 2020.

[56] W. Hao, Y. Lio, H. Zhou, H. Chen and D. Fang, "Preparation and Characterization of 3D Printed Continuous Carbon Fiber Reinforced Thermosetting Composites," *Polymer Testing,* vol. 65, pp. 29-34, 2018.

[57] M. E. Bourgeois and D. W. Radford, "Toolless Out of Build Plane Manufacturing of Intricate Continuous Fiber Reinforced Thermoplastic Composites with a 3D Printing System," Colorado State University, Fort Collins, 2019.

[58] P. A. Rodriguez, "Dynamic Mechanical Analysis for Quality Evaluation of Additively Manufactured Continuous Fiber Reinforced Thermoplastic Matrix Composites Subject to Manufacturing Defects," Colorado State University, Fort Collins, 2019.

[59] P. A. Rodriguez and D. W. Radford, "Effect of Applied Consolidation Pressure in Direct Digital Manufacture of Continuous Fiber Reinforced Composites," CAMX, Orlando, FL, 2017.

[60] *Jushi USA Fiberglass Co., Ltd., Irwindale, CA, USA.*

[61] "ASTM D792-20: Standard Test Methods for Density and Specific Gravity (Relative Density) of Plastics by Displacement".

[62] "ASTM D3171-15 Standard Test Methods for Constituent Content of Composite Materials".

[63] N. Aliheidari, J. Christ, R. Tripuraneni, S. Nadimpalli and A. Ameli, "Interlayer Adhesion and Fracture Resistance of Polymers Printed through Melt Extrusion Additive Manufacturing Process," *Materials and Design,* vol. 156, pp. 351-361, 2018.

[64] P. Wang, B. Zou, H. Xiao, S. Ding and C. Huang, "Effects of Printing Parameters of Fused Deposition Modelling on Mechanical Properties, Surface Quality, and Microstructure of PEEK," *Journal of Materials Processing Tech.,* vol. 271, pp. 62-74, 2019.

[65] S. Petersmann, P. Spoerk-Erdely, M. Feuchter, T. Wieme, F. Arbeiter and M. Spoerk, "Process-Induced Morphological Features in Material Extrusion-Based Additive Manufacturing of Polypropylene," *Additive Manufacturing,* vol. 35, 2020.

[66] L. Wang and D. J. Gardner, "Effect of Fused Layer Modeling (FLM) Processing Parameters on Impact Strength of Cellular Polypropylene," *Polymer,* vol. 113, pp. 74-80, 2017.

[67] H. R. Vanaei, M. Deligant, K. Raissi, M. Shirinbayan, J. Fitoussi, S. Khelladi and A. Tcharkhtchi, "Toward the Unverstanting of Temperature Effect on Bonding Strength, Dimensions and Geometry of 3D-Printed Parts," *Journal of Materials Science,* vol. 55, pp. 14677-14689, 2020.

[68] A. Vaxman and M. Narkis, "Void Formation in Short-Fiber Thermoplastic Composites," Technion-Israel Institute of Technology, Haifa, 1989.

[69] H. E. N. Bersee and A. Beukers, "Consolidation of Thermoplastic Composites," *Journal of Thermoplastic Composite Materials,* vol. 16, no. 5, pp. 433-455, 2003.

[70] M. Mehdikhani, L. Gorbatikh, I. Verpoest and S. V. Lomov, "Voids in Fiber-Reinforced Polymer Composites: A Review on their Formation, Characteristics, and Effects on Mechanical Performance," *Journal of Composite Materials,* vol. 53, no. 12, pp. 1579-1669, 2019.

[71] A. Alhajahmad and C. Mittelstedt, "Minimum Weight Design of Curvilinearly Grid-Stiffened Variable-Stiffness Composite Fuselage Panels Considering Buckling and Manufacturing Constrains," *Thin-Walled Structures,* vol. 161, 2021.